EXPERIMENTAL AND ANALYTICAL STUDY IN FATIGUE AND WEAR OF STEEL AND NICKEL-BASED ALLOYS

by

Arman Ahmadi

A Dissertation

Submitted to the Faculty of Purdue University

In Partial Fulfillment of the Requirements for the degree of

Doctor of Philosophy

School of Mechanical Engineering

West Lafayette, Indiana

December 2021

THE PURDUE UNIVERSITY GRADUATE SCHOOL
STATEMENT OF COMMITTEE APPROVAL

Dr. Farshid Sadeghi, Chair
School of Mechanical Engineering

Dr. Carl R. Wassgren
School of Mechanical Engineering

Dr. Marcial Gonzalez
School of Mechanical Engineering

Dr. Vilas Pol
School of Chemical Engineering

Approved by:
Dr. Nicole L. Key

This dissertation is dedicated

to my parents

Ameneh Mansourghanaei and Ardeshir Ahmadi

ACKNOWLEDGMENTS

The work presented in this report would not have been possible without the support and encouragement of many people. First, I would like to express my sincere appreciation to my advisor, Prof. Farshid Sadeghi, for the continuous support, guidance, and encouragement throughout my study and research.

I thank the rest of my advisory committee: Prof. Carl R. Wassgren, Prof. Marcial Gonzalez, and Prof. Vilas Pol, for their help, insightful comments, and valuable guidance.

I would like to thank all my past and present friends at Mechanical Engineering Tribology Laboratory (METL) for their help and support. They provided a productive and friendly environment to work.

I would like to thank Dr. Kuldeep Mistry from Timken Company. His knowledge of the topic provided vital direction to my work and helped overcoming many challenges throughout the project. Also, I would like to thank the Department of Energy (DOE) for their help and support.

Most importantly, I would like to express my thanks to my beloved parents and my brothers for their support and encouragement throughout my time at Purdue. They have always been the strongest support to me and they deserve my deepest appreciation for their love, devotion, and sacrifices.

TABLE OF CONTENTS

LIST OF TABLES

LIST OF FIGURES

NOMENCLATURE

Symbol	Units	Description
E	GPa	Elastic modulus
E'	GPa	Equivalent stiffness
H	GPa	Hardening
ν		Poisson's ratio
S_y	GPa	Yield strength
S_{ys}	GPa	Torsional yield strength
α	GPa	Backstress tensor
σ	GPa	Stress tensor
σ^D	GPA	Deviatoric stress tensor
ε		Strain
$\dot{P}$		Plastic strain over a fatigue cycle
σ_{max}	GPa	Maximum von Mises stress
$\Delta\boldsymbol{\tau}$	GPa	Shear stress range
$\Delta\epsilon_p$		Range of plastic strain
M	GPa	Hardening modulus
G	GPa	Shear modulus
$\dot{\lambda}$		Plastic multiplier
$\hat{C}$		Scalar multiplier for hardening
σ_r	GPa	Material properties
m		Material properties
S_0	GPa	Material properties
q		Material properties
P_{max}	GPa	Maximum Hertzian pressure
V_w	μm^3	Wear volume
k		Archard wear coefficient
F	N	Normal force
S	μm	Total contact slip
δ	μm	Displacement amplitude
E_d	J	Energy dissipated at the contact
h	μm	Scar depth
a	μm	Half contact width
c	μm	Stick zone size
N		Number of cycle
N_t		Transition cycle from severe to mild wear
N_f		Cycle to failure
W	N	Normal load
Q	N	Shear load
D		Damage variable
μ		Coefficient of friction (COF)
d	μm	Ball diameter

ABSTRACT

Fretting wear occurs when two bodies in contact are subject to small oscillatory displacements. This wear phenomenon is common in many industrial applications, such as gears, couplings, bearings, screws, valves and joints where vibrations occur. It has been shown that many factors affect the fretting wear rate, e.g. the normal load, sliding distance, geometry of the bodies, surface roughness, material properties, lubrication status, temperature and presence of third bodies. Fatigue has also been the subject of much investigation over the past century. Fatigue damage is observed in the form of microcracks, debonding, etc. in the vicinity of stress risers (e.g. inclusions, voids etc.) within the materials. The stress component causing fatigue failure can be normal, shear, or a combination due to a compound state of loading. In order to investigate the shear mode of fatigue failure, torsional fatigue testing has been the subject of many studies. Shear mode of failure is of significant importance in triaxial state of stress present for ball and rolling element bearings and machine component which are subject to fretting fatigue. A number of different experimental and numerical techniques have developed to study the torsion fatigue and fretting wear of materials at different conditions. An in-situ fretting wear measurement technique was developed to investigate the effects of temperature on the coefficient of friction and wear rate of Inconel 617 in fretting wear in air and helium environments. Due to the importance of the shear mode of stress in fretting fatigue phenomenon, another set of experiments were designed to measure high cycle torsional fatigue properties of Inconel 617 at elevated temperatures. An MTS torsional fatigue test rig was modified with customized mechanical grips and cooling fins. In order to achieve the objectives of analytical aspects of this investigation, a 3D elastic-plastic finite element model was developed to examine the torsional fatigue damage in Inconel 617 material at high temperatures. Then, a 3D finite element model was developed to study fretting wear of similar materials in Hertzian line and circular contacts. The wear law incorporated in this model is based on the accumulated dissipated energy law. The FEM was used to investigate partial slip regime. Then, the model was verified by performing several experimental tests for the circular contact configuration. During fretting wear, the generated wear debris is of significant importance. A finite element model was created to study the third body effects on fretting wear of Hertzian contacts in the partial slip regime. Both first bodies and third bodies were modeled as elastic-plastic materials. The effect of the third body particles on contact stresses and stick-slip behavior

was investigated. The influence of the number of third body particles and material properties including modulus of elasticity, hardening modulus, and yield strength were analyzed. Finally, A new thermally cured polymer-graphene-zinc oxide-based solid lubricant was developed that reduced friction and wear significantly during the sliding wear of bearing steel under extreme contact pressure and long duration. The dry solid coating composite was made from a mixture of graphene, zinc oxide, and a specific industrial binder and then laminated on the surface of 52100 steel disks using the spin-coating technique. After ~3000 cycles, the 15 μm thick coating created a significant reduction in the steel's coefficient of friction (approximately 82%) and wear loss compared to the uncoated surfaces. Following the tribological examination, scanning electron microscopy, energy dispersive X-ray spectroscopy, X-ray diffraction, and Raman spectroscopy were conducted to determine the topography and morphology of the composite coating and resultant wear scars.

1. INTRODUCTION

1.1 Fretting Wear Phenomenon

Fretting wear occurs when two bodies in contact are subject to small oscillatory displacements. In machine components, this oscillatory motion causes wear and fatigue failures. Fretting often occurs entirely unexpectedly because only a negligible amount of motion is required from a few nan-scale to a couple of hundreds micro-sclae displacements. This wear phenomenon is common in many industrial applications, such as gears, couplings, bearings, screws, valves and joints where vibrations occur. It has been shown that many factors affect the fretting wear rate, e.g. the normal load, sliding distance, geometry of the bodies, surface roughness, material properties, lubrication status, temperature and presence of third bodies [1–5]. A major difference between fretting wear and other types of wear is that a substantial amount of wear debris is retained in the contact zone during fretting.

The response of a fretting contact is categorized based on the amount of slip that occurs in the contact. Fretting wear has been classified into several types including stick, mixed stick/slip, gross slip and sliding regimes based on the amount of stick and slip that occur in the contact [6]. Wear maps have been developed over the years which differentiates various types of fretting wear. The two most commonly used maps are: Running Condition Fretting Map (RCFM) and the Material Response Fretting Map (MRFM) which are introduced by Zhou et. al. [7] and Blanchard et al. [8], respectively. As shown in RCFM map, a contact is in the partial slip regime at high normal forces and low displacements, while the contact is in the gross slip regime at low normal forces and high displacements. The transition between these regions is the mixed fretting regime where the beginning of a test is in gross slip but the contact transitions into partial slip. These different regimes lead to a different damage mechanism. Cracking is the most dominant form of damage in the partial slip regime as long as the bulk tensile stress necessary for crack growth is present. In gross slip regime, wear dominates which causes the formation of a layer of wear particles that separate the two surfaces. In the mixed fretting regime, failure can occur from either wear or cracking or both. Figure 1.1(a) depicts the RCFM for different fretting regimes like partial slip, mixed stick-slip and gross slip based on normal load and displacement amplitude. Figure 1.1(b) depicts the MRFM related to different failure modes like surface cracking, wear etc.

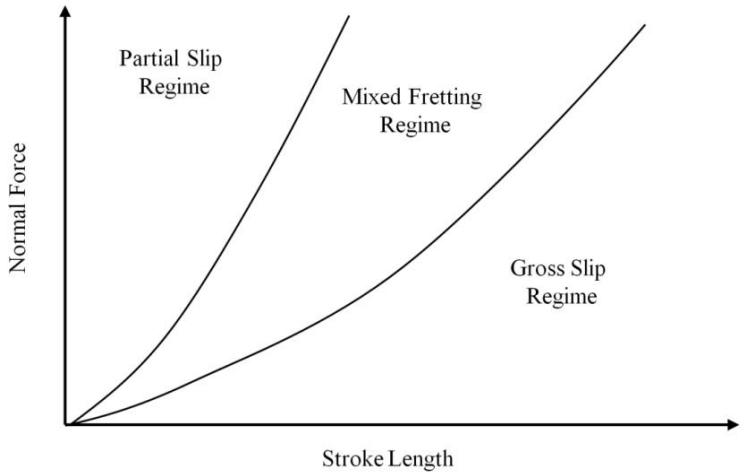

(a)

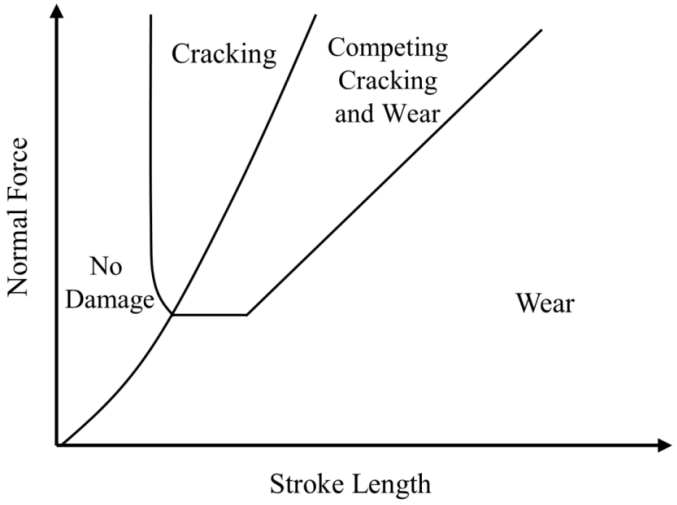

(b)

Figure 1.1. (a) Running Condition Fretting Map (RCFM), and (b) Material Response Fretting Map (MRFM)

Fretting regimes can be explained using the plot of friction force vs displacement amplitude, which is known as the fretting loop. Distinct partial slip and gross slip fretting loops are shown in Figure 1.2. In partial slip, the center of the contact area remains in stick and the rest of the contact is in slip throughout the fretting cycle while in gross slip the entire contact will slip at some point during the fretting cycle. The top and bottom edges of the rectangular fretting loop in gross slip regime occur when the entire contact is in slip. If the displacement amplitude becomes large

enough that the wear rate is the same as in uniaxial sliding, the contact is no longer considered to be fretting but reciprocating sliding.

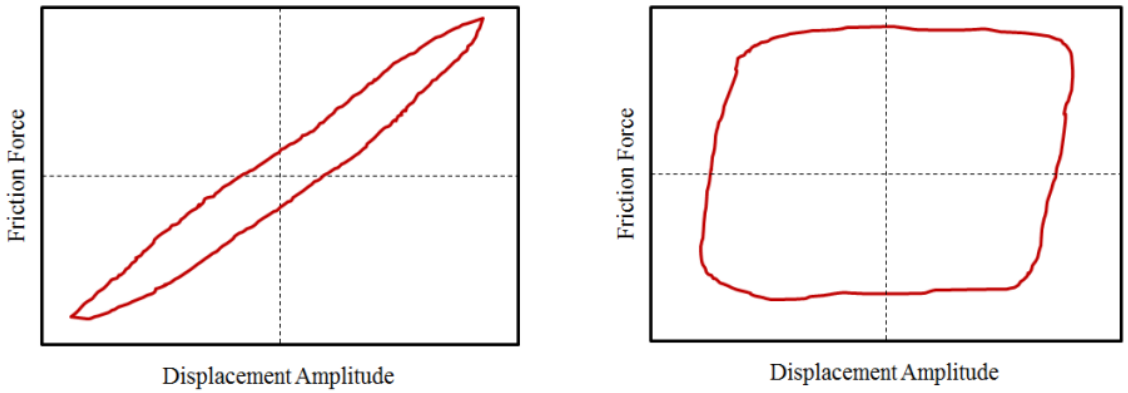

(a) (b)

Figure 1.2. (a) Partial slip fretting loop, (b) gross slip fretting loop

Beard [9] proposed a method for classifying fretting contacts into partial slip and gross slip regimes by using the ratio of frictional shear force (Q) to the slipping point ($Q/\mu \cdot P$). Here μ is the coefficient of friction and P is the normal force. Partial slip fretting takes place when this ratio is less than one. Gross slip fretting takes place when the ratio is equal to one. It is also mentioned in the literature that fretting occurs when $\frac{\delta}{a}$ is smaller than one while the contact is in reciprocating sliding if this ratio is bigger than one (δ is the displacement amplitude and a is half contact size).

Several wear laws have been discussed in literature to calculate wear due to fretting, but there are two which are widely used: 1. Archard Wear Law [10], 2. Dissipated Energy Wear Law [11]. Archard stated that wear volume (V_w) can be obtained from the following equation:

$$V_w = \frac{k}{H} FS \qquad 1.1$$

where k is the Archard wear coefficient, H is the hardness of the softer material in contact, F is the normal force, and S the total contact slip.

Dissipated Energy Wear Law says that that wear volume is directly proportional to the energy dissipated at the contact (E_d) due to relative tangential displacement.

$$V_w = \alpha E_d \qquad 1.2$$

1.2 Review of Fretting Wear Studies

Eden et al. [12] was among the first who observed fretting accidentally while studying fatigue in 1911. They noticed oxide debris forming at the interface between the test specimens and clamping device. The distinctive red wear particles which characterize steel fretting wear scars were considered to form from a chemical process and introduced the term fretting corrosion. T hen, Tomlinson [13] in 1927 conducted the first formal investigation of fretting. He realized that relative motion was necessary in order for the phenomenon to occur. Cattaneo [14] in 1938 and Mindlin [15] in 1949 started the construction of a theoretical framework for fretting wear by independently solving for the frictional shear stress between two spheres in partial slip. They explained the distinctive shape of the fretting wear scars and developed analytical and numerical models to predict local wear rates in fretting contacts.

Several theoretical models have been developed to explain fretting wear phenomenon. Goryacheva et al. [16] proposed an analytical method to evaluate the evolution of stress and surface profile in partial slip regime of fretting wear. They used Archard wear law to calculate the wear volume in the slip zone. Hill et al. [17] found a close form solution of elastically similar cylinder-on-flat contact subject to oscillatory shear stress in partial slip condition. Nowell [18] developed an efficient approach using quadratic programming to analyze the pressure profiles and worn geometries in fretting contacts. Dhia and Torkhani [19] developed a Lagrangian hybrid contact wear formulations to bound the wear of a body under an edge of contact.

The fretting phenomenon has been widely studied using different numerical modeling approaches. Johansson [20] presented a finite element (FE) model using Archard law for elastic contact to compute contact pressure evolution in fretting wear. McColl et al. [21] developed a 2D FE model to simulate the fretting wear and the evolution of the fretting variables in a cylinder-on-flat configuration. Paulin et al. [22] presented a 2D FE model using Archard law and dissipated energy method to modify the nodal coordinate for representing of material removal. Leonard et al. [23] developed a combined finite discrete element model to study the effect of displacement and normal load on fretting wear. They used Archard and dissipated energy wear theories to

investigate wear of Hertzian line contact. Cruzado et al. [24] introduced an optimized methodology to simulate wear scars in fretting wear. They used ABAQUS to simulate the crossed-cylinders configuration which consist of an optimum mesh size to minimize the computational time. Rodriguez-Tembleque and Aliabadi [25] proposed a 3D boundary element method (BEM) formulation to simulate fretting wear in fiber-reinforced composites under gross slip and partial slip regimes. They studied the effect of fiber orientation, sliding orientation and micromechanics on the wear evolution. Dong et al. [26] developed a semi-analytical solution to study partial slip wear of heterogeneous elasto-plastic materials. They applied an iterative conjugate gradient method and fast Fourier transform algorithm to determine the stick and slip areas. Yue and Wahab [27] studied the effect of variable coefficient of friction (COF) and constant COF on fretting wear of steels ranging from partial slip to gross slip. They generated a 2D plain strain cylinder-on-flat FE model to predict the wear scar and wear volume. Tobi et al. [28] studied the plasticity accumulation in fretting wear using an FE based wear model. They noted that significant plasticity accumulation occured due to plastic shakedown in partial slip regime while a saturation of plastic deformation was observed in gross slip regime. Ashton et al. [29] presented a 3D strain-gradient crystal plasticity finite element model to predict the microstructure length-scale effects on crack initiation under fretting fatigue.

Damage mechanics approach has been widely used to study fatigue and failure of materials. Bhattacharya and Ellingwood [30] presented a continuum damage mechanic (CDM) method to estimate cumulative fatigue damage and crack initiation by using principles of thermodynamics. Ireman et al. [31] developed a continuum damage model coupled to wear for studying crack initiation in fretting fatigue. In their model, the evolution of damage was obtained by a boundary value problem to have a mesh independent model. Raje et al. [32,33] modeled crack initiation and propagation using damage mechanics approach and discrete element method in the rolling contact fatigue (RCF) process. Warhadpande et al. [34] developed an FE model to investigate the influence of material microstructure on intergranular fatigue damage evolution in tensile test specimens. Zhang et al. [35] introduced a 3D FE model using CDM for multiaxial fatigue study. Leonard et al. [36] proposed a finite discrete element method to study fretting wear of rough and smooth Hertzian contacts by considering Archard law equation and CDM approach. Ghosh et al. [37] implemented a new wear law using damage mechanics approach in a 2D FE model to simulate fretting wear in partial slip regime of line contact configuration.

1.3 Fretting Wear at Elevated Temperatures

In industrial applications, fretting wear frequently occurs under elevated temperature conditions. One of the most severe environments and a common source of fretting failures is in turbine engines. Temperatures in the combustor exit exceed 1400°C while in the compressor temperatures reach 650°C. Engine components must resist oxidation, corrosion, erosion, and high pressure at high temperatures. Another source of high temperature fretting is in electrical contacts applications where thermal cycling combines with other vibrations to reduce component life. In these contacts, fretting highly depends on frequency. At very high frequencies, temperature changes do not have enough time to propagate and make large displacements [38–41]. Nuclear fuel rods and tubes in steam generators are also susceptible to high temperature fretting damages.

Temperature has a noticeable influence on the fretting wear of materials [42–44] . Oxidation rate, corrosion and mechanical properties of materials change as the temperature changes. The rate of wear in fretting of metals usually decreases if a thick, stable, mechanically strong and adherent oxide film is created on the surface. In this case, oxidized layers act as a solid lubricant which reduces friction, wear, and surface damage [45]. In addition, the mechanical properties of the materials and the intensity of the fretting process affect the amount of the oxide films that form and can be maintained at elevated temperatures. If the oxide layers are damaged, then the wear rate will probably grow much more than at lower temperature [46]. The formation of the oxide layers at high temperature has been mentioned for different materials such as steels [47,48], aluminum alloys [49], titanium alloys [50] and nickel alloys [51,52]. For the medium carbon and stainless steels, it has been demonstrated that the wear rate decreased an order of magnitude over the transition temperature [53–55]. Hurricks [56,57] noted that the transition temperature is related to a change in the rate of the oxide film from logarithmic to parabolic growthand to change from α-Fe2O3 to Fe3O4 within the oxide layer. Other researchers have focused on the mechanical property aspect of the debris instead of the rate of the oxide film on a surface. Experimental tests illustrated that oxide particles which were supplied into the contact artificially and formed the debris bed resulted in reducing the wear, but when a stable oxide layer didn't form on the surface, then having more oxidation increased the abrasion and consequently increased the wear rate. Sintering is another factor which has been considered in the high-temperature wear phenomenon in the literature [53,58–60] . Kato [61] studied the sintering

process between Fe2O3 oxide particles at room temperature. He showed that the oxides with a higher diffusivity rate and smaller size promoted the formation of the oxide film on the surface, and therefore exhibited a mild wear rate. Formation of a glaze in the contact area during fretting wear at high temperature is another topic discussed in the literature. The glaze is a smooth glassy layer appearing on the top of the oxide film which contains compacted sub-micron size oxide debris particles. It was proposed that the formation of the glaze is due to the plastic flow of oxides which were small in size and carried hydrostatic loading that was associated with the sintering [62,63].

1.4 Third Body Concept in Fretting Contact

Third body particles are generated during unlubricated, boundary or mixed lubricated contacts under combined normal and tangential loads. The geometry and material of the bodies in contact, surface roughness and external loads affects debris generation. The generation of wear particles is usually a mechanical process. Wear debris detach from the unworn bodies in contact as a result of localized stresses at the contact. Some common surface damages that lead to generation of wear particles are micro-cutting, plastic deformation, surface fatigue, spalling etc. Wear debris have been mentioned as one of the main reasons why synthesizing the numerous wear laws describing the fretting phenomena is difficult. Wear debris can have both beneficial and harmful effects on fretting contacts. A large wear particles mass and the formation of a compacted oxide layer can reduce friction and the separation of the first bodies. On the other hand, the wear debris can cause abrasive wear. Figure 1.3 shows the zones, bodies, and flow rates of a third body wear system.

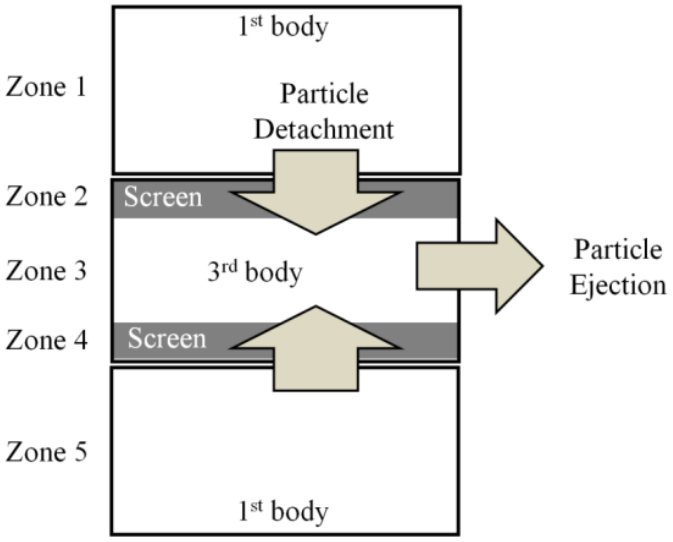

(a)

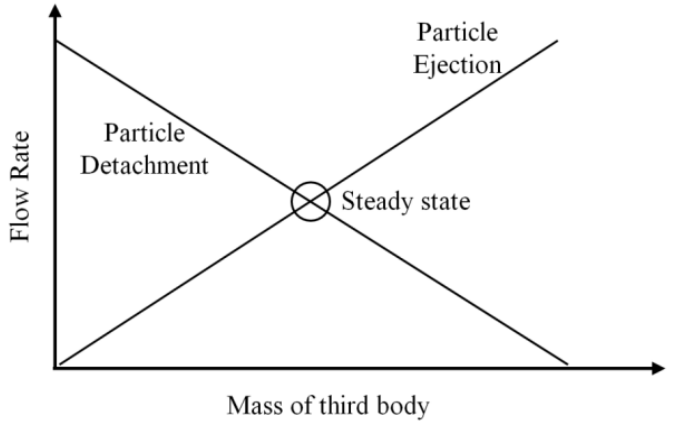

(b)

Figure 1.3. (a) Third body tribological circuit (b) Flow rates in a third body contact

In the wear process, “first bodies” refer to the rubbing parts and “third body” refers to the debris and particles which are generated during the process. Godet [64] introduced the concept of the third body to link lubricated and dry contacts. Many wear equations are proposed by different authors to describe the fretting process, however, there is not a single general law that match well with the experimental results due to the existence of the third bodies and complexity of the problem. Generation of debris in contact can be due to several factors such as surface and subsurface failure, micro-cutting, plastic deformation, spalling, etc. [65]. According to Waterhouse and Taylor [66], the detachment of third body particles from first bodies is because of the initiation of subsurface

crack and delamination in the wear process. Detached particles in wear might either trap between the first bodies and compact to a solid third body layer or eject outside the contact. Detrimental effects of debris could be more critical at the beginning of the fretting process as the mass of the particle is small. As wear continues, wear particles accumulate and form a compacted oxide particle layer which leads to alleviating wear [67]. Iwabuchi [67] showed that higher debris mass resulted in lowering the wear rate implying that abrasive qualities of debris were counterbalanced by its beneficial effects. However, it is worth mentioning that the debris phenomena also depend on contact shape, contact orientation, and wear particle properties [68–70].

Berthier [71] illustrated the concept of the third body by the tribological circuit. In this theory, the particles are generated from the wear of two first bodies, recirculate in the wear track and then some portion of those particles is ejected from the contact. When the generation rate and ejection rate of third bodies are equal, a stable equilibrium is achieved and a steady layer of debris is formed. Any change in contact conditions could change the equilibrium state by altering the generation and ejection rates of third bodies but a temporary disturbance won't move the contact to a new equilibrium point.

Continuum and discrete approaches are two common methods to simulate the third body in a wear process. In the continuum approach, the particles are considered to be continuum and isotropic and the rheological properties would be studied. According to the third body behavior, both solid and fluid mechanics methods can be applicable [72]. Heshmat [73] studied the parameters such as pressure and geometry of particles that determine the solid or fluid behavior of a third body. On the other hand, discrete modeling received a lot of attention for the debris simulation as a third body is anisotropic, heterogeneous and discontinuous. Furthermore, the continuum approach is not a precise method for this problem. Cundall and Starck [74] developed a discrete element method (DEM) for the third body modeling. Iordanoff et al. [72] developed one of the first discrete element models to study the effect of particle size and internal forces on the macroscopic response of the contact. They used Couette flow with periodic boundary conditions for the particles modeling. Fillot et al. [75] developed a wear model using DEM by considering a degradable first body in the simulation. They stated that material properties and applied load affect the steady-state thickness of the third body. Iordanoff et al. [76] simulated the abrasive particles from a polishing process using DEM and considering a degradable first body.

Similar to DEM, the finite element modeling (FEM) has been applied in the third body study. In the FEM, the particles can be considered deformable while in DEM they are rigid. Both implicit and explicit techniques have been used for modeling the third body but the explicit model is more common for granular flow problems. Linck et al. [77] used FEM to simulate the third body which was rubbing against a rigid surface and showed the stick-slip behavior. They suggested that the slip wave could explain the particle detachment in the wear process. Ding et al. [78] simulated the third body in a 2D FEM model. They considered the third body as a thin layer with different properties than the first bodies. Their results indicated that the presence of third body particles made a narrower and deeper wear scar. Kabir et al. [79] applied an explicit FEM for granular particle modeling. They studied the effect of material properties and gap height on the velocity of third body and compared the results with DEM. Cao et al. [80] developed a coupled FEM-DEM model to study the performance of stress and velocity on the third body. They considered the third body and the upper first body as rigid while the lower first body as deformable. Basseville et al. [81] modeled the debris using rectangular finite element mesh placing in between the contact surfaces. They demonstrated that wear particles were ejected in the gross slip regime while trapped in the partial slip regime. Leonard et al. [82] introduced a 2D finite-discrete element model to study the effect of the third body in fretting. They modeled the first bodies using finite elements and the third body using discrete elements. They studied the effect of debris on the normal and shear stresses in Hertzian line contact. Ghosh et al. [83] studied the effect of the third body in a Hertzian line contact using a 2D FEM. Both first bodies and third bodies were deformable with elastic-plastic properties. They evaluated the effect of particle numbers on the contact pressure, slip, and shear stress.

1.5 Anti-Wear Coatings in Wear Applications

The majority of engineering systems can encounter a damage because of wear and friction. One of the reasons could be related to the mechanical components and manufacturing instruments with parts in contact and relative motion [84]. Lubrication is one of the most widely recognized methods of improving the efficiency, performance, and lifetime of mechanical components by reducing friction between two sliding surfaces. The use of liquid lubricants such as organic oils [85] is one of the most common means of reducing energy losses at moving interfaces. Furthermore, the importance of additives in the tribological performance of lubricating oils has been investigated

by many researchers [86–91]. However, liquid lubricants are not good candidates in high-temperature or low-pressure applications due to their low resistance to vaporization [92,93]. On the other hand, dry solid lubricants have proven to be a vital option for high-load, high-speed, and extreme environmental conditions. Various types of solid lubricants such as molybdenum disulfide (MoS2) [94], boron nitride (BN) [95], polytetrafluoroethylene (PTFE) [96], and graphene [97] have been studied.

Graphene is a two-dimensional material with distinct friction and wear properties that can be used as a solid lubricant. Graphene is composed of a unique flat hexagonal lattice of aromatic carbon rings with well-stablished thermal and electrical conductivity [98,99], mechanical strength [100], and ultra-low friction and wear [101,102]. Its excellent tribological properties result from its high chemical inertness, high strength, low shear capability, and atomically smooth surface. Graphene can be utilized in both nanoscale [103] and microscale [104] applications because it is an ultra-thin material.

The macroscale tribological properties of graphene are of paramount importance to various industries where high friction and high wear are prevalent. Won et al. [105] investigated the durability and wear mechanism of graphene coatings on copper substrates under dry contact sliding wear with a contact pressure of 220 MPa. Berman et al. [106] studied the tribological performance of graphene-coated steel in dry nitrogen under a maximum Hertzian pressure of 410 MPa. They illustrated that friction and wear reduction occur only under low contact pressure, and that poor adhesion of graphene to a substrate leads to a rapid increase in friction and wear under excessive contact pressure (i.e., >0.5 GPa). Such studies demonstrate that strong adhesion of the coating to the substrate surface is another key parameter that should be considered in a solid lubricant.

Zinc oxide (ZnO) is an inorganic compound that can be used in paints and coatings as an additive to enhance adhesion and corrosion resistance [107,108]. ZnO actually is a very good candidate for strengthening adhesion between graphene and the substrate surface. Wu et al. [108] proved that the ZnO composite enhances the adhesion of graphene layers to silver electrode-coated surfaces. Song et al. [109] investigated the tribological performance of a polyurethane composite coating filled with ZnO particles. He noted that the wear resistance of polyurethane was increased by adding ZnO to the coating and, furthermore, that scuffing and adhesion of the coating were enhanced. Selvam et al. [110] studied the behavior of a magnesium matrix composite reinforced with ZnO particles in dry sliding wear. He asserted that the addition of ZnO to the magnesium

matrix improved the abrasion and delamination resistance of the coating. Alazemi et al. [111] proposed a graphene-zinc oxide composite solid lubricant to reduce friction and wear in stainless steel substrates under high contact pressure. However, the surface adhesion properties of former composite solid lubricant coating was very poor, limiting the durability.

1.6 Torsion Fatigue of Materials

Fatigue has been the subject of much investigation over the past century. Fatigue damage is observed in the form of microcracks, debonding, etc. in the vicinity of stress risers (e.g. inclusions, voids etc.) within the materials. The stress component causing fatigue failure can be normal, shear, or a combination due to a compound state of loading. In conventional fatigue testing, a specimen is stressed repeatedly as rotating bending or axial tension to investigate the material behavior under cyclic tensile stresses. However, many engineering structural components such as automotive transmission shafts, axles, crankshafts are stressed not only with axial tension-compression loads but also cyclic shear or torsional loads. In order to investigate the shear mode of fatigue failure, torsional fatigue testing has been the subject of many studies [112–115]. Shear mode of failure is of significant importance in triaxial state of stress present for ball and rolling element bearings and machine component which are subject to fretting fatigue [37,84].

In general, fatigue failure involves three stages: crack initiation, crack propagation and final catastrophic failure [115,116]. The amount of the life related to each stage is associated with material properties, loading conditions and environmental conditions. Crack initiation is considered to be the largest contributor to fatigue life of various materials especially in high cycle fatigue (HCF) [117]. Crack initiation may occur at surface defects, imperfections, voids, inclusions, weak planes, or other microstructural defects. These variations in microstructure and material properties lead to the high scatter observed in fatigue results [118].

Several numerical models have been developed to investigate fatigue life of various materials operating under various loading conditions. Aktaa and Schmitt [119] proposed a modified inelastic strain rate damage model to predict life of steels under creep-fatigue conditions. Rinaldi et al. [120] suggested a lattice model to study the effects of microstructural and geometrical variability of a polycrystalline materials in fatigue. Raje et al. [32] developed a damage mechanics based fatigue model for rolling contact fatigue using the discrete element method. Slack and

Sadeghi [121] developed an explicit finite element model (FEM) using the cohesive zone approach for the grain boundaries and discussed the effect of grain boundaries properties on fatigue lives and spall patterns. Several investigators have modelled torsional fatigue. Papadopoulos [122] introduced a novel fatigue law for multiaxial non-proportional stress loading on the crystalline structure of metals to explain out of phase torsion and bending fatigue limit. Bomidi et al. [115] developed a 3D FEM using Voronoi tessellation and damage mechanics approach to obtain fatigue life and crack path in torsional fatigue of bearing steels. Mobasher Moghaddam et al. [114] proposed a 3D FEM model to study the effect of compressive stresses on torsional fatigue life of bearing steels.

1.7 Scope of This Work

During the past few decades, fretting has grown and the phenomena has changed from being considered as a primarily chemical process to a mechanical one. However, the current literature does not provide rules which can be easily implemented by the engineers leading to many unpredictable machine failures in different environmental conditions. The first objective is to develop a set of experimental tests for investigating fretting wear of materials at elevated temperatures. The developed tests will allow fretting to be studied at high temperatures and in different environmental conditions. Also, the proposed numerical models will provide more insight into the understanding of fretting wear phenomenon and allow the third body effect to be analyzed more realistically.

Chapter two presents the fretting wear behavior of Inconel 617 at room and elevated temperatures. Several tests at high temperatures were conducted in both air and helium environments. The coefficient of friction (COF) and the hysteresis loops were reported for different conditions of the tests. A modified Archard wear law is proposed to state the bilinear wear behavior of the material during the test. Topography and dimensions of the scars were characterized using optical profilometer and Scanning electron microscope (SEM). Morphology and relative proportion of elements of the scars were determined by SEM and energy dispersive X-ray spectrometry (EDX).

In chapter three, high cycle torsional fatigue behavior of Inconel 617 at 850°C was experimentally and analytically studied. For the experimental aspects of this study, an MTS torsional fatigue test rig was modified by designing custom cooling fins and mechanical gripes to

allow tests at elevated temperatures. In the analytical aspects of this study, a 3D elastic-plastic FEM was developed to determine the torsional fatigue damage of the material at high temperatures.

In chapter four, a 3D Hertzian point contact model was developed using FEM to study the effects of third body phenomenon in partial slip fretting wear. Both the first bodies and the third body were considered to be deformable with the elastic-plastic material properties. The wear particles were located in the slip zone of the contact and a partial slip regime was simulated. In this modeling, the effect of third body on the contact pressure and shear stress was investigated in detail. Also, the effects of number of particles on the contact pressure and total load carried by particles were evaluated. The influence of the number of third body particles and material properties such as modulus of elasticity, hardening modulus, and yield strength were studied. Fretting loops for with and without wear particles were compared and the relation between the number of cycles and the hardening process was obtained. Finally, wear debris with different material properties than first bodies were studied to represent the influence of oxidization of the particles.

In chapter five, a 3D fretting wear model was developed based on the damage mechanics approach and accumulated dissipated energy to investigate fretting wear of Hertzian circular and line contacts. The damage mechanics stress-based law was implemented using the commercially available ABAQUS finite element software. Voronoi tessellation was used to simulate the microstructure of the material. Fretting wear process was simulated such that the elements with the maximum stress were removed in each fretting cycle. In order to reduce the computational expenses, the partial slip regimes were modeled using the normal and shear surface tractions for the circular and line contacts applied to the wear body. The stress distribution and wear volume rate calculated from FE model were compared with the wear coefficient available in the open literature. The influence of modulus of elasticity, hardness, and COF on fretting process were evaluated. Then, the FE model was verified using several fretting wear tests for two different materials (AISI 8620 and AISI 1566). The experiments were performed for the circular contact configuration. The modulus of elasticity and hardness of each material were obtained using nanoindentation tests near the contact surface and the grain size were measured using the scanning electron microscope (SEM). These properties were implemented in the FE model and the worn surface and wear rate were compared with the experimental results.

In chapter six, a cured Aremco-Bond™ 570 polymer-graphene-zinc oxide composite was developed to increase the adhesion and durability of the coating on contact surfaces and to reduce friction and wear in bearing steels under high contact pressure. The proposed composite was made from graphene, zinc oxide particles, and a specific binder including butanone and isopropanol and was laminated on a bearing steel disks. A sliding wear test with a ball-on-disk configuration was used to measure the tribological performance of the composite coating under a contact pressure of 1 GPa. Scanning electron microscope (SEM), energy dispersive X-ray spectrometry (EDX) analyses and X-ray powder diffraction (XRD) were conducted to determine the topography and morphology of the composite coating and the wear scars. Raman spectroscopic analysis and Fourier transformed infrared spectroscopy (FTIR) were conducted to study the mechanical and chemical durability of the composite coating. The surface adhesion properties of the coating were measured using the Nanovea® scratch tester and compared to an earlier graphene-zinc oxide-PVDF coating.

2. IN-SITU FRIRCTION AND FRETTING WEAR MEASUREMENTS OF INCONEL 617 AT ELEVATED TEMPERATURES

2.1 Introduction

The Fretting is a special wear process which occurs when two bodies in contact are subject to small amplitude relative motion. This wear phenomenon is common in many industrial applications, such as gears, couplings, bearings, screws, valves, and joints, often where vibrations occur. Fretting wear was classified into several types including stick, mixed stick/slip and gross slip regimes [6,83]. Many factors influence the fretting wear rate, e.g. the normal load, sliding distance, geometry of the bodies, frequency, surface roughness, material properties, lubrication status, environmental conditions and temperature [1,3].

Inconel 617 is a widely used material in a very high-temperature gas-cooled reactor (VHTR) and in gas turbine combustion equipment because of its high-temperature strength, creep and wear resistance. Helium is a primary coolant gas used in these reactors. The relative movement of different components in the reactor such as rods and valves lead to a potential failure of the components due to the friction, fretting, self-welding and galling. Birol [58] investigated the sliding wear resistance of Inconel 617 at high temperature and compared with Stellite 6 and tool steel. He expressed that the plastic Cr_2O_3 on Inconel 617 and Stellite 6 remains more during the sliding wear process than the tool steel which attributed to their lower wear rate.

Though the effect of temperature on the wear rate of different materials has been extensively studied previously, there has been very little investigations on in-situ measurement of the fretting wear at high temperature, specifically for Inconel 617. In the current chapter, the fretting wear behavior of Inconel 617 at room and elevated temperatures was studied. Tests at high temperatures were conducted in both air and helium environments. The coefficient of friction (COF) and the hysteresis loops were reported for different conditions of the tests. Two distinct wear regimes including a severe running-in and steady state were obtained by in-situ measurement of the wear and verified by wear measurement after the tests using a profilometer. A modified Archard wear law is proposed to state the bilinear wear behavior of the material during the test. Topography and dimensions of the scars were characterized using optical profilometer and Scanning electron microscope (SEM). Morphology and relative proportion of elements of the scars were determined by SEM and energy dispersive X-ray spectrometry (EDX).

2.2 Experimental Procedure

In this section, the material properties and the fretting test method which have been accomplished for this high temperature study will be discussed in detail.

2.2.1 Material

The fretting tests were carried out using an Inconel 617 ball on an Inconel flat disk. Inconel 617 is a nickel-chromium-cobalt-molybdenum alloy. The combination of high-temperature strength and oxidation resistance makes this alloy a good material for high-temperature applications. The chemical composition of Inconel 617 is given in Table 2.1. The balls with the diameter of 6.35 mm and the flat specimens were machined from Inconel 617 blocks. The surface roughness of the ball and the flat was around Ra=0.4 µm.

Table 2.1. Composition of Inconel 617 (wt.%)

Ni	Cr	Co	Mo	Al	C	Fe	Mn	Si	S	Ti	Cu	B
44.5 min	20-24	10-15	8-10	0.8-1.5	0.05-0.15	3 max	1 max	1 max	0.015 max	0.6 max	0.5 max	0.006 max

2.2.2 Fretting Tests

Fretting tests were conducted for the ball-on-flat configuration on a Bruker UMT Tribolab. A high-temperature ball holder made of Hastelloy-x was used to withstand high temperatures during testing. This ball holder was attached to a heat sink mounted between the holder and the force sensor at the top of the setup. A dual-axis force sensor was used to measure the friction force and the normal force simultaneously. The force sensor can measure a load in the range of 0.5 N to 50 N with the resolution of 2.5 mN. A reciprocating linear drive was used to reciprocate the flat plate against the stationary ball. The reciprocating platform had an adjustable stroke length ranging from 30 microns to 25 mm with a frequency of up to 60 Hz. An ultra-high temperature chamber was utilized to allow testing up to 1000 °C during the process with a controller resolution of 0.1 °C. In addition, a closed chamber was developed for introduction of gas inside the chamber in case of performing the test in the helium environment. Figure 2.1 shows the fretting setup.

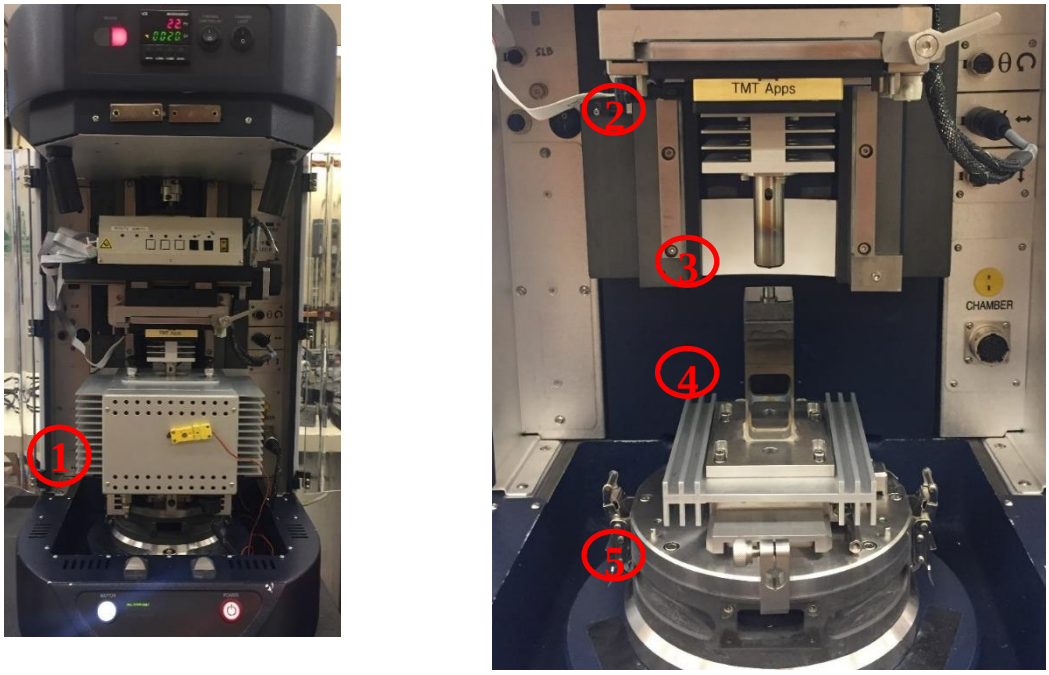

(a) **(b)**

Figure 2.1. Commercial tribometer modified for high-temperature testing: (a) Fretting setup (1. Heater), (b) Specimen setup (heating chamber removed for clarity) (2. Load cell, 3. Ball holder, 4. Flat holder, 5. Reciprocating drive)

The normal load applied in all the tests was 4 N and remained constant during the tests. The zero to peak displacement of 250 µm (stroke length of 500 µm) was applied with the frequency of 10 Hz to the flat specimen. A linear encoder with the resolution of 1 µm was utilized to assure feedback to the reciprocating drive. A position probe with the resolution of 0.1 µm was placed on the carriage of the machine measured the wear depth during the test. The friction force and the displacement amplitude were measured during the tests with the sampling rate of 2000 Hz. In order to have a constant gaseous atmosphere for the tests in the helium environment, a constant gas flow was injected at a constant gas pressure and the average flow rate of 40 L/min to a closed chamber. Commercial helium gas with the purity of 99.999% was used in this investigation. An oxygen detector (Single O2 detector, BW Technologies) was utilized inside the chamber to monitor the level of oxygen during the tests and it was kept below 1% during the experiments. Prior to testing, any residual debris was removed from all specimens using an ultrasonic cleaner and acetone. The room temperature tests were conducted in ambient air at 25 °C and high temperature tests at 375 °C and 750 °C. The relative humidity was 40 to 50% for the ambient

tests. Each test was repeated at least three times with the error of measured friction and wear below 5%. Wear scars from the ball-on-flat configuration were scanned using an optical surface profilometry (ZeScope, Zygo Corp.). SEM investigations combining with EDX analyses were carried out to examine topography and morphology of the scars. Table 2.2 shows the experimental parameters of the fretting wear tests.

Table 2.2. Experimental parameters for the fretting tests

Experimental Parameters	**Value**
Normal load	4 N
Displacement	250 µm
Frequency	10 Hz
Cycles	0.5k, 1k, 2k, 5k, 10k, 20k, 30k
Gas atmosphere	Air, He
Temperature	20 °C, 375 °C, 750 °C

2.3 Results and Discussion

In this section, the hysteresis loops at different temperature and environments, coefficient of friction for various conditions and the wear rate of the tests will be discussed.

2.3.1 Hysteresis Loop and COF

Fretting loops at room and elevated temperatures in air environment are illustrated in Figure 2.2. All the fretting tests showed gross sliding hysteresis loops. The fretting loops at elevated temperatures demonstrated decreased COF as compared to the room temperature. For the high temperature conditions, the results showed the force to peak at the end of the stroke. This is mainly due to material's build-up at the edges of the contact during the high temperature test. This phenomenon is associated with the plastic deformation at the front and rear contact borders. The interaction between the moving part and ploughing of the material causes the force to peak in hysteresis loops [2,123,124]. These force peaks were more significant in helium environment at high temperatures (750 °C) as illustrated in Figure 2.3. At this temperature (750 °C) and in helium environment, a higher level of plasticity is expected at the end of the stroke due to a reduction in material strength and hardness at elevated temperature. Tests in air environment illustrated lower force peaks than in helium environment. It is hypothesized that this phenomenon could be related to oxidation at high temperature which reduced the force peak.

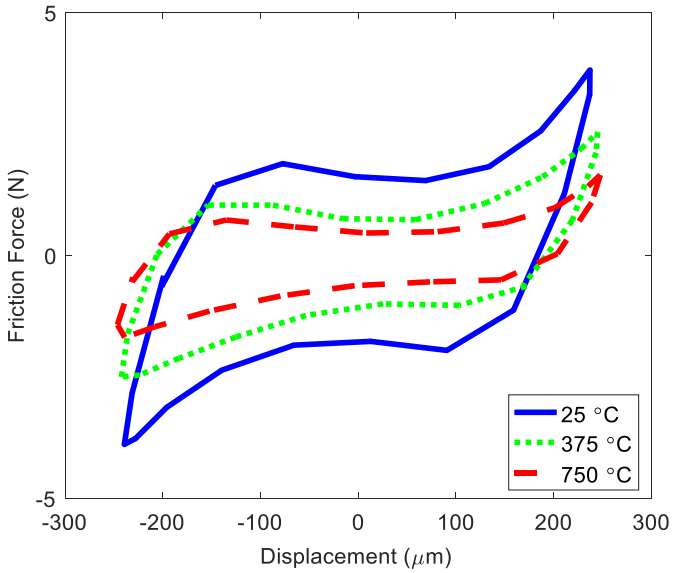

Figure 2.2. Fretting hysteresis loops conducted at different temperatures and in air taken at 30,000 cycles

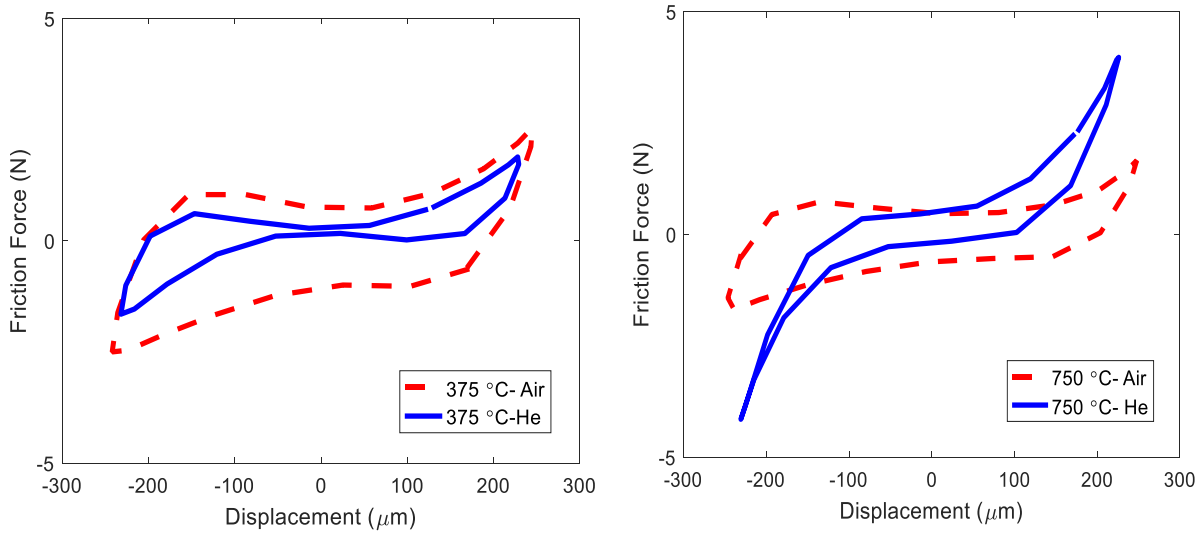

(a) **(b)**

Figure 2.3. Fretting hysteresis loops in air and helium taken at 30,000 cycles: (a) 375 °C, (b) 750 °C

The area under the hysteresis loop corresponds to dissipated energy in each cycle during the fretting test, and by summing the dissipated energy for all the cycles (Ed) [123], accumulated dissipated energy can be obtained. This energy loss per cycle can also be used to identify the

transition from gross slip to partial slip regime in fretting [43]. The frictional dissipated energy per cycle is depicted in Figure 2.4 for the ambient and high temperatures tests. In both ambient and high temperatures cases, the dissipated energy started high and gradually reduced to a steady state. As the cycles increased, the surfaces became smoother resulting in a decrease in the dissipated energy which was observed after around 5000 cycles. The elevated temperatures results showed lower steady state frictional dissipated energy which was consistent with COF behavior.

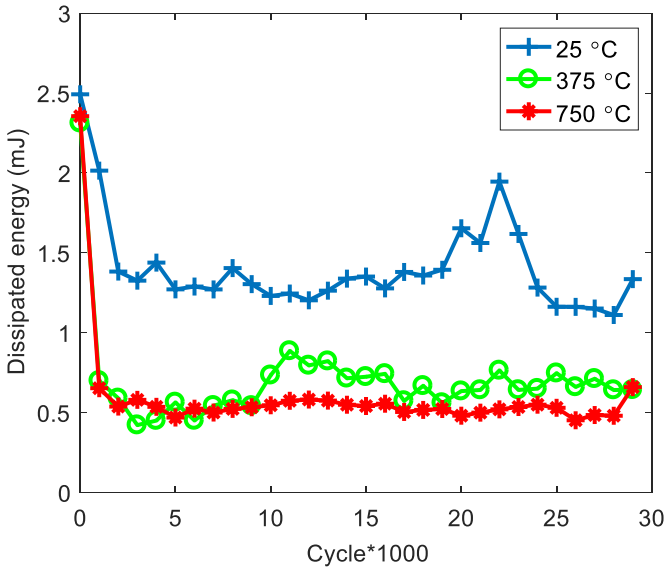

Figure 2.4. Energy loss per cycle for different temperatures in air environment

Based on the ploughing effect that was discussed previously, the normalized tangential force ratio $\frac{Q}{F}$ might not be a good representation of COF (Q is the tangential force and F is the normal force). An average energy friction coefficient can be defined based on the dissipated energy per cycle divided by to the total energy 2FS [123].

$$COF = \frac{E_d}{2FS} \tag{2.1}$$

where Ed is the dissipated energy during fretting cycles, F is the applied normal force and S is the total stroke length.

Figure 2.5 shows that the COF derived by the energy dissipated method was less than that obtained by the normalized tangential force method. With either method, however, two stages can

be observed. A high value of COF in the first few hundred cycles which indicated the formation of the metal to metal contact, after which it reached the steady state value, which was lower than the start value. We propose this was due to the presence of the third body in the contact.

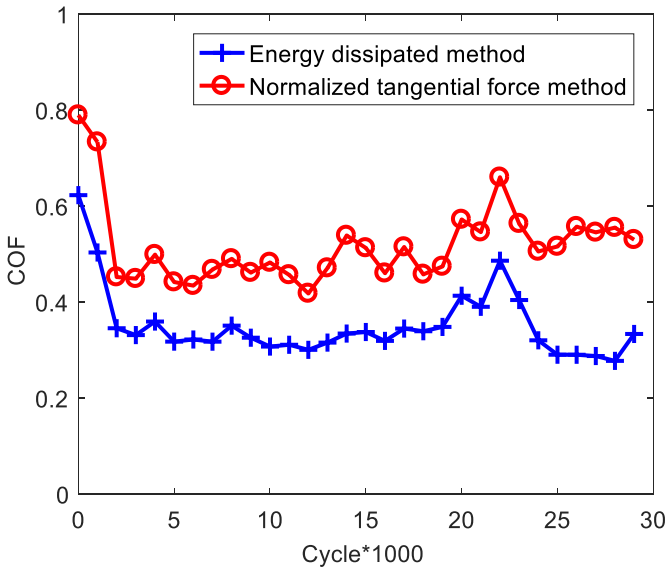

Figure 2.5. Comparison of the COF obtained by the normalized tangential force method and energy dissipated method

Figure 2.6a depicts the development of the COF versus cycle for the tests at different temperatures in air and helium environments obtained by dissipated energy method. It was shown previously that at 25°C and in air, the COF rapidly decreased from 0.7 to around 0.41 after a few hundred cycles and then had a small fluctuation to the end of the test. At 375°C in air, the COF started around 0.6 but it drastically decreased such that the stable value was about 0.17. At 750°C in air, the COF began at around the same value as 375°C and then dropped to around 0.13, which was lower than the other two temperature conditions. According to the literature [125], the glazed surface in the contact zone is responsible for the decrease in COF at high temperatures as it develops a wear protective surface. In helium environment, there was not such a big difference in COF with temperature compared to air environment. At 375°C in helium, there was a little oxidation on the surface of the parts that resulted in having lower COF than air environment which had a bit more oxidation on the surfaces. The test at 750°C and in helium had the lowest COF.

In order to compare the effect of temperature on the COF quantitatively, the steady state section of the results (after 5000 cycles) were averaged and defined as steady state COF. Figure

2.6b shows that the steady state COF dropped as temperature increased, though the rate of the change was minimal above 400°C.

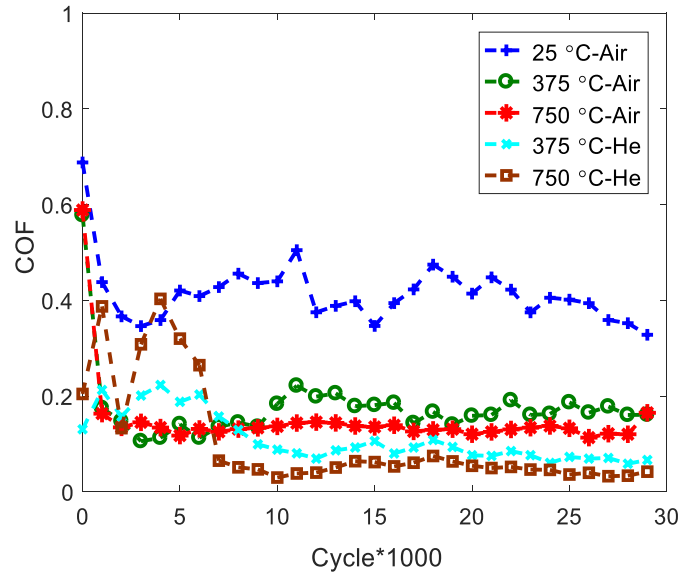

(a)

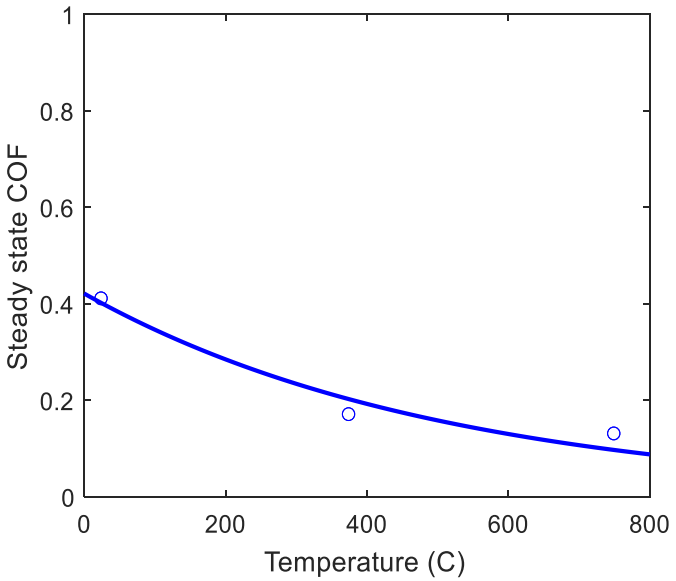

(b)

Figure 2.6. (a) Change of the COF with cycle as a function of temperature in air and helium, (b) Change of the steady state COF as a function of temperature in air

2.3.2 Wear Rate

In-situ measurement of the wear rate was conducted using a proximity probe during the fretting test to measure the depth of wear. Figure 2.7a depicts in-situ measurement of the scar depth in room temperature and for various cycles. Two different slopes were observed such that there was a high wear rate in the running-in regime followed by a mild steady state wear rate. According to the Archard equation, wear rate is linearly proportional to the total sliding distance, but the current tests indicated that there is a bilinear approximation between the wear depth and the sliding distance. The running-in regime had an order of magnitude higher wear rate than the steady state regime, with the change likely due to the initial high contact pressure. Wear and plasticity in the first few hundred cycles enlarges the area of contact and consequently, as the number of the cycle is further increased and additional material is removed, the contact pressure decreases and the surfaces are separated by the wear debris. This bilinear wear behavior has been demonstrated by several researchers. Cruzado et al. [126] investigated the wear of thin steel wires in cross cylinders geometry and observed two different wear periods of running-in and steady state. Henein et al. [127] measured the wear between cylinder liners and piston and showed a bilinear behavior on the wear depth of specimens. Ghosh et al. [128] proposed a numerical approach to extend wear modeling of real engineering surfaces and obtained two distinct running- in and mild wear regimes. He asserted that roughness parameters have a high influence on the wear rate of first regime.

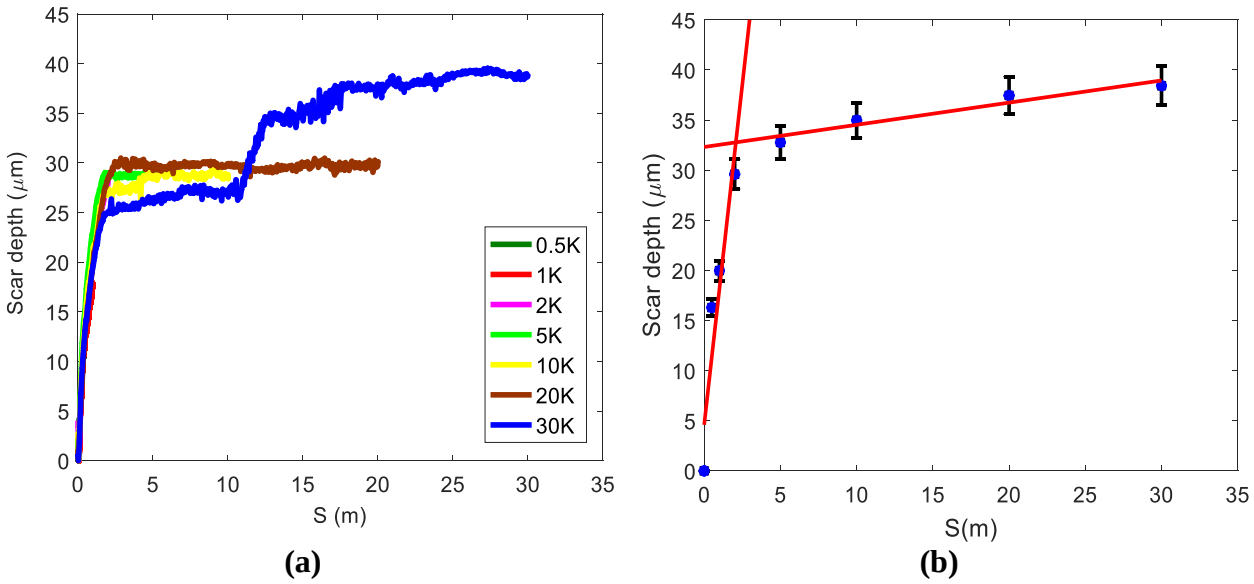

(a) **(b)**

Figure 2.7. (a) In-situ measurement of wear depth at room temperature and air environment, Measuring of wear depth at room temperature and air environment by profilometer after completing the tests

Averaged contact area during the wear is defined as $A_{avg} = \frac{\pi}{4}c^2$ whereas c is the scar width, and the relation between the depth and diameter of the scar for the ball (ASTM G99) is;

$$c = 2\sqrt{r^2 - (r-h)^2} \qquad 2.2$$

Where r represents the ball diameter, h is the scar depth, and c is the scar width. According to equation 2.2 and Figure 2.7, P_{avg} during the test decreased significantly in the running-in regime and then it became stable (Figure 2.8).

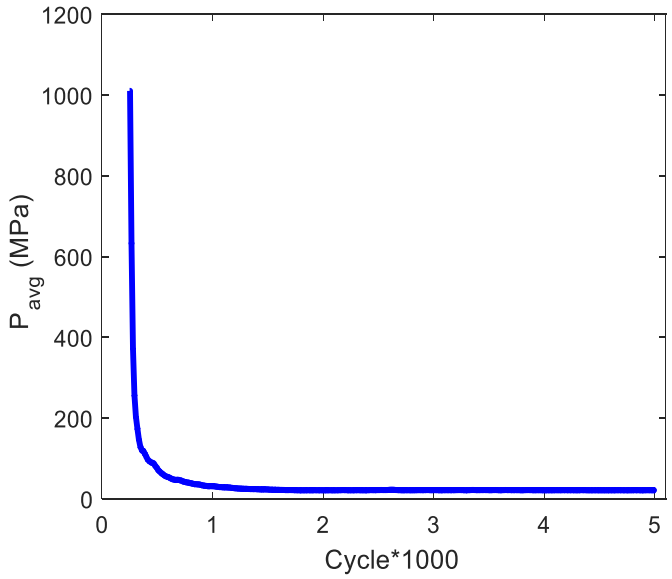

Figure 2.8. Change of average pressure during fretting test

Equation 2.2 can be used to obtain the scar depth on the ball when the wear just happens on the ball and there is no significant wear on the flat specimen. The same procedure can be used to calculate the depth of the scar on the flat specimen by assuming that there is no considerable wear on the ball. After the tests were completed, the depth of the scars was measured using an optical surface profilometer and considering the average width of the scars on both parts and using equation 2. It was assumed that each body (i.e. the ball and flat) equally wore during the fretting process. The profile of the scar depth measured by the profilometer verified this assumption (Figure 2.9). Using this assumption and plotting the total scar depth on Figure 2.7b demonstrated that measuring scar depth at the end of the test also represented the same bilinear behavior of the wear rate during the test and it was in a good correlation with in-situ measurement of the wear rate (Figure 2.7a). The total wear depth on both specimens was calculated using the width of the contacts as follows:

$$h_t = \frac{1}{2}h_B + \frac{1}{2}h_F = \frac{1}{2}\left\{2r - \sqrt{r^2 - \frac{c_B^2}{4}} - \sqrt{r^2 - \frac{c_F^2}{4}}\right\} \qquad 2.3$$

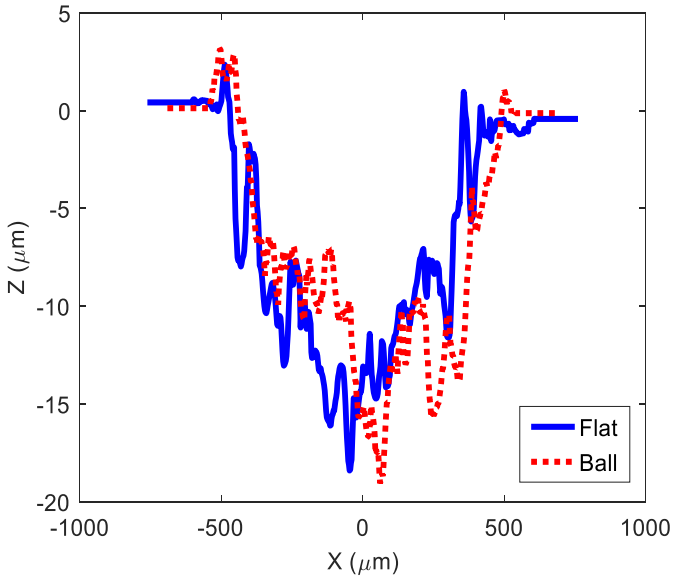

Figure 2.9. Two-dimensional surface profiles of the ball and flat specimens submitted to room temperature and air environment of fretting wear test

As described earlier, the current analysis presents that a bilinear approximation exists between a wear depth and sliding distance while the widely followed Archard's wear law says that scar depth is linearly proportional to the sliding distance. To acquire the Archard constants K1 and K2 in running-in and steady state regimes respectively, the volume loss of balls and flats were calculated separately with the same assumption that for each volume calculation, there was not a significant wear on the other specimen. Based on the geometry, the volume loss was calculated as follows:

$$W_{ball} = \frac{1}{6}\pi h_{ball}(h_{ball}^2 + \frac{3}{4}c^2) \quad 2.4$$

$$W_{flat} = \frac{1}{6}\pi h_{flat}\left(h_{flat}^2 + \frac{3}{4}c^2\right) + 2dch_{flat} \quad 2.5$$

By adding these two volumes together and assuming $h_{ball}=h_{flat}=0.5h$ and then simplifying, the total volume loss can be calculated as:

$$W = W_{ball} + W_{flat} = \frac{1}{12}\pi h^2(6r - h) + 2dh\sqrt{r^2 - (r - \frac{h}{2})^2} \quad 2.6$$

Therefore, the modified Archard equation was used for the current bilinear behavior and by equating equation 2.6 and 2.7 and curve fitting, two different Archard constant were obtained as shown in Figure 2.10.

$$W = \begin{cases} K_1 F(4Nd), & N < N_t \\ K_2 F(4Nd), & N > N_t \end{cases} \quad 2.7$$

Where Nt is the transition cycle from severe to mild wear. K1=1e-3 $\frac{mm^3}{Nm}$ and K2=6.8e-5 $\frac{mm^3}{Nm}$ were calculated by curve fitting.

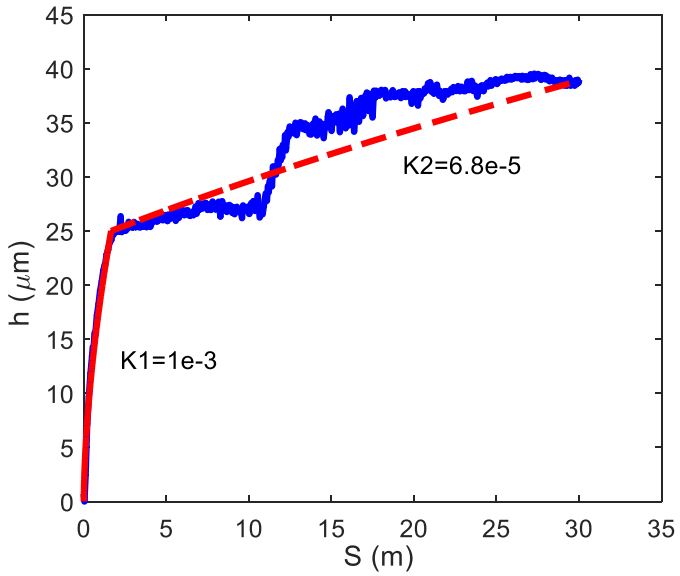

Figure 2.10. Running-in and mild steady state regimes in fretting wear

In-situ measurement of wear depth at elevated temperatures and in air environment has shown that as temperature increased, the wear rate decreased compared to the room temperature test. In helium environment, 750°C showed a higher wear rate compared with the air environment

test but still less than the room temperature test (Figure 2.11). The Archard constant in running-in regime at elevated temperatures and in both environments was calculated to be about K1=1.5e-4 $\frac{mm^3}{Nm}$ which was about an order of magnitude less than the room temperature test. The surface of the contacts at 375°C was believed to have a very small oxidation layer in air environment and even less oxidation in helium environment, therefore, the wear rates were very close to each other. At 750°C and in air, there was a noticeable amount of oxide film which covered the surface of the parts that decreased the COF and wear rate significantly. The highly plastic and adhesive oxide film in the form of Cr2O3 was mentioned in the literature [58] to be the most dominant oxide layer on the surface of Inconel 617 which sustained the abrasion and improved the wear of the material. In fact, the wear resistance of Inconel 617 at high temperature relied on the formation of a continuous Cr2O3 film which was stable enough to protect the surface and acted as a lubricant. At 750°C and in helium, while the amount of O2 was kept below 1% (measured using an oxygen detector inside the chamber), there seem to be a little oxidation on the surface that was measured by EDX. The higher wear rate in helium at 750°C could be associated with the thin thickness and poor adherence of oxides that deteriorated the wear and also degradation of material properties, especially hardness. Although Inconel 617 has a very high hardness resistance at elevated temperature, a little reduction of the material strength at that temperature could be another cause of wear volume loss it has faced. According to the literature, the tensile strength of Inconel 617 decreases by about 25% at 750°C [129,130].

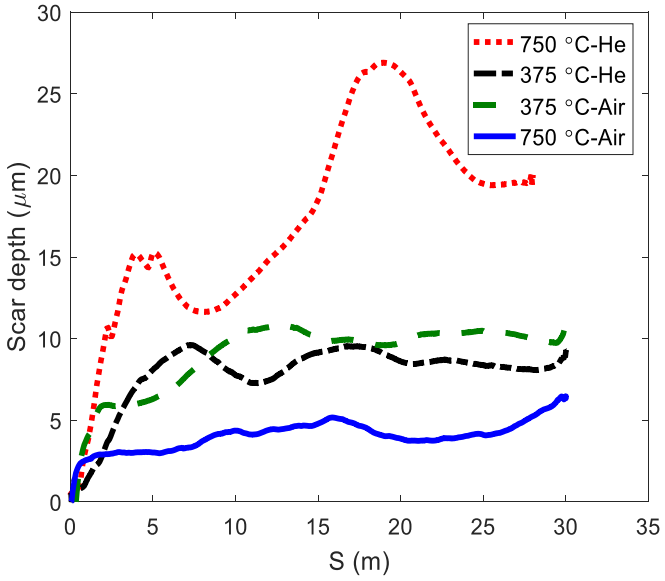

Figure 2.11. In-situ measurement of wear depth at elevated temperatures and air/helium environment

Figure 2.12 illustrates the image of wear scar at 25°C, 375°C, and 750°C for balls in air environment. It was shown that the scar on the ball at room temperature was bigger and more uniform which was because of a higher wear rate while at higher temperatures, it became smaller and non-uniform especially at 750°C which was more elongated in the sliding direction. Furthermore, there were some sintered-like wear particles which adhered to the contact surfaces due to high temperature and pressure. The detached particles were also seen around the contact areas at both room and high-temperature tests which can be mostly attributed to plastic deformation of the surfaces, micro-cutting of adhesive particles, and abrasion [44,65].

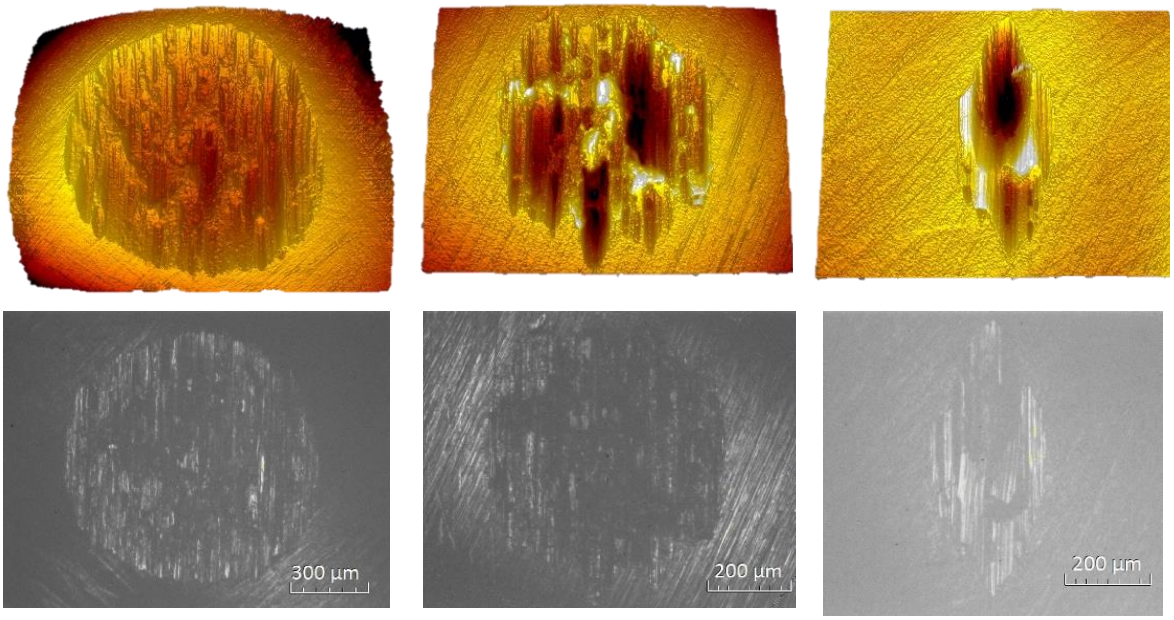

(a) **(b)** **(c)**

Figure 2.12. Optical micrographs and 3D surface reconstruction images of the balls in air environment taken at 30,000 cycles: (a) room temperature, (b) 375 °C, (c) 750 °C

SEM and EDX images are shown in Figure 2.13 and Figure 2.14 for elevated temperatures in both air and helium environments. Strongly sintered-like wear debris particles can be seen at discrete locations that were formed due to the adhesion of debris particles to the scar surfaces which created large agglomerates and promoted ploughing. Adhesion, delamination, and abrasive wear were observed on the surface of this alloy which were related to the formation of hard oxides between the bodies during the fretting test. Near the center of the wear scar, where the pressure was maximum, some localized galling was observed. At 750°C and in air, the surface became glassy and burnished which could be described as the evolution of the glaze layer that made large areas of smooth polished oxide on the surface of oxide debris. The local composition within the surface asperities was captured by EDX. The presence of Ni, Cr, Mo, Co, and etc. was detected in all regions, but the peak intensity was found to vary from region to region. It is worth mentioning that even in the helium environmental condition that the level of oxygen was kept less than 1% during the test, there was some oxidation on the surfaces. The EDX results of a small portion of the scars showed that there was a high percentage of oxide layers (20 % Wt) at 750°C and in air while in helium it declined to a lower amount (14 % Wt). In 750°C, oxidation intensity

was around twice than in 375°C. Moreover, the peak of the Oxygen element was higher at the contact edge than at the contact center and outside the contact as shown in Figure 2.15.

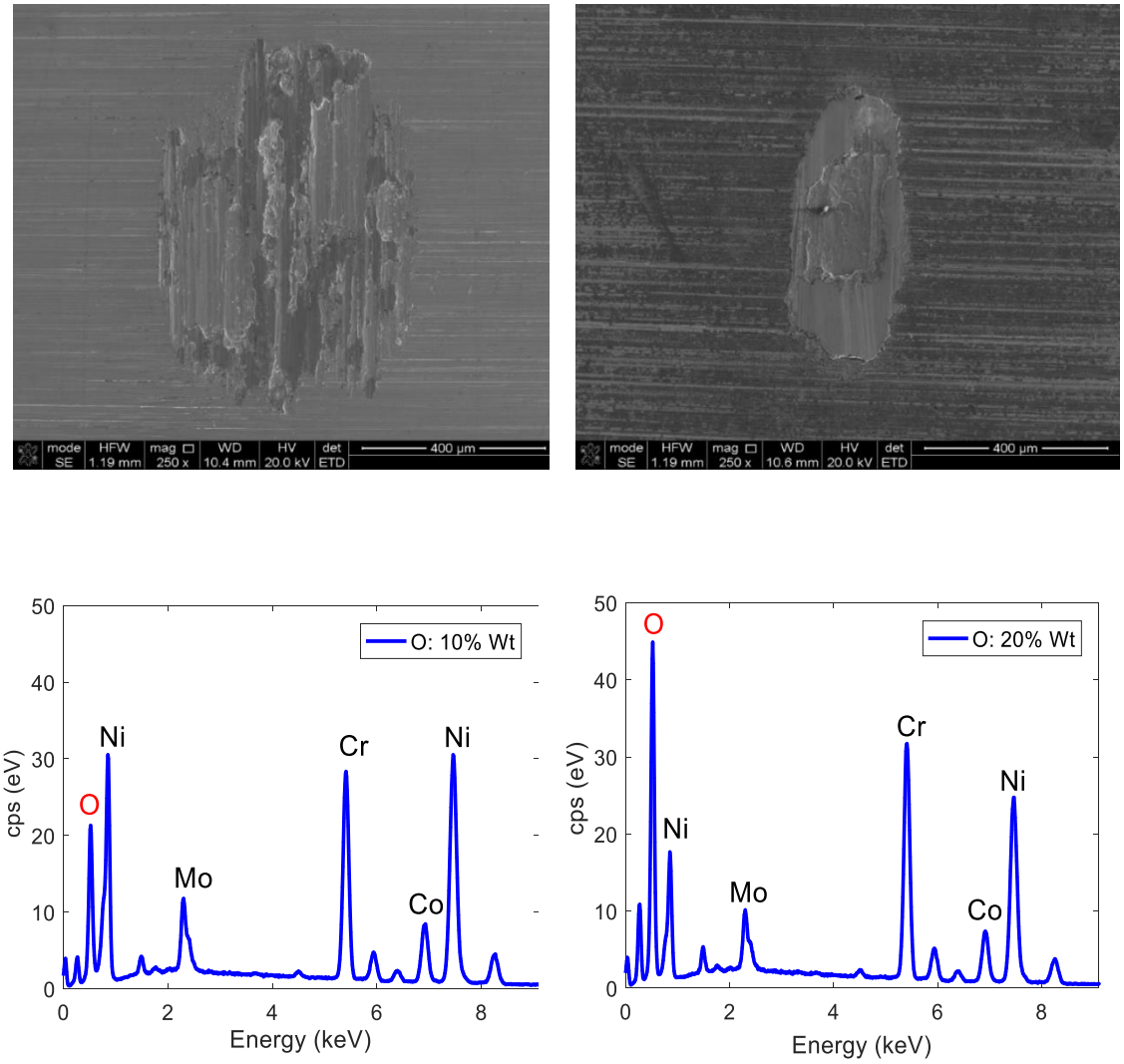

(a) (b)

Figure 2.13. SEM and EDX micrographs of the wear scar on the flat specimen in air environment and elevated temperatures: (a) 375 °C, (b) 750 °C

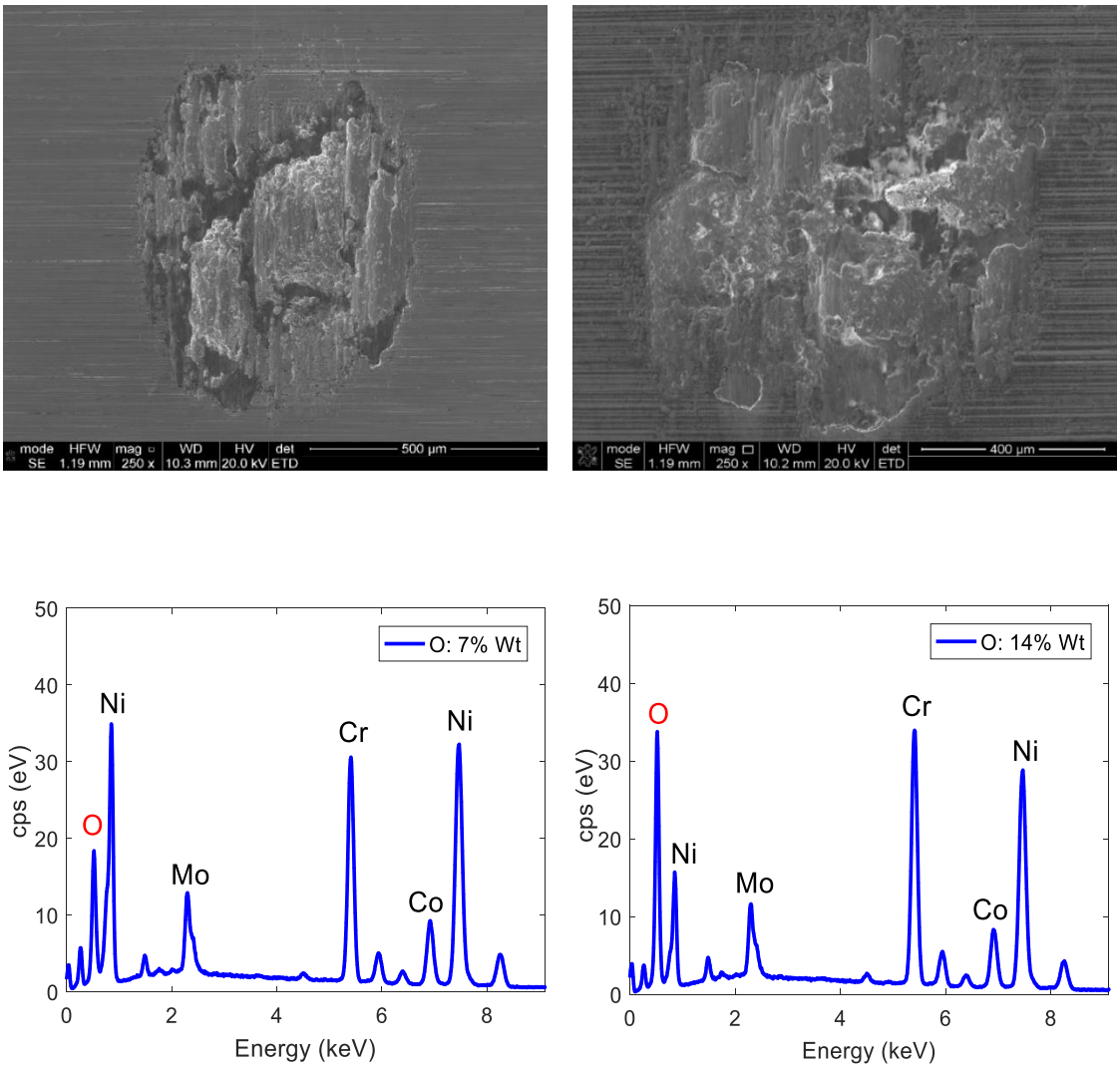

(a) (b)

Figure 2.14. SEM and EDX micrographs of the wear scar on the flat specimen in helium environment and elevated temperatures: (a) 375 °C, (b) 750 °C

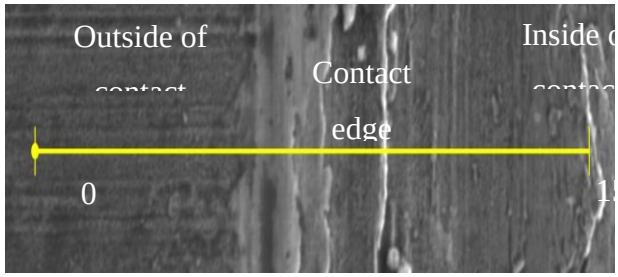

(a)

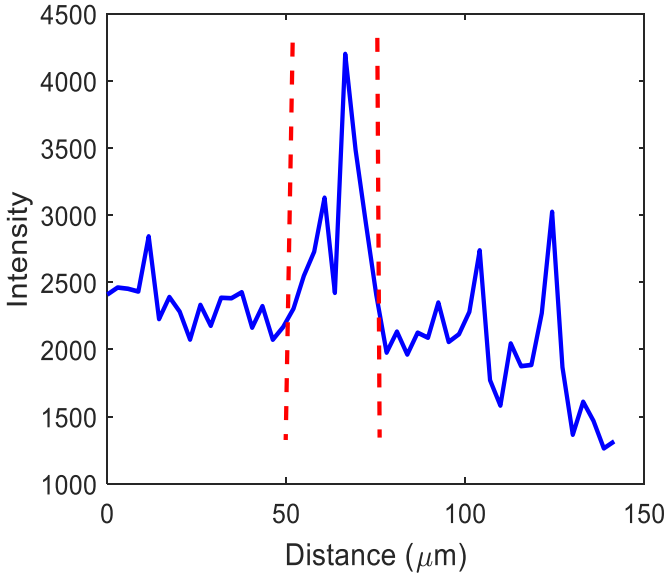

(b)

Figure 2.15. Oxygen intensity at the contact edge for the test at 750 °C and in air

2.4 Conclusions

The objectives of this study were to experimentally investigate the effect of temperature and inert environment on the fretting wear of Inconel 617. Gross sliding fretting tests for the 6.35 mm-diameter ball-on-flat configuration with a normal load of 4 N and displacement of 250 μm were conducted. In-situ fretting wear measurement was used to continuously monitor the change in wear depth of the scar during the process. It was observed that as the number of cycles in both room temperature and in air were increased, the wear rate decreased such that there was a bilinear wear behavior, including a severe running-in wear at the beginning followed by a mild steady state wear. The COF and friction loops were plotted for different conditions of the tests. It was observed that in both helium and air environments, the COF decreased as the temperature increased which was attributed to the change in oxidation and material properties of the specimens at elevated temperatures. Furthermore, the wear rate decreased compared to the room temperature test in both environments. At 750°C, the wear rate in the helium environment was higher than in the air environment. At 750°C in air, a significant amount of stable oxide film covered the surface of the scar, leading to the decrease in wear rate, while in the helium environment, fewer protective oxides particles were present in the contact zone, leading to the increased wear rate of the specimens. Topography and morphology of the scars were performed using SEM and EDX. A high percentage of oxide particles were observed to be adhered to the contact surfaces at 750°C in air, which led to lower friction and wear.

3. EXPERIMENTAL AND NUMERICAL INVESTIGATION OF TORSION FATIGUE OF A NICKEL-BASED ALLOY AT ELEVATED TEMPERATURE

3.1 Introduction

Fatigue has been the subject of much investigation over the past century. Fatigue damage is observed in the form of microcracks, debonding, etc. in the vicinity of stress risers (e.g. inclusions, voids etc.) within the materials. The stress component causing fatigue failure can be normal, shear, or a combination due to a compound state of loading. In order to investigate the shear mode of fatigue failure, torsional fatigue testing has been the subject of many studies [112–115]. Shear mode of failure is of significant importance in triaxial state of stress present for ball and rolling element bearings and machine component which are subject to fretting fatigue [37,84].

Inconel 617 is known for its high-temperature strength and resistance to creep and wear. For this reason, Inconel 617 is widely used in very high-temperature gas-cooled reactors (VHTR). Within the reactor, relative movement between different components such as rods and valves has led to fretting wear and fatigue failures. The fatigue behavior of Inconel 617 at elevated temperatures has been investigated by many researchers. Meurer et al. [131] evaluated the low cycle fatigue (LCF) and HCF of nickel-based alloys at temperatures up to 950°C. They performed the LCF tests under strain control and the HCF under stress control using push-pull loading. They demonstrated that by increasing temperature, the fatigue life of nickel-based alloys decreased. They also noted that strain rate is an important factor for the stress response in LCF. Rao et al. [132] experimentally investigated the influence of time and temperature on LCF of Inconel 617. They found that increasing temperature and decreasing the strain rate resulted in a reduction of LCF life of the material due to the homogenization of slip and the associated increase in the elastic strain. Totemeier et al. [133] studied the creep-fatigue behavior of Inconel 617 in air, vacuum and argon at 1000°C. Burke and Beck [134] performed fully reversed strain controlled LCF tests on Inconel 617 at high temperatures. They indicated that grain boundary sliding and intergranular slip are the main mechanisms of deformation and dislocation at elevated temperatures.

In this chapter, high cycle torsional fatigue behavior of Inconel 617 at 850°C was experimentally and analytically studied. For the experimental aspects of this study, an MTS torsional fatigue test rig was modified by designing custom cooling fins and mechanical gripes to

allow tests at elevated temperatures. The experimental torsional fatigue results demonstrated that fatigue crack initiation occurred due to shear stress followed by normal stress for the propagation. In the analytical aspects of this study, a 3D elastic-plastic FEM was developed to determine the torsional fatigue damage of the material at high temperatures. The microstructure of the material was modeled using Voronoi tessellation and grain boundaries were considered to be weak planes in the material. Continuum damage mechanics approach was applied to simulate the material degradation during the fatigue process. The effects of material plasticity were incorporated by using Mises based plasticity model with a linear kinematic hardening approach. Both stress and accumulated plastic strain-based damage law were included in the model to study the fatigue initiation and propagation in the material. The results demonstrate fatigue lives and crack paths which corroborated well with the high-temperature torsional fatigue experiments.

3.2 Experimental Investigation

In this section, the material and design of the torsion specimen and the procedure of the torsion fatigue tests will be explained in detail.

3.2.1 Torsion Fatigue Test Rig

An MTS torsional fatigue test rig was used to experimentally measure the S-N behavior of Inconel 617 at elevated temperature. Figure 3.1 depicts the modified MTS hydraulic rotary actuator with customized mechanical grips and cooling fins developed for this investigation. This test rig can achieve a total angular displacement of 90° (± 45°) with a resolution of 0.001° measured by an angular displacement transducer. The in-line MTS torque cell with the capacity of ±565 Nm was used to measure the torque applied to the specimen. The rotary actuator and the torque cell are mounted on a rigid flat base with the rotary drive fixed to the base at one end and the torque cell mounted on a slider attached to the base such that allowed for different size specimen. Two customized cooling fins were designed, developed and attached on both ends of the grips to dissipate heat and prevent heat conduction to the actuator and torque cell. These cooling fins were machined from 4140 steel which has a high fatigue and torsional strengths. In order to apply torque to a specimen accurately and repeatedly at high temperature, custom grips were also designed and machined. These grips were made of 310 stainless steel which has

excellent high-temperature properties and resistance to oxidation due to its high chromium and nickel content. These grips had a square pocket which is compatible with the specimen design and two tapped holes which secured the specimen from any rotation and/or slip during the tests.

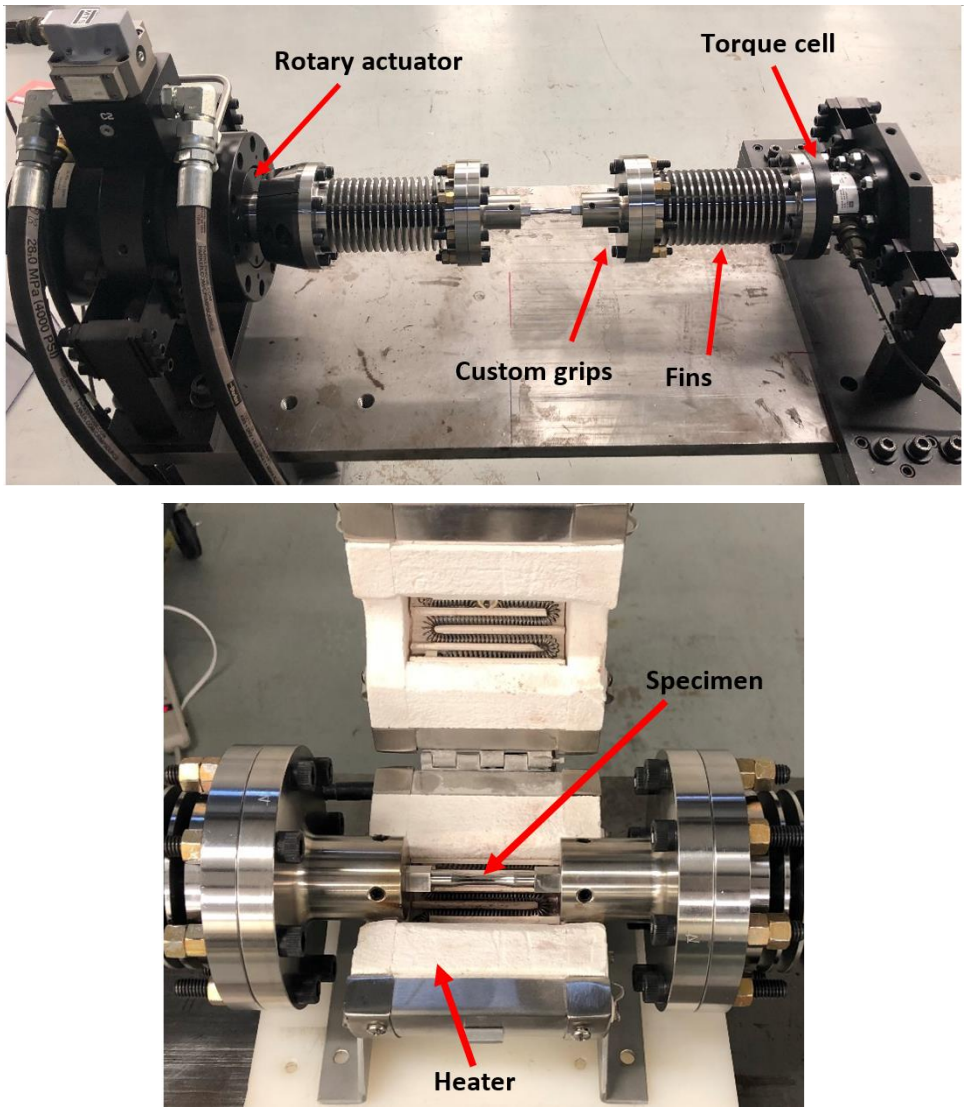

Figure 3.1. The MTS torsion fatigue test rig

3.2.2 Material and Specimen

The material used in this investigation was Inconel 617. Inconel 617 is a nickel-chromium-cobalt-molybdenum alloy. The combination of high-temperature strength and oxidation resistance makes this alloy an excellent candidate for high-temperature applications. Table 3.1 contains the

chemical composition of Inconel 617 [84] and Figure 3.2 illustrates a schematic of the specimen used in this investigation. The specimen had square ends which were fitted into the grips to prevent slip during testing. The specimens are dog bone shaped where the circular cross section gradually reduces toward the region of maximum stress concentration at the center of the gauge section. To observe the grain size of Inconel 617, a specimen was etched in Aqua regia (20% HNO3 and 80% HCl) [133,135]. The specimen was then installed in a scanning electron microscope (SEM) to observe the material microstructure as depicted in Figure 3.3. Using the ASTM E112 [136] standard, the grain size of the Inconel 617 was measured to be 100 μm.

Table 3.1. Composition of Inconel 617 (wt.%)

Ni	Cr	Co	Mo	Al	C	Fe	Mn	Si	S	Ti	Cu	B
44.5 min	20-24	10-15	8-10	0.8-1.5	0.05-0.15	3 max	1 max	1 max	0.015 max	0.6 max	0.5 max	0.006 max

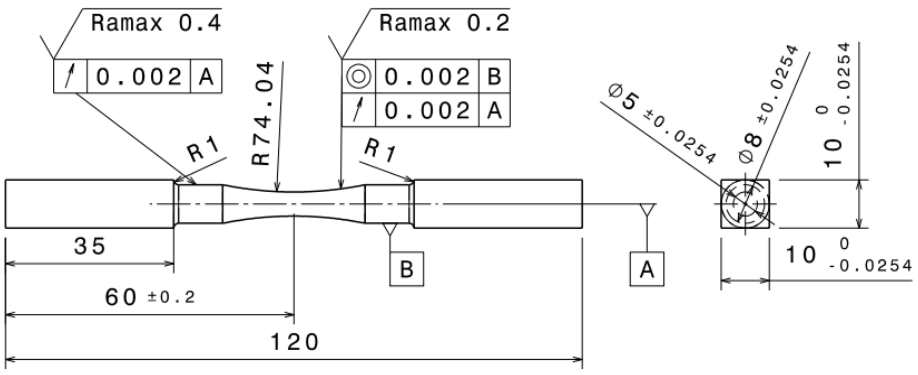

Figure 3.2. Torsion fatigue test specimen geometry (dimension in mm)

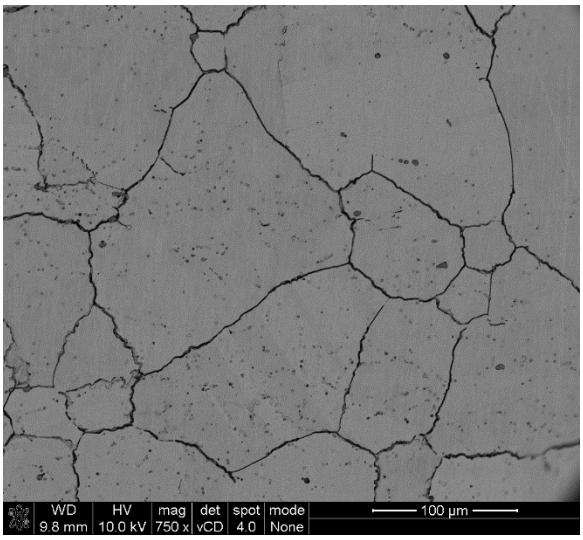

Figure 3.3. SEM of Inconel 617 revealing grain structure

3.2.3 Material and Specimen

Before performing each test, the specimen was aligned into the grips such that there was not any bending moment applied onto the specimen. After alignment, the specimen was heated to 850°C using a heating oven with a resolution of 1°C. Once the specimen reached the desired steady state temperature (850°C), the torsional fatigue test was commenced. First, a monotonic torsional test was conducted to obtain the torsional stress-strain curve of Inconel 617 at 850°C and estimate the torsional yield stress of this material. This experiment was conducted in shear strain control with a shear strain rate of 0.0006 s-1. This monotonic test was not taken to failure because a monotonic shear failure at this high temperature requires hundreds of percent shear strain which was not possible with the limitation of our MTS machine (maximum angle of 90°). After performing the monotonic test, torsional fatigue testing was conducted with the frequency of 40 Hz in a fully reversed (R= -1) load control condition using a sine waveform. This frequency was selected based on the possibility of performing these HCF tests at 850°C in terms of the operation time of the tests and the rotational angle limitation of the machine. Stress amplitudes ranged from 1.12Sys to 1.81Sys which were in HCF region. All specimens were run to failure and the torque and angle changes were recorded during the tests.

3.3 Modeling Approach

In this section, the FE model used for simulating the torsional fatigue test and the damage mechanics approach used in the model are described.

3.3.1 Finite Element Model

ABAQUS finite element software was used to develop a model for the torsional fatigue behavior of Inconel 617 at elevated temperature. A 3D Voronoi tessellation mesh was used to represent the polycrystalline microstructure of the material and to capture damage accumulation, crack initiation, and propagation. Voronoi tessellation has been used by several researchers to model material grain microstructure [137–141]. In this method, a set of randomly Poisson points are used to generate the Voronoi cells. Each cell is the set of all points that are closer to the seed point of the related zone than to any other point in the space. In this model, the average grain size was chosen to be 100 μm to correspond to the experimental measurement of the grains depicted in Figure 3.4. The dimensions of the torsion model were considered based on the gauge section of the experimental specimen such that the size of the model was 20% of the real specimen to have a tenable computational effort. The construction of the Voronoi domain with a curved section is explained in detail [37,142]. After generating the Voronoi domain, the faces of each grain were divided into triangles by connecting the centroid of the polygon to the vertices and all the triangles were connected to the centroid of the Voronoi cell to create the tetrahedras for finite element analysis which is shown in Figure 3.4. Then, These tetrahedras were meshed using linear strain elements (LST).

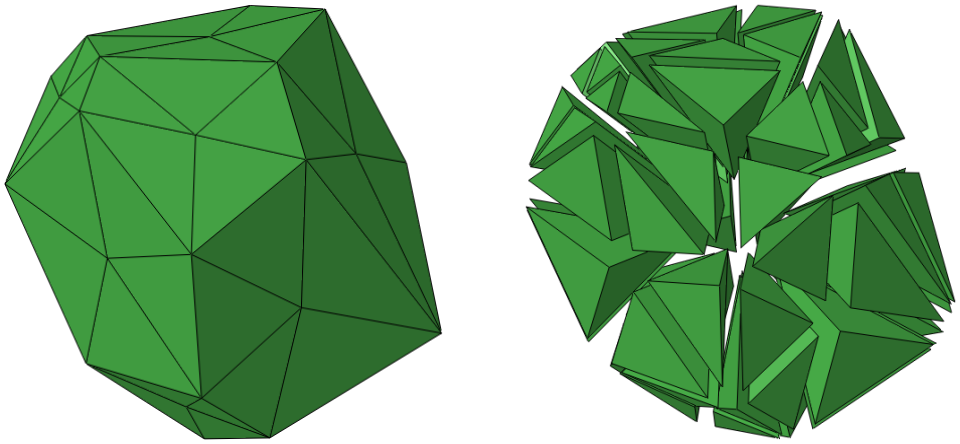

(a) **(b)**

Figure 3.4. A Voronoi grain of the model: a) a grain with the faces divided into the triangles, b) an exploded view

In the current investigation, all the nodes on one end of the model were fixed in the axial direction and the nodes on the other end were coupled to a reference point at the center using kinematic coupling constraints to apply the reversal torque in two steps along two opposite directions. The material properties for Inconel 617 at 850°C were selected based on the literature and data sheets available for this material [129,130] which are shown in Table 3.2.

Table 3.2. Material properties considered for the FE torsional fatigue modeling of Inconel 617 at 850°C

Experimental Parameters	**Value**
Material grain diameter, d_g	100 µm
Undamaged elastic modulus, E	153 GPa
Poisson's ratio, υ	0.3
Yield strength, S_y	280 MPa
Ultimate strength, S_u	370 MPa
Hardening modulus, M	0.2 GPa
Critical damage value, D_{crit}	1

3.3.2 Finite Element Model

In cyclic loading, damage is a process of material deterioration which manifests itself as a gradual degradation of the material through the initiation and propagation of microcracks and voids.

The theory of continuum damage mechanics introduces a convenient framework to consider these microscopic failure mechanisms by defining a thermodynamic state variable D. In an elastic material, the updated constitutive relationship coupled with damage has the following form:

$$\sigma_{ij} = C_{ijkl}(I_{klmn} - D_{klmn})\,\varepsilon_{mn} \tag{3.1}$$

where σ_{ij}, C_{ijkl}, D_{klmn} and ε_{mn} corresponds to the stress, stiffness, damage, and strain tensors respectively. In the case of isotropic damage, Equation 3.1 can be simplified as

$$\sigma_{ij} = C_{ijkl}(1 - D)\,\varepsilon_{kl} \tag{3.2}$$

Where, D ranges from 0 to 1 for an undamaged and fully damaged material, respectively. Equation 2 is based on the effective stress concept in damage mechanics [143]. The stress acting on the undamaged area $\tilde{\sigma}_{ij}$ satisfies the following constitutive laws for the elastic material:

$$\tilde{\sigma}_{ij} = \frac{\sigma_{ij}}{1 - D} = C_{ijkl}\varepsilon_{kl} \tag{3.3}$$

For the elastic-plastic material behavior, Mises yield criterion combined with kinematic hardening and damage form the following constitutive law

$$f = (\tilde{\sigma} - \alpha)_{eq} - S_y \tag{3.4a}$$

$$(\tilde{\sigma} - \alpha)_{eq} = \sqrt{\frac{3}{2}\left(\frac{\sigma_{ij}^D}{1 - D} - \alpha_{ij}\right)\left(\frac{\sigma_{ij}^D}{1 - D} - \alpha_{ij}\right)} \tag{3.4b}$$

where α is the backstress tensor, S_y is the yield strength, and σ^D is the deviatoric stress tensor.

In addition, the plastic strain and kinematic hardening in evolution laws are:

$$\dot{\varepsilon}_{ij}^{p} = \dot{\lambda}\frac{\partial f}{\partial \sigma_{ij}} = \frac{\dot{\lambda}}{1-D}\left(\frac{\sigma_{ij}^{D}}{1-D} - \alpha_{ij}\right) \quad 3.5$$

$$\dot{\alpha}_{ij} = -\hat{C}\dot{\lambda}\frac{\partial f}{\partial \sigma_{ij}} = \hat{C}\dot{\lambda}\left(\frac{\sigma_{ij}^{D}}{1-D} - \alpha_{ij}\right) \quad 3.6$$

where $\dot{\lambda}$ is the plastic multiplier and $\hat{C}$ is a scalar multiplier for hardening. In this investigation, a linear elastic kinematic hardening plastic (ELKP) was assumed to model the stress-strain behavior of Inconel 617 and implemented in a user-defined material (UMAT) subroutine in ABAQUS.

Damage only depends on the state of stress in elastic materials, but it depends on both state of stress and plastic strain in elastic-plastic materials. This current model considered both elastic and plastic damage evolutions laws in case of LCF and HCF analyzes.

In torsion fatigue, experiments demonstrated that crack initiation is due to the shear stress and crack propagation is due to the normal stress [114,115]. In this work, for the elastic damage law, shear stress reversal $\Delta\tau_{critical}$ was considered as the critical stress quantity up to initiation and after that, normal stress reversal was used to propagate the cracks in the model [115]. The maximum shear reversal was calculated using the longest cord method [144]. In this modeling, the stresses and strain fields are resolved along the grain boundaries based on the assumption that Voronoi grain boundaries are the weak planes in which damage happens in intergranular mode. The elastic damage evolution law used for this model is [145]:

$$\frac{dD}{dN} = \left[\frac{\Delta\sigma}{\sigma_r(1-D)}\right]^{m} \quad 3.7$$

where N is the number of cycles, m and σ_r are material parameters, and $\Delta\sigma$ is the critical stress range which is responsible for fatigue damage.

The plastic damage evolution law is based on the maximum von Mises stress (σ_{max}) and accumulated plastic strain over a fatigue cycle ($\dot{P}$) resolved along grain boundaries [143,146] in which:

$$\frac{dD}{dN} = \left[\frac{\sigma_{max}^2}{2ES_0(1-D)^2}\right]^q \dot{p} \qquad 3.8$$

where E is Young's modulus of the undamaged material and S_0 and q are material dependent parameters.

The parameters for both elastic and plastic damage law were calculated based on the experimental torsional fatigue S-N data. Using Basquin's law to curve fit the experimental data, we have

$$\frac{\Delta\tau}{2} = AN^B \qquad 3.9$$

For the elastic damage law, by integrating Equation 7 from D=0 to D=1 and N= 0 to N=N_f (N_f is cycles to failure) and comparing with Equation 9, m and σ_r are calculated for the crack initiation in which shear stress reversal is critical [115].

$$m = -\frac{1}{B}, \quad \sigma_r = 2A(m+1)^{1/m} \qquad 3.10$$

In the case of normal stress reversal (which is equal to shear stress reversal in pure torsion) for the crack propagation, by integrating Equation 7 from D=0 to D=1 and N= 0.9999N_f to N=N_f [115], m and σ_r are as follows:

$$m = -\frac{1}{B}, \quad \sigma_r = 2A(m+1)^{1/m}(10000)^{-1/m} \qquad 3.11$$

For the plastic damage law, a similar procedure was used to obtain the damage parameters S_0 and q by integrating the Equation 8 as follows:

$$\sigma_{max} = \sqrt{3}\left(\frac{\Delta\tau}{2}\right) = \frac{(2ES_0)^{\frac{1}{2}}}{\left(2(2q+1)\Delta\epsilon_p\right)^{1/2q}} N_f^{-1/2q} \qquad 3.12$$

where $\Delta\epsilon_p$ is the range of plastic strain related to σ_{max} over one fatigue cycle. By using kinematic hardening plasticity and plastic flow laws and after some manipulation [146,147], $\Delta\epsilon_p$ can be written as:

$$\Delta\epsilon_p = \frac{\sigma_{max} - S_y}{M+3G} \quad 3.13$$

where M is the hardening modulus and G is the shear modulus. Using equation 12 and selecting two different values for N_f (N_1=10 and N_2=1000 as the plastic strain in fatigue occurs in low cycle fatigue regime [146,148]), S_0 and q can be calculated as follows:

$$q = -\frac{1}{2B}\frac{ln(\frac{N_2\Delta\epsilon_{p2}}{N_1\Delta\epsilon_{p1}})}{ln(\frac{N_2}{N_1})} \quad 3.14a$$

$$S_0 = \frac{1}{2E}\sigma_{max}^2[2(2q+1)N\Delta\epsilon_p]^{1/q} \quad 3.14b$$

It is worth mentioning that both the elastic and the plastic damage evolutions laws were solved simultaneously for each element at any given time and the greater one was chosen to update the fatigue damage in the model.

Rao et al. [132] have indicated that for push-pull LCF of Inconel 617 at 850°C, crack nucleation and propagation occurred mainly in intergranular mode at different strain rates. Burke et al. [134] also discussed the inter/transgranular behavior of Inconel 617 at different high temperatures in LCF. As described earlier in this investigation, the failure mechanism was assumed to be intergranular by considering these paths as weak planes in the material. Furthermore, a technique known as "jump-in-cycle" [115,143,144] was utilized which assumed the damage to be constant over a block of cycles due to the fact that FEM modeling is not computationally possible to run for the actual number of cycles in fatigue process.

3.4 Results and Discussion

In this section, the experimental and numerical results will be discussed in detail.

3.4.1 Experimental Static and Fatigue Tests

Figure 3.5 depicted the monotonic shear stress experienced by Inconel 617 at 850°C with the strain rate of 0.0006 s-1. The slope of the elastic regime (known as shear modulus) was calculated to be G = 59 GPa and the 0.2 percent offset torsional yield stress was Sys= 160 MPa. The results indicate significant hardening which occurred after yielding. Fatigue tests were performed in fully reversed HCF regime at different load levels ranging from 1.12Sys to 1.81Sys with the frequency of 40 Hz at 850°C. A power law curve fit was used to demonstrate the general trend of the results as shown in Figure 3.6. According to the literature, the effect of frequency is noticeable in high-temperature fatigue tests, especially for LCF regime. Rao et al. [149] determined the effects of strain rate on LCF of Inconel 617 at 950°C. They observed a remarkable reduction in the maximum tension and compression portions of the hysteresis loop and increase of plastic deformation in each cycle by reducing the strain rate. This yielded to a gradual reduction in fatigue life. Mall and Engesser [150] studied the effect of frequency on fatigue behavior of a carbon fiber reinforced silicon carbide composite at high temperatures. They found that by increasing the frequency, cycles to failure at a considered stress level increased.

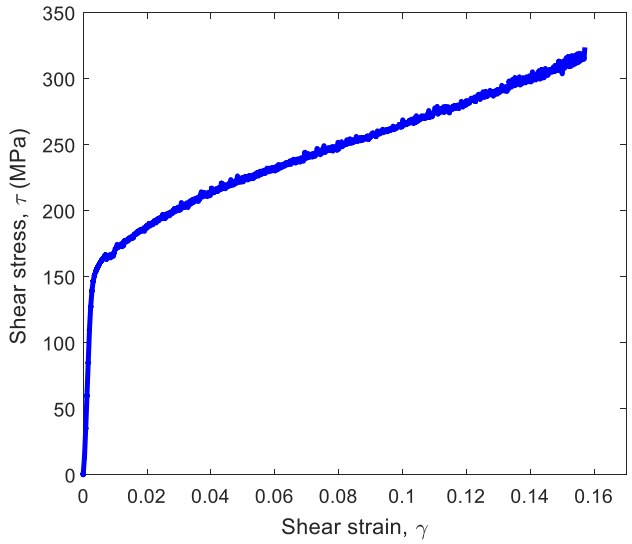

Figure 3.5. Monotonic torsional test experienced by Inconel 617 at 850°C

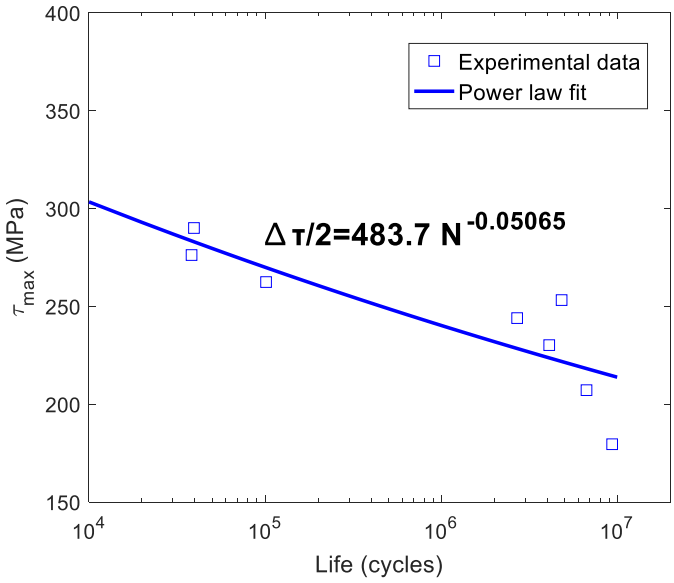

Figure 3.6. S-N data of torsional fatigue tests for Inconel 617 at 850°C

3.4.2 Experimental Static and Fatigue Tests

In order to study the failed surfaces of Inconel 617 in torsion fatigue tests at elevated temperature, optical analysis was performed by taking the image of the fracture surfaces of the samples. In HCF, the strain energy applied to the specimen is low and thus cracks only initiate on the weak planes or material defect locations. As the number of cycles increases, one of these randomly distributed sites becomes critical and forms the crack path to final failure. The final failure surface of the specimen in the current study demonstrated the commonly observed helical fracture planes. These critical planes are at 45° angle with the specimen axis which was the principal normal stress plane angle in pure torsion. Figure 3.7 illustrates a broken specimen. It is to be noted that the specimens which failed (broke) at higher cycles had a smooth and well-defined failure surface than the ones which failed at the lower number of cycles. The failure surface is usually created of three principal stages: crack initiation, crack growth and final failure which are demonstrated in Figure 3.8. In pure torsional fatigue tests, the crack starts at the exterior region of the geometry in the gauge section area which can be observed on an edge parallel or perpendicular to the sample axis where the shear stress reversal is dominant [114]. The propagation marks are a series of ridges which begin from the crack initiation point. These marks show the crack growth stage. The majority portion of the fatigue life is related to the mesoscale

crack initiation [114,115]. Considering the number of cycles corresponding to 2% drop off in the peak torsional load [149] as the initiation life in the current experiment revealed that just 0.1% of the total life was associated with the propagation life. The helical shape of the failure surface depicts that normal stress was dominant in propagation as normal stresses were maximum on these planes in pure torsion. The final failure area is the last stage which is at the opposite side of the crack initiation location. Due to the sudden and catastrophic failure in this region, the surface on this site was rougher than the propagation region [151,152].

(a) **(b)**

Figure 3.7. Comparison of fracture surfaces in torsional fatigue tests of Inconel 617 at 850°C: a) failed at N= 39.5k cycles b) failed at N=9.4m cycles

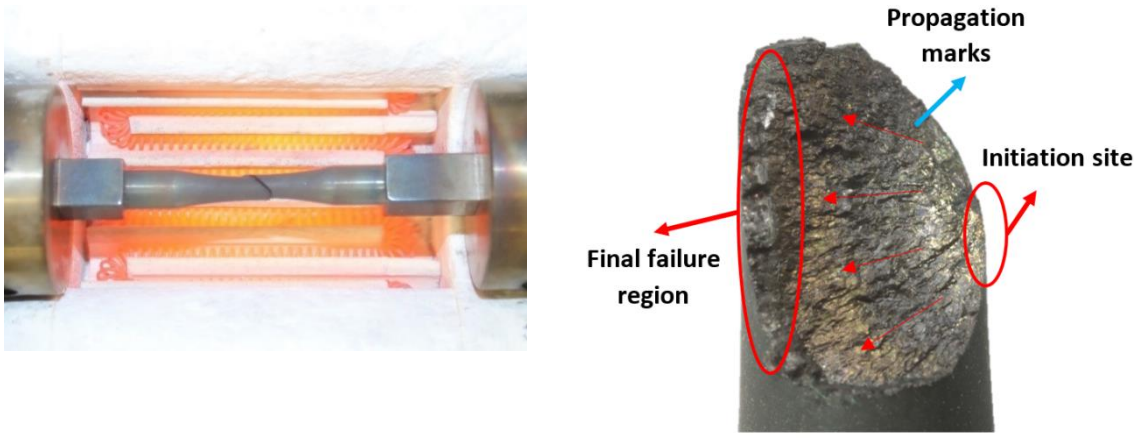

(a) **(b)**

Figure 3.8. Detailed image of high cycle torsional fatigue of Inconel 617 specimen at 850°C: a) Broken specimen in a test, b) fracture surface of the specimen

Due to the high temperature condition of the tests, the amount of oxidation on the specimens was quite noticeable. Influence of oxidation on crack initiation and propagation in high-temperature fatigue tests of Inconel 617 was broadly discussed by Rao et al. [132]. They mentioned that crack branching was associated with oxidation and because the oxides are brittle, the crack initiation occurred in oxides located on the surface connected grain boundaries.

3.4.3 Analytical Results

A finite element model was developed to model torsional fatigue of dog bone specimen and corroborate experimental and analytical results. Ten different domains were generated using the Voronoi tessellation and subjected to fully reversed torsional loading. Figure 3.9 illustrates the stress contours of the model before any element reached the critical damage (crack initiation). In HCF, the majority of life is spent during the initiation of the crack. Several domains were modelled at different stress levels and corresponding fatigue lives are shown in Figure 3.10 It demonstrates that the predicted fatigue life obtained from the FE model is in a good agreement with the fatigue (S-N) lives obtained from the experiments and the deviation in the results is due the randomness in the microstructure of Voronoi tessellation torsion model. Continuation of the cyclic fatigue load on the model after crack initiation, damage localized, and cracks propagated along intergranular week planes. Figure 3.11 illustrates the crack growth patterns at 1.12Sys. The location of the crack initiation was consistent with the location of maximum shear stress and the subsequent crack propagations were at almost 45o with respect to the specimen axis. The crack propagation life also indicated that 99.9% of life was spent in crack initiation which was consistent with the experimental observations [115,132,149].

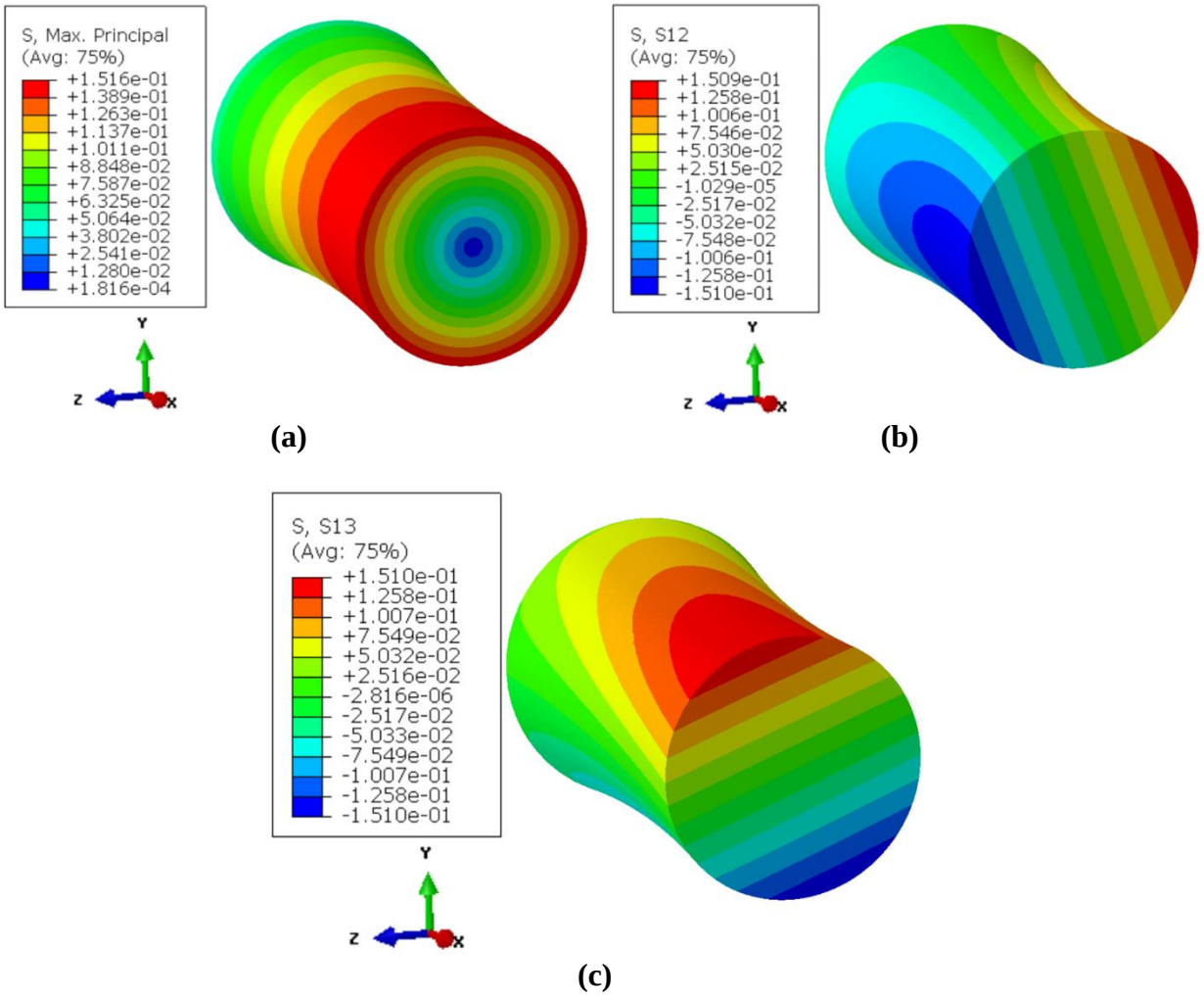

Figure 3.9. Stress contours on a cut section of the torsion model: a) von Mises, b) S12, c) S13

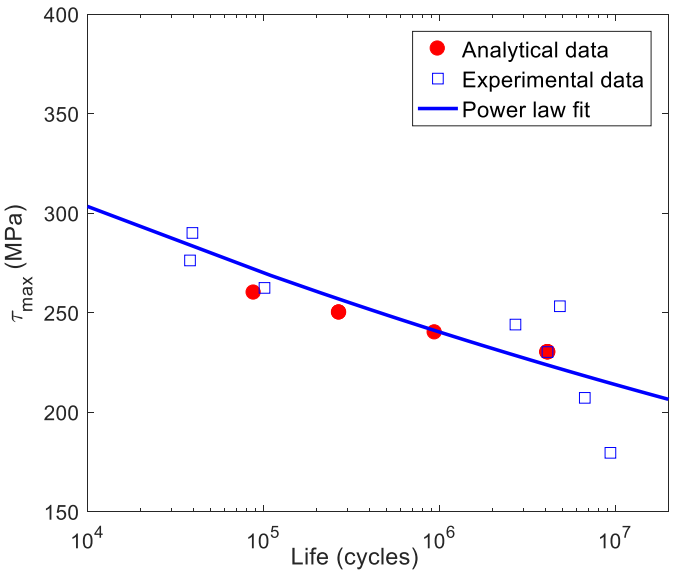

Figure 3.10. Comparison of FEM life prediction with the experimental S-N curve for Inconel 617 at 850°C

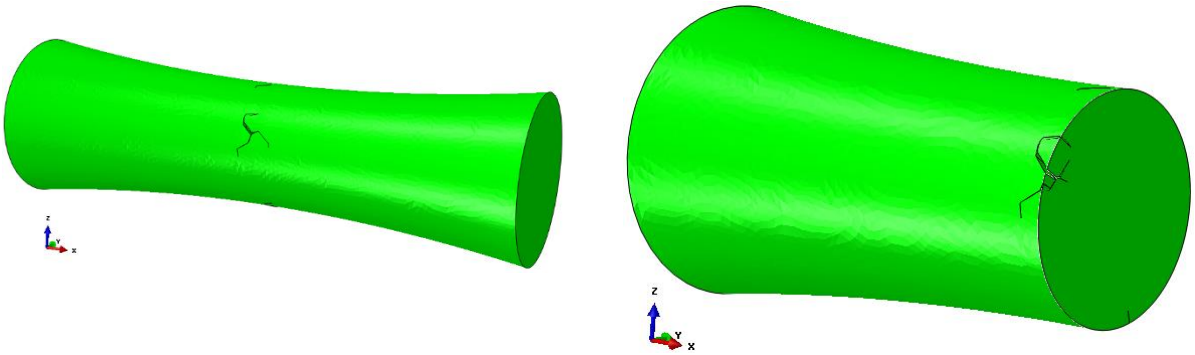

(a) **(b)**

Figure 3.11. Crack propagation map in torsional fatigue FE modeling of Inconel 617 at 850°C: a) whole model, b) cut section of the model

3.5 Conclusions

The objectives of this study were to experimentally and analytically investigate the effect of temperature on torsional fatigue of Inconel 617. In the experimental aspect, a modified MTS machine was used by to obtain torsional fatigue (SN) results under fully revered conditions at 850°C. The MTS machine was modified by high temperature gripers with cooling fins. The final failure surface of the test specimen depicted that they had similar failure modes which was observed by helical fracture planes at 45° angle with the specimen torsional axis. The helical shape of the failure surface depicted that normal stress was dominant in propagation as normal stresses were maximum on these planes in pure torsion. In the analytical aspect of this study, a 3D elastic-plastic FEM was developed to investigate the torsional fatigue damage of the material at high temperatures. Voronoi tessellation was used to model the microstructure of the material and boundaries of the grains were considered to be weak planes in the material. Continuum damage mechanics approach was applied to simulate the material degradation during the fatigue process. Mises based plasticity model combined with a linear kinematic hardening approach was used to include the influence of plasticity into the model. The model predicted fatigue lives and crack growth path which corroborated well with the high-temperature torsional fatigue experiments

4. A NOVEL 3D FINITE ELEMENT MODEL TO SIMULATE THIRD BODY EFFECTS ON FRETTING WEAR OF HERTZIAN POINT CONTACT IN PARTIAL SLIP

4.1 Introduction

In this chapter, a 3D Hertzian point contact model was developed using FEM to study the effect of third body phenomenon in partial slip fretting wear. Both the first bodies and the third body were considered to be deformable with the elastic-plastic material properties. Some simplified assumptions were made due to the complexity of the problem such as there was no interaction between the particles in contact; all the particles were spherical with the same size. The wear particles were located in the slip zone of the contact and a partial slip regime was simulated. In this modeling, the effect of third body on the contact pressure and shear stress was investigated in detail. Also, the effects of number of particles on the contact pressure and total load carried by particles were evaluated. The influence of the number of third body particles and material properties such as modulus of elasticity, hardening modulus, and yield strength were studied. Fretting loops for with and without wear particles were compared and the relation between the number of cycles and the hardening process was obtained. Finally, wear debris with different material properties than first bodies were studied to represent the influence of oxidization of the particles.

4.2 Modeling Approach

An FE model was developed to evaluate the effect of the third body in the partial slip regime of the fretting phenomenon. A 3D Hertzian point contact geometry was created. Some of the contact properties including contact pressure and stick-slip behavior were studied using the ABAQUS finite element software. The upper and lower first bodies were modeled as a ball on a flat specimen respectively and both bodies were considered to be deformable. The lower body was fixed in all directions and a uniform contact pressure was applied on the upper body to bring these two bodies into contact. The same boundary conditions have been applied previously by other authors [82,83]. Four-node tetrahedral elements (C3D4) were used to mesh the bodies. All the bodies were partitioned to have a finer mesh near the contact and courser mesh away from the

contact to reduce computational time and have accurate results. In addition, just half of the model was simulated to reduce the number of elements. For the contact between the different parts in the FE model, the non-linear penalty method was applied. Although the Lagrange method could provide more accurate stick-slip results, the penalty method has a better convergence rate. In order to obtain a good accuracy in the penalty method, a slip tolerance of 0.005 was selected in the model for the interaction between bodies. Figure 4.1 demonstrates the schematic of the model developed for this investigation. Before adding the wear scar and particles to the model, the model and mesh quality were verified by considering a linear elastic material model and comparing the Hertzian pressure and internal stresses with the theory for the point contact as shown in Figure 4.2. This verified the accuracy of the mesh, domain size, and boundary conditions. The contact pressure in the Hertzian point contact can be obtained using the following equation:

$$P = P_{max}[1 - \frac{r^2}{a^2}]^{0.5} \quad 4.1$$

where r is the location in the contact, a is the Hertzian half contact width, and P_{max} is the maximum Hertzian pressure. In this modeling, P_{max}=1 GPa and a=100 μm were kept constant for the simulation and consequently, the diameter of the upper body was calculated to be D=14 mm. To simulate the partial slip regime in fretting, after achieving the load balance between the first bodies, the displacement amplitude of δ=0.5 μm was applied to the upper body using a sinusoidal function. All the steps in the partial slip fretting wear are shown in Figure 4.3. The stick zone size (c) was also obtained by the following equation:

$$\frac{c}{a} = \sqrt[3]{1 - \frac{Q}{\mu W}} \quad 4.2$$

where Q is the shear force, W is the normal force, and μ is the coefficient of friction (COF). COF was set to 0.6 in this work and the values of c was kept constant for the simulation which simplified the third body study in contact. After obtaining the value of Q from the FE model and substituting in Equation 2, the stick zone size was calculated to be c=65 μm. This point is corresponding to the maximum tangential force in a cycle. The calculated c correlated well with the theoretical result as shown in Figure 4.4. Figure 4.5 also shows the evaluated stick-slip zone on the lower body at the point of maximum displacement Table 4.1 summarizes all the parameters related to the FE model.

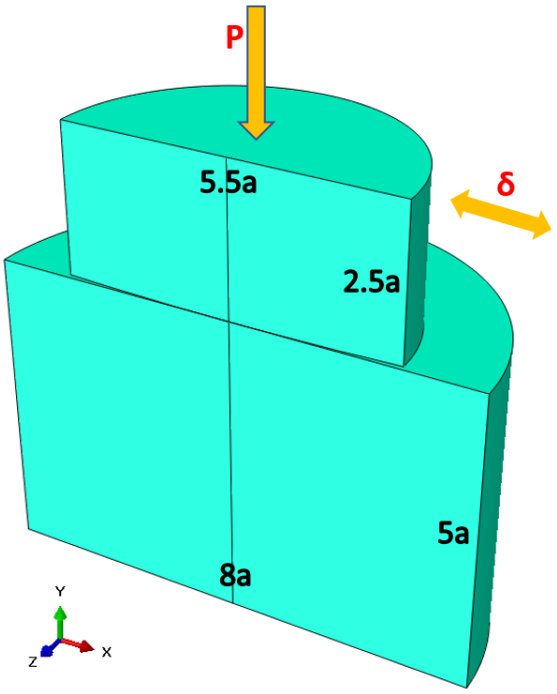

Figure 4.1. The 3D FE model description with showing the load and displacement (a is the half contact size)

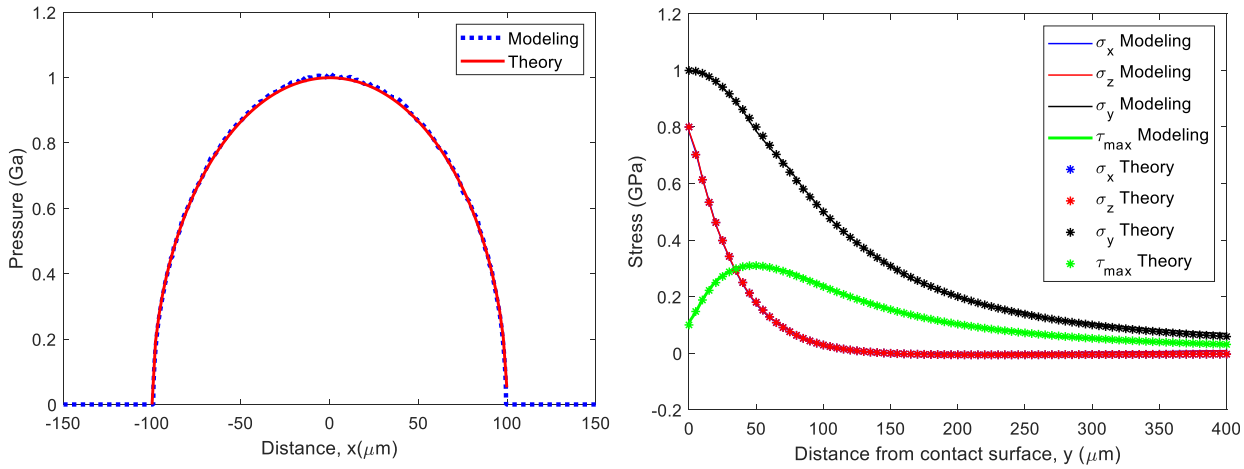

Figure 4.2. Comparison of (a) contact pressures and (b) internal stresses in the FE Hertzian point contact model with theory

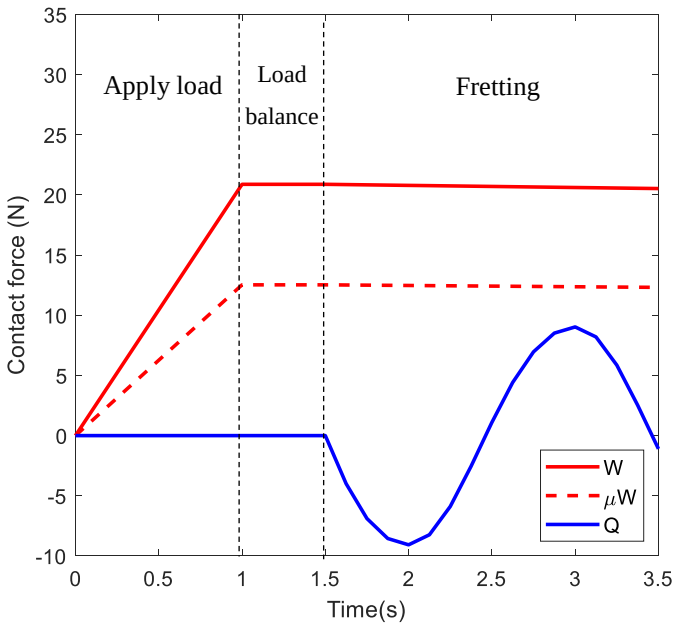

Figure 4.3. Contact forces obtained in FE model of Hertzian point contact

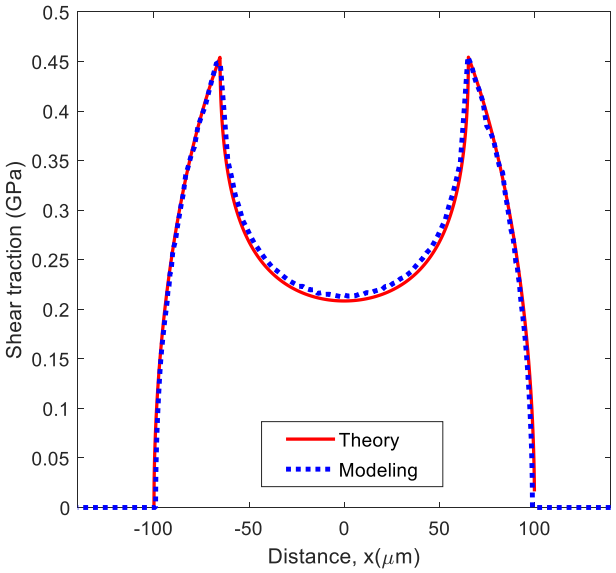

Figure 4.4. Shear tractions occurring during the fretting cycle at the point of maximum displacement

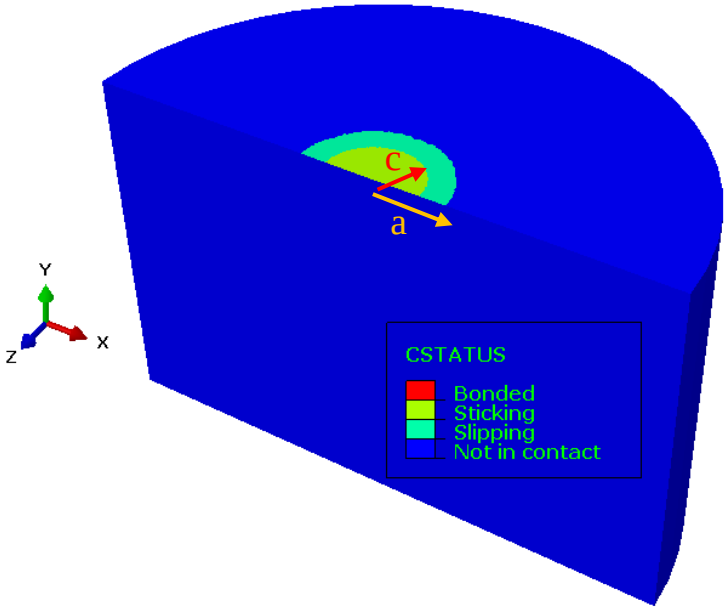

Figure 4.5. Evaluation of Stick zone size from a Hertzian point contact model on the lower body. The value is measured at the point of maximum displacement

Table 4.1. Parameters used in the fretting wear analysis

Parameters	Value
Maximum Hertzian pressure, P_{max} (GPa)	1
Half contact width, a (μm)	100
Stick zone size, c (μm)	65
Displacement amplitude, δ (μm)	0.5
Coefficient of friction, μ	0.6

After calculating the stick and slip zone sizes for the fretting model without any particle, the final worn surface was obtained theoretically similar to the method proposed by Hills et al. [17,83]. The wear scar was located in the slip zone without changing the contact surface in the stick zone for the first bodies.

In the partial slip fretting wear, the wear particles detach from the first bodies and form the wear scar. In this investigation, the wear particles were considered to be deformable similar to the first bodies and they were placed in the worn surface which was created in the slip zone of the first bodies. This is shown schematically in Figure 4.6. Two types of wear debris have been reported in literature: flake which has a uniform thickness and non-flake which can be spherical, cylindrical, or irregular shapes [65]. Zanoria et al. [153] showed that the initial wear particles have mostly spherical, cylindrical, or needle-like shapes due to the reciprocating motion of the first bodies. As the number of cycles increase, these particle aggregate and create denser debris with a change in the shape and size, or they may break into finer particles because of crack and plastic deformation on particles. The agglomeration of wear debris is an important topic in fretting wear studies but combining agglomeration of the third body along with fretting will cause a significant increase in computational time. In this investigation, spherical wear particles were modeled as separate parts without any interaction with each other. In fact, it is assumed that the interaction between the first bodies with each other and with the third body is more significant than the interaction of the third body with each other. These wear particles had the same size (Dp=0.4 μm) and were placed symmetrically in the scar between first bodies to understand their effects on the contact parameters in the initial stage of the wear process. The size of the wear particles can be from a few nanometers to several microns depending on the contact situation and material properties [83]. The objective of this investigation was to study the initial stage of the fretting including wear debris which is critical to understand the subsequent interaction and evolution of wear.

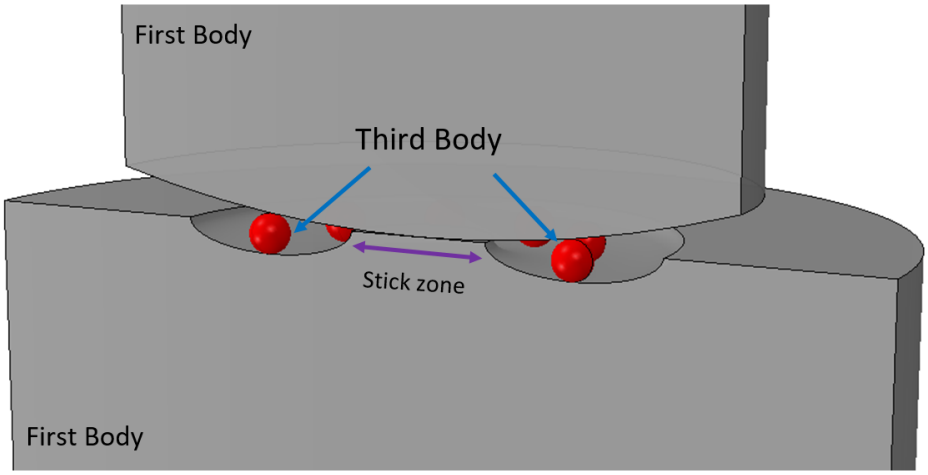

Figure 4.6. Schematic of the contact surfaces showing the worn contact surface with third body particles

In the generation of wear particles in fretting, oxidation and corrosion can also accompany the mechanical process and therefore, the properties of the third body could be different from first bodies. In this simulation, first, it was assumed that the third body has the same material properties as first bodies. In the last section of the paper, the effect of different material properties of debris was also analyzed.

4.3 Results and Discussion

In this section, the results for different case of elastic and plastic models with different properties will be discussed.

4.3.1 Analysis of the Third Body with Linear Elastic Material Model

As discussed earlier, the model was validated using the linear elastic properties of steel (E=200 GPa, ν=0.3) with theory in the absence of particles (Figure 4.2). In the next step, the FE model including two particles was considered. These particles were located symmetrically at the edge of the Hertzian contact. As shown in Figure 4.7, a considerable increase was observed in the contact pressure where the particles were located. These wear particles served as stress risers due to their small size compared to the contact size of first bodies. In addition, there was a rise at the edge of the scar where the stick zone ended, this is due to the stress concentration at the sharp edge. Also,

due to the high local pressure on the particles, sever deformation occurred on the particles and the non-linear geometry option was activated for this modeling.

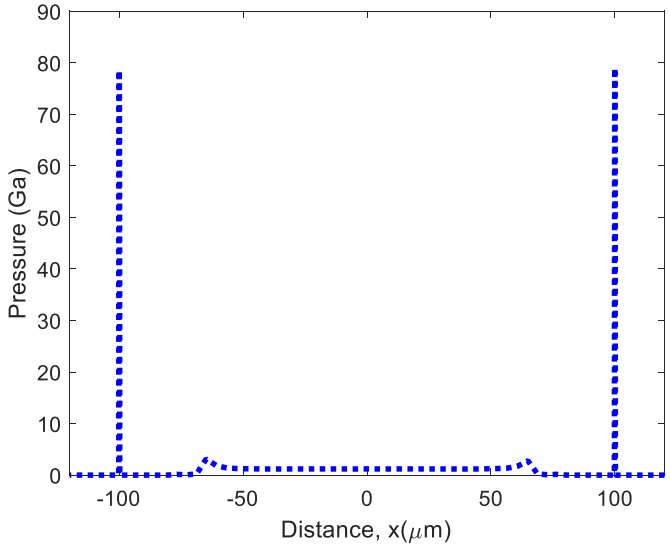

Figure 4.7. Contact pressure of a worn Hertzian point contact with two third bodies for a linear elastic material model

In the model with particles, three interaction surfaces exist: contact between the spherical and the flat surfaces, contact between the spherical surface and the third body, and contact between the flat surface and the third body. By applying the load to the ball, the first bodies came into contact and as the normal load was increased, the third body came into contact with both first bodies as well. Figure 4.8a illustrates the evolution of contact force with the time of approach for the contact of the third body with first bodies for a linear elastic model. It is worth mentioning that the force balance was achieved at the end of this step with a duration of 1 s. It is shown that the force between the third body and the upper first body (ball) was equal to the force between the third body and the lower first body (flat) which confirmed the force balance in the contact. Furthermore, the maximum force on each third body was about 5 mN which was smaller than the total force between the first bodies without particles (W=21 N). In reality that there are thousands of wear particles in contact, the summation of all of those forces would be significant such that the majority of the load could be carried by the particles instead of the first bodies. Figure 4.8b depicts the deformation with the time of approach for different contacts in a linear elastic model. The results for the Hertzian point contact in the absence of the third body was also included as a

reference. Although the contact between first bodies and the third body occurred at about 0.6 s according to Figure 4.8a, some deformation occurred on the third body before this time as shown in Figure 4.8b. This is due to the deformation of the first bodies. Furthermore, the deformation on the upper first body (ball) was higher than the lower first body (flat) due to the higher radius of the curvature in the lower first body (Rflat=∞).

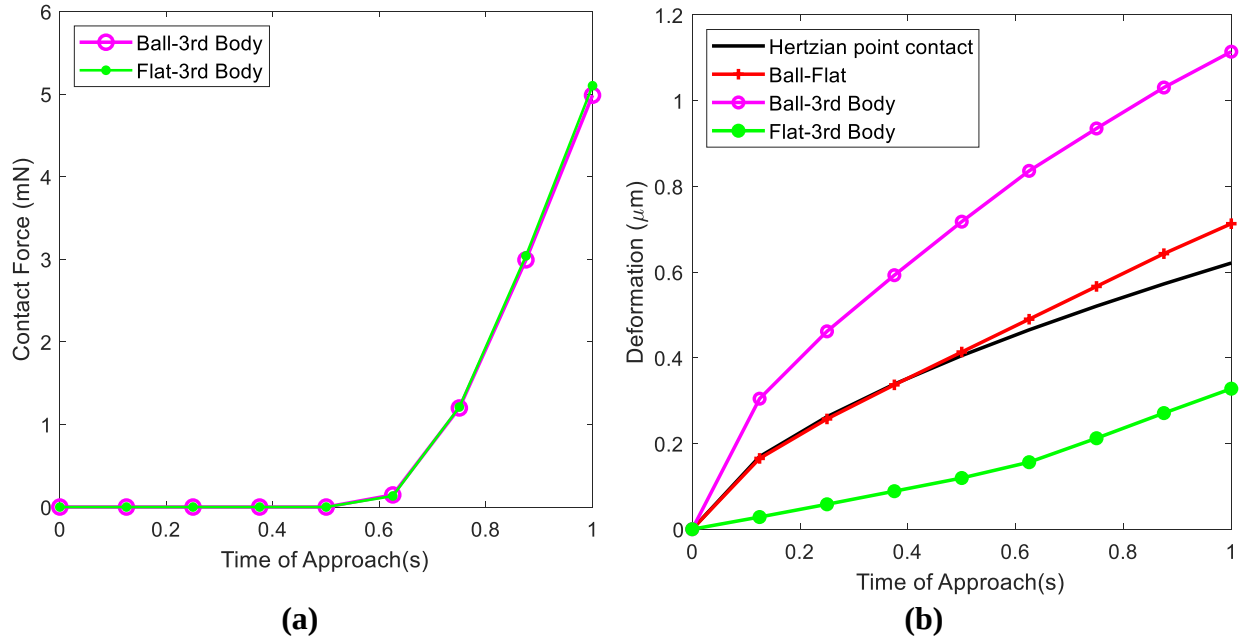

Figure 4.8. Comparison of (a) Force vs time of approach and (b) Displacement versus time of approach for different contact surfaces in an linear elastic model with two wear particles

By combining the force and deformation results in Figure 4.9, the force-deformation results of bodies are illustrated in Figure 4.9. In this linear elastic model with two wear particles, the majority of the load was supported by the first bodies but as the number of particles increases in the contact, more load will be carried by the third body which affects the surface stresses and wear of the first bodies.

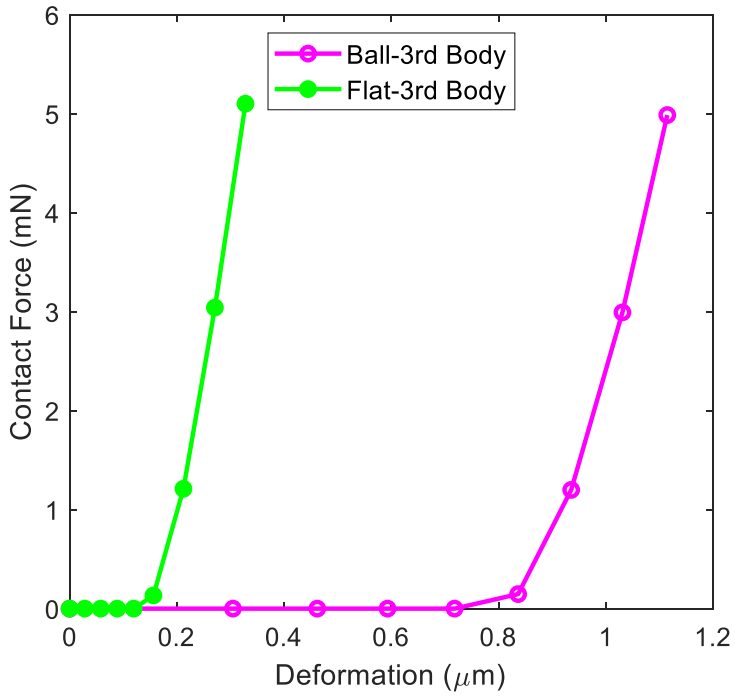

Figure 4.9. Force-deformation curves for different contact surfaces in the FE Elastic model of third bodies in Hertzian point contact.

4.3.2 Analysis of the Third Body with an Elastic-plastic Material Model

As shown in Figure 4.7, the linear elastic model of the third body resulted in a stress concentration at the location of wear particles. At this local high contact pressure, the material technically cannot be elastic anymore and significant plastic deformation occurs on the bodies. Fretting wear has a cyclic loading due to the sinusoidal motion and has stress reversals in the plastic range. Therefore, a kinematic hardening model would be a more appropriate model to predict its behavior similar to the experiments. To this end, an elastic linear kinematic plastic (ELKP) model was used for the rest of the simulations. As shown in Figure 4.10, a bilinear stress-strain relationship was considered for a 52100 steel in this model [154]. In this material model, the modulus of elasticity is E=200 GPa, the hardening modulus is M=10 GPa, and the yield strength is Sy=2.03 GPa.

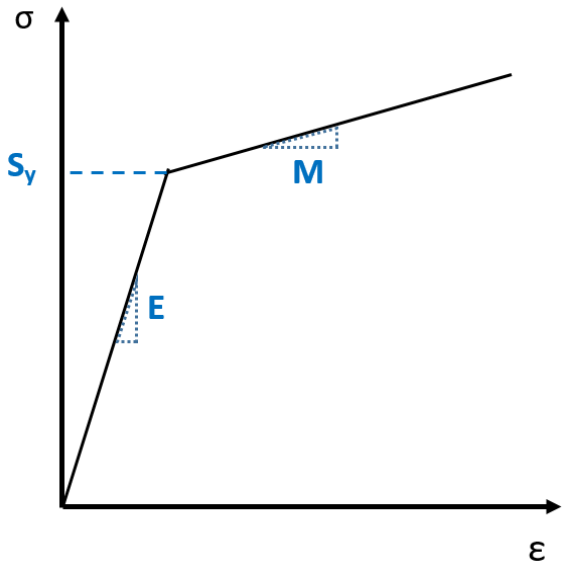

Figure 4.10. Stress–strain curve for the Elastic Linear Kinematic Plastic material (ELKP)

Figure 4.11 depicts the difference between the Hertzian point contact centerline pressure of the elastic-plastic model and the linear elastic model. Although the parabolic profiles of the contact pressure on the first bodies were almost the same for both materials, there was a significant reduction of the pressure on the location of particles for the elastic-plastic model. This was due to the yield strength limit which was defined for the elastic-plastic model. Figure 4.12a depicts the difference between force-deformation plots of the linear elastic and elastic-plastic models for the third body. Elastic-plastic properties resulted in having a lower contact stiffness of third body particles and therefore, lower stresses were observed for this model than the pure elastic model. The difference of force-deformation for the first bodies contact was not significant as they were in the elastic region for both materials (Figure 4.12b). The difference between the force of the elastic and elastic-plastic models was in the order of a few milli-Newtons according to the third body force and the load balance but it is not distinguishable in Figure 4.12b due to the Newton unit used in the plot.

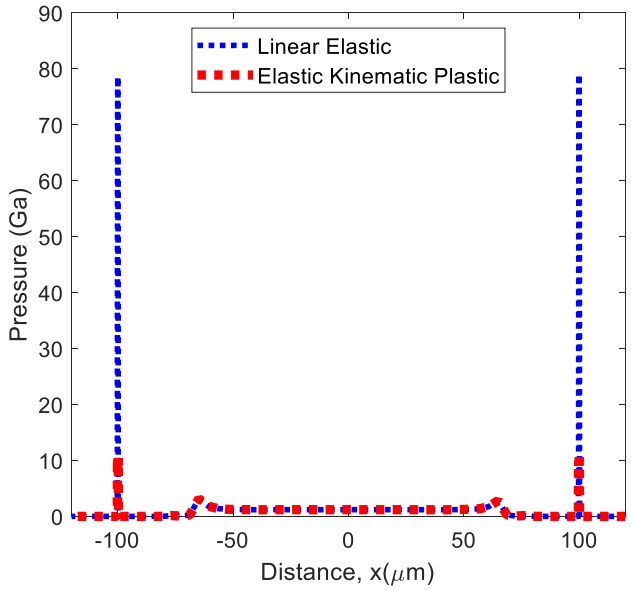

Figure 4.11. Comparison of centerline contact pressure for linear elastic and elastic–plastic material models including two particles.

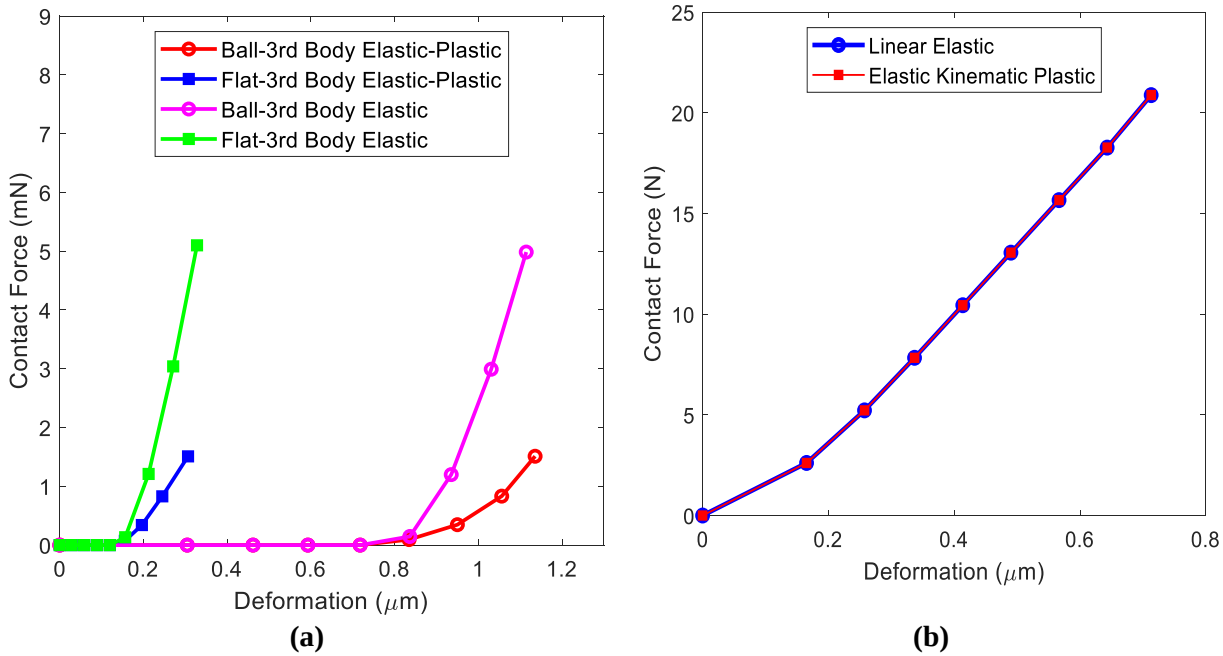

(a) **(b)**

Figure 4.12. (a) Force-deformation relationship for linear elastic and elastic-plastic material models including two wear particles at the contact of two first bodies. (b) Force-deformation relationship for linear elastic and elastic-plastic material model at the contact of surfaces involving third bodies

As discussed earlier, for the model with just two particles, most percentages of the load in the contact were captured by the first bodies but in reality that there are thousands of particles and in different locations of the slip zone. Therefore, a noticeable amount of load could perhaps be carried by these third body particles which could affect the wear significantly. As it was not computationally possible to put a lot of particles in the contact, FE model with different number of wear particles were developed n=2, 10, 18, and 36). All these particles were located at the edge of the half contact. It is shown in Figure 4.13 that as the number of particles increased, more load was carried by the particles and it could be significant when there are a lot more particles and in different locations of the contact.

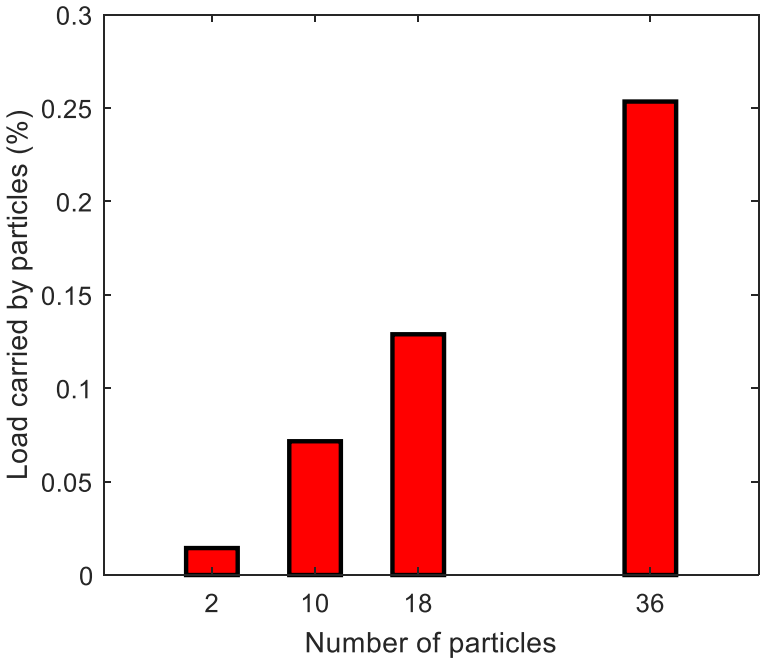

Figure 4.13. Total load carried by wear particles in an elastic-plastic model.

The large plastic deformation of the third body in an elastic-plastic model led to an oval and platelet type shape of the particles. It is demonstrated in Figure 4.14 that in the elastic-plastic investigation, the particle deforms more than the elastic model. Platelet deformation of the wear particles was investigated experimentally by different authors [155–157]. The evolution of the third body shape and the equivalent plastic strain of the third body in contact are shown in Figure 4.15. As the particle underwent stresses higher than yielding, significant plastic strain and

consequently a permanent deformation occurred on the third body. During the wear process, the wear particles experience severe normal and shear stress which results in a high deformation. In this condition, some of the wear particles could fracture into several smaller particles depending on their material properties and some could undergo a permanent plastic deformation. In the current work, the fracture of the particles was ignored, and the plastic deformation and final platelet shape of the wear debris were investigated.

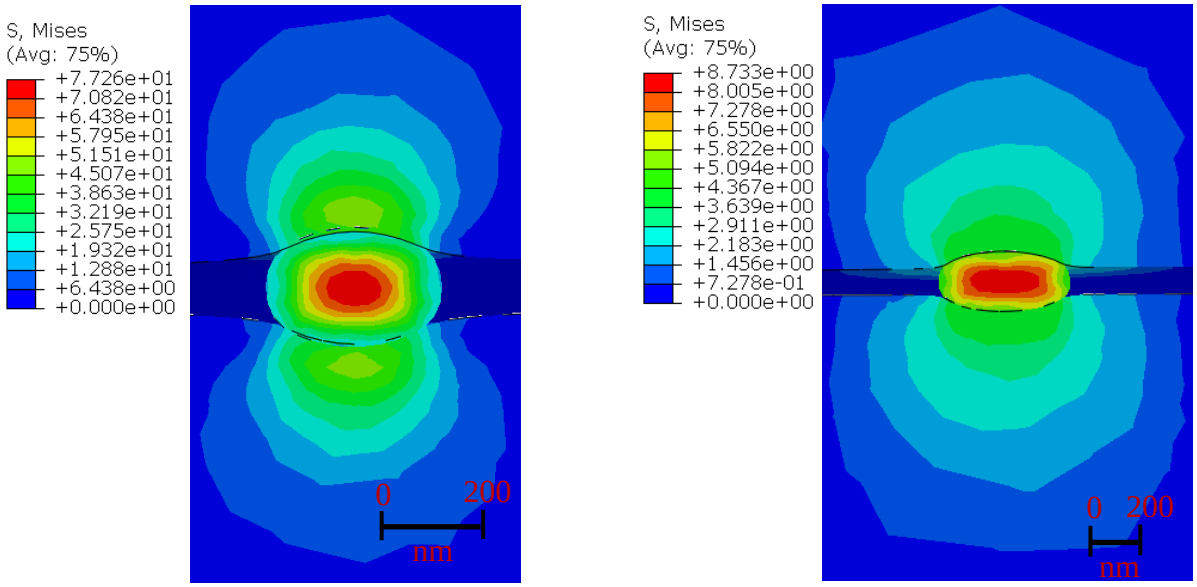

(a) **(b)**

Figure 4.14. (a) The wear particles shape and von Mises stress contours at the end of load balance step: a) Linear elastic, b) Elastic-plastic

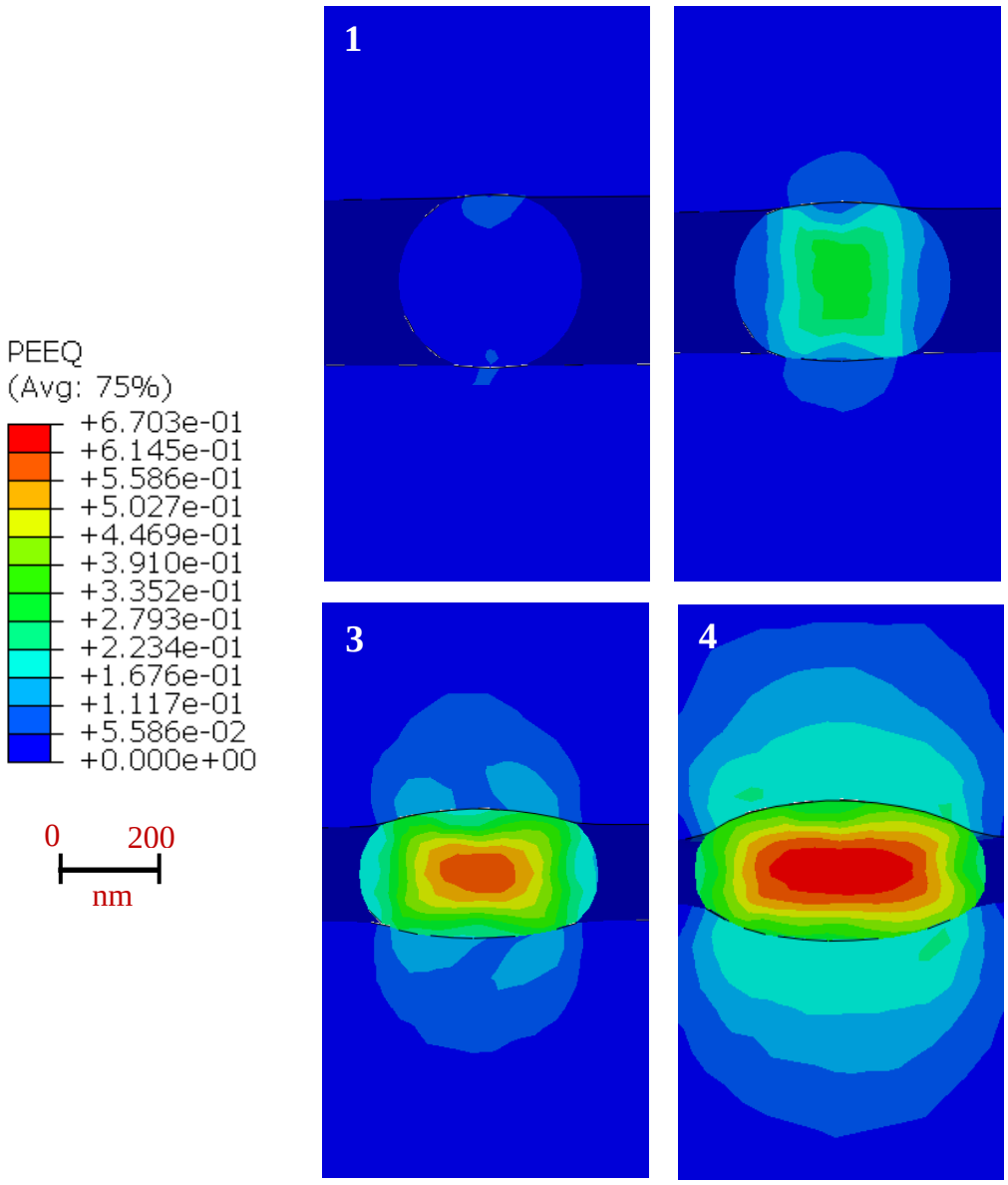

Figure 4.15. Equivalent plastic strain and evolution of the particle shape in the elastic-plastic model.

4.3.3 Effect of Third Body on Contact Pressure

The amount of the third body particles in the partial slip fretting wear depends on the geometry, load, displacement amplitude and material properties. Therefore, the number of wear debris is critical in the FE modeling. In the current study, several models with different number of wear particles including 2, 10, 18, and 36 particles were simulated (Figure 4.16). The challenge of adding more particles to the FE model is the number of elements which could be quite significant in terms of computational time. In all these models, the load and the boundary conditions were the same as the model without any particle and the particles were placed at the edge of the Hertzian contact. Very high contact pressure was observed at the location of third body particles due to the small size of the particles compared to the first bodies contact. In addition, while the first bodies contact remained in the elastic region, a high contact pressure occurred at the edge of the stick zone due to the stress concentration of the edge. As discussed before, by increasing the number of particles, the total load carried by the particles increased and the load was distributed on more particles, therefore, less load was carried by each particle individually and also by the first bodies. This reduction in local contact pressure could be significant when there is a lot of wear debris in the contact and consequently will affect the wear rate of the material.

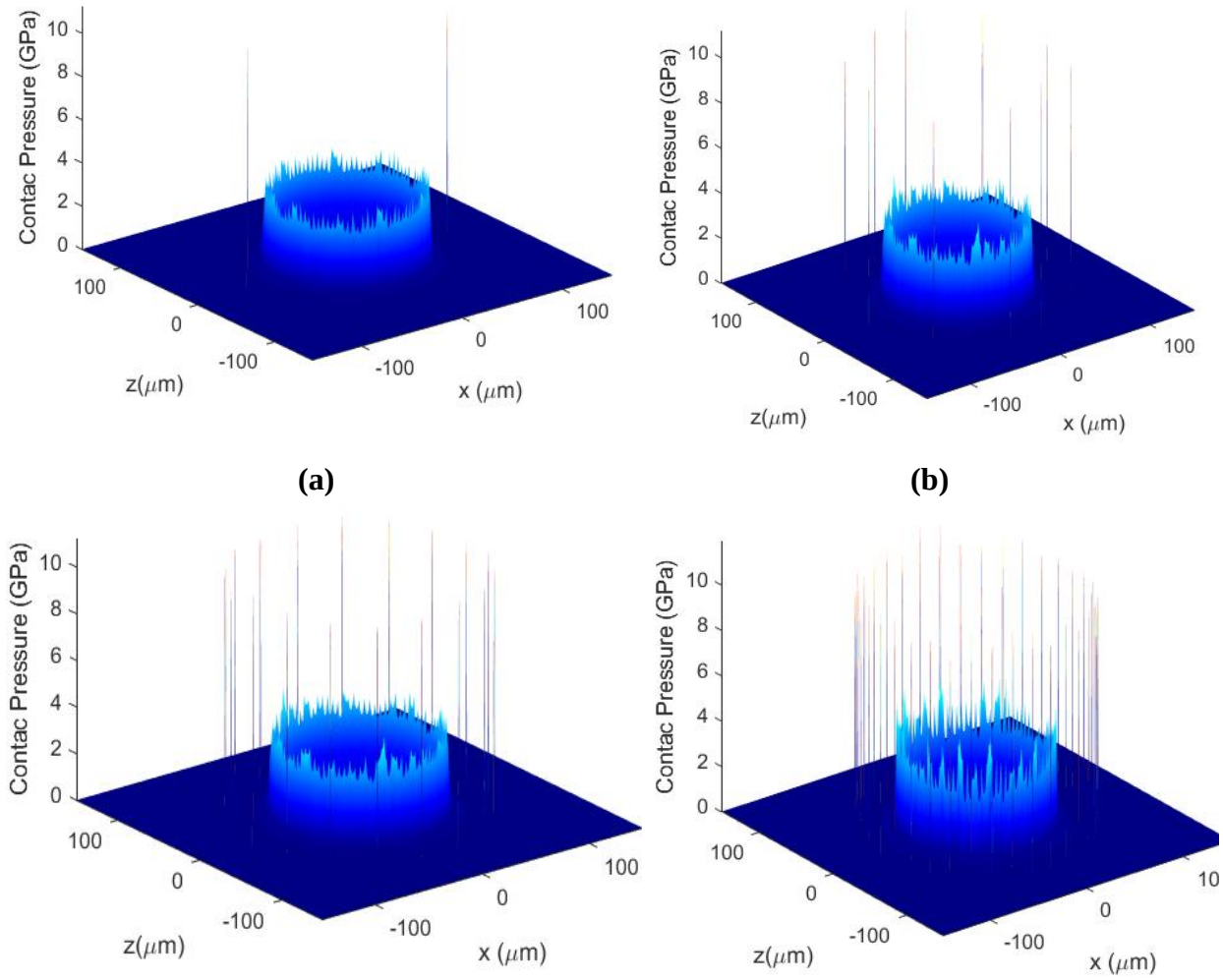

Figure 4.16. Contact pressure of the Hertzian point contact with different number of wear particles: a) 2, b) 10, c) 18, and d) 36 wear particles

4.3.4 Third Body Effect in a Fretting Contact

The fretting wear was modeled by applying sinusoidal displacement with the peak-to-peak amplitude of 1 μm to the upper body similar to the model without any third body. Because of this reciprocating motion, the contact experienced shear force in addition to the normal force. Both wear particles and the surfaces of the first bodies in the location of the third body particles faced a severe plastic deformation. Figure 4.17 illustrates the von-Mises and deformation of one of the wear particles and first bodies in the vicinity of the particle during the fretting cycle. To better understand the particle deformation, Figure 4.18 is also shown which is a cut view of one of the third body particles.

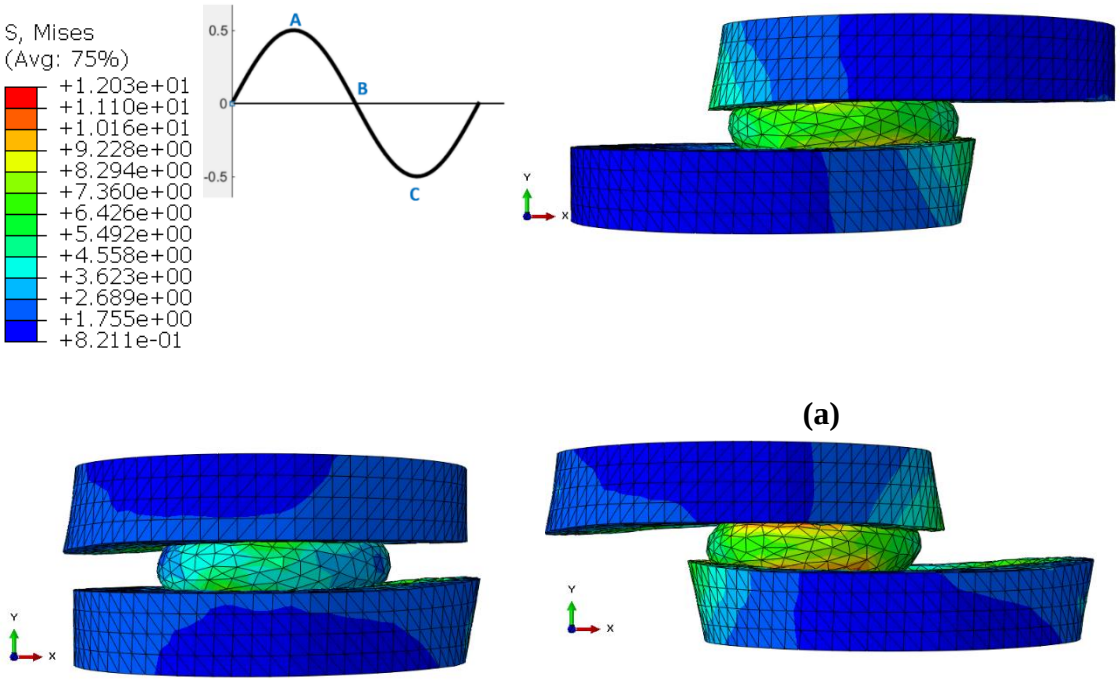

Figure 4.17. Evolution of a third body shape and surfaces in the small vicinity of the third body and the corresponding von-Mises stress during fretting cycle in a model with 18 particles: a) at point A of the cycle, b) at point B of the cycle, c) at point C of the cycle

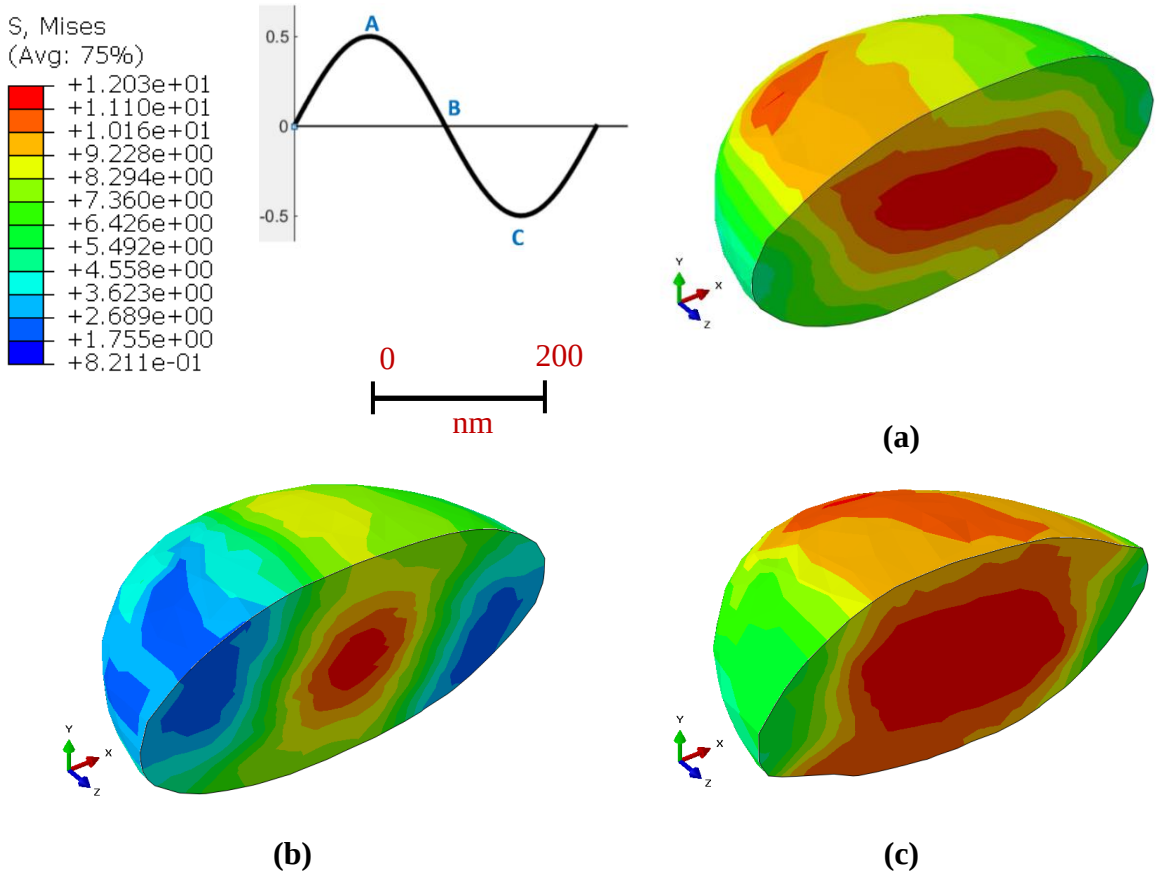

Figure 4.18. The cut view of the third body shape and the corresponding von-Mises stress during fretting cycle: a) at point A of the cycle in a model with 18 particles, b) at point B of the cycle, c) at point C of the cycle

Figure 4.19 depicts the fretting loop for one cycle obtained for the elastic-plastic model in a model with eighteen particles compared to a model without any third body particle. Both models showed a perfect partial slip fretting loop. The amount of shear force was lower in the model with wear particles as some portion of the shear force was captured by the particles and this result was obtained for the contact between first bodies. The hardening effect of the elastic-plastic model during the cycle is depicted in Figure 4.20 for a model in the presence of two third body particles. After the first fretting cycle, the plastic strain accumulated and the material strain hardened. This process continued toward the next cycles. Although the amount of hardening might not be significant in this model with two wear particles, but with more particles in contact and also increasing the number of cycles in the wear process, this effect will be noticeable. According to the literature [83], the strain hardening of the material continues and then stabilizes at some point

during the fretting process which results to have an elastic shakedown or plastic shakedown behavior based on the load, geometry, material properties, etc. [158].

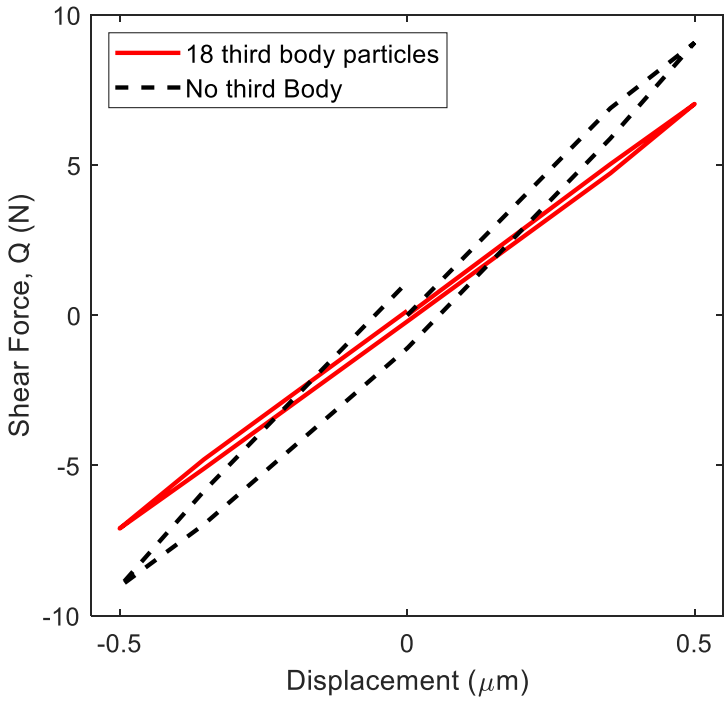

Figure 4.19. Fretting loops for an elastic plastic contact in presence of 18 third body particles compared to contact without any third body

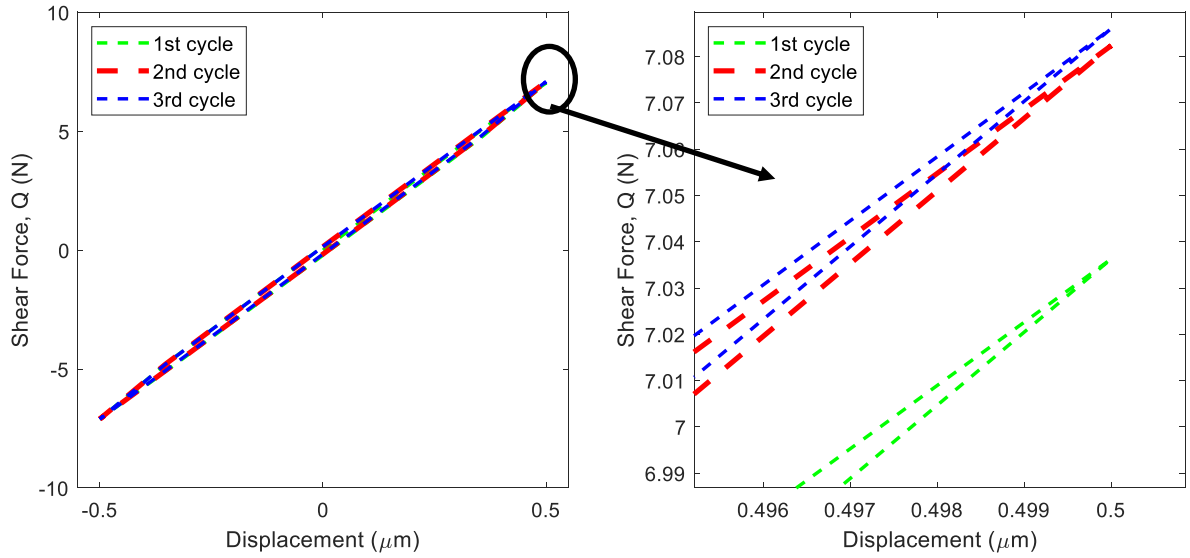

Figure 4.20. Hardening effect in fretting loop of the model with two third body particles

4.3.5 Local Partial Slip Behavior of the Third Body

In this investigation, the partial slip fretting wear model was studied in the presence of the third body. In order to achieve a partial slip zone in the FE model, the contact pressure of 1 GPa on a ball-on-flat configuration was used and then a sinusoidal reciprocating motion with the peak-to-peak displacement of 1 μm was applied to the ball. The corresponding stick-slip area at the time of maximum shear stress during the cycle as depicted in Figure 4.5 in the model without any wear particle. By adding the wear particles to the model, local stick-slip zones were also observed on the wear particles and the location of wear particles on the first bodies. Figure 4.21 demonstrated this local partial slip behavior on the third body particles at the point of maximum tangential load. Please note that while these wear particles were located in the slip zone of the first bodies, due to the high contact pressure and small displacement of the upper body, some portion of the particles in contact stuck to the first bodies. The partial slip regime causes crack generation in the contact of the bodies besides the material removal [159]. Therefore, these local partial slip zones on the first bodies could result in crack nucleation near these wear particles.

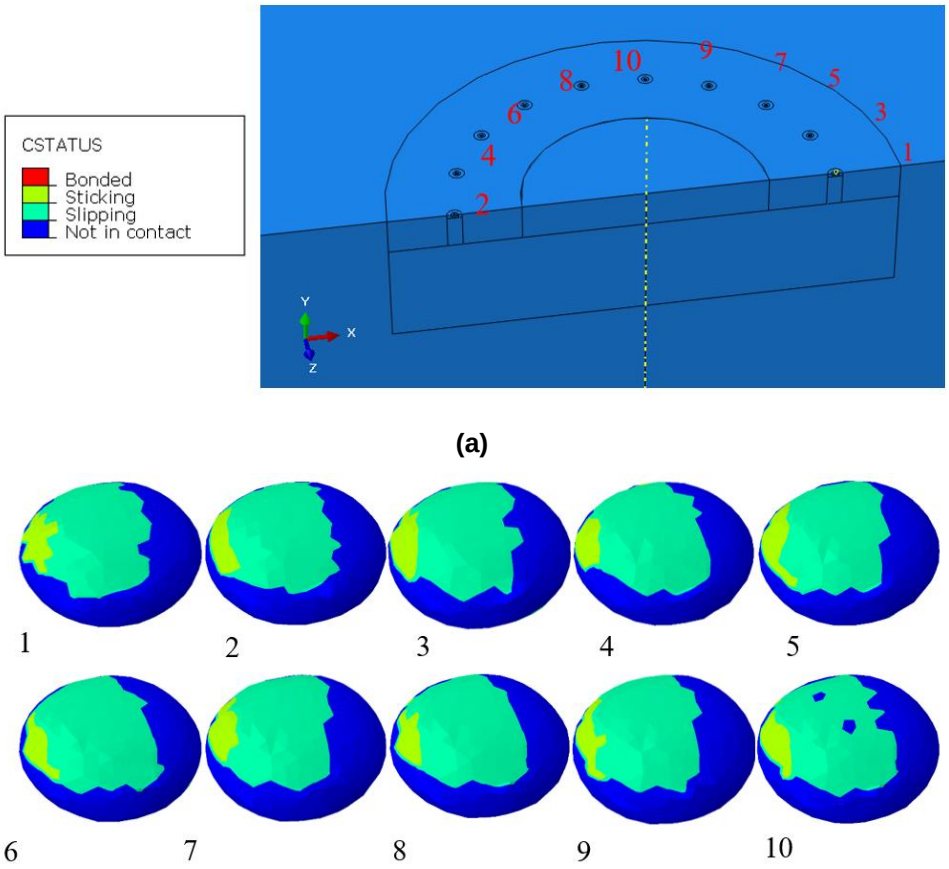

Figure 4.21. a) Zoom view of the half of the contact in lower body with 18 particles, b) Stick-slip zone on the wear debris measured at the point of maximum displacement

4.3.6 Third Body Particles with Different Material Properties

In the current modeling, it was assumed that the material constitutive relationships for the first bodies and the third body is the same while in reality, the third body could be different in microstructure and composition due to the fracturing, agglomerating, oxidizing, etc. Godet et al. [64] and Jiang et al. [160] studied the properties of wear particles. They realized that the third body particles are oxidized immediately after detaching from the first bodies. Everitt et al. [161] performed a nano-indentation test on the wear particles of Ti-6Al-4v and realized that the third body had higher hardness than the first bodies and the modulus of elasticity was marginally different from the first bodies.

In this investigation, the effect of different material properties including the modulus of elasticity (E), hardening modulus (M) and yield strength (Sy) on the contact stress and slip properties of the bodies were studied. First, it was assumed that both the third body and the first bodies have the same properties. Figure 4.22 depicts the effect of E on the contact pressure of a model in the presence of two wear particles. Three different models with the properties of Sy=2.03 GPa, M=10 GPa, and E=100, 200, and 300 GPa were simulated. It is demonstrated that at the location of first bodies where most of the load were carried, the model with E=100 GPa had the lowest contact pressure while at the location of the third body particles, it had the highest contact pressure. In fact, the contact of first bodies was mostly in the elastic regime and by decreasing E, the contact pressure decreased too. For the same load, to achieve the force balance, higher deformation occurred in the material with lower E which resulted to undergo significant deformation and consequently higher contact pressure at the location of the third body particles.

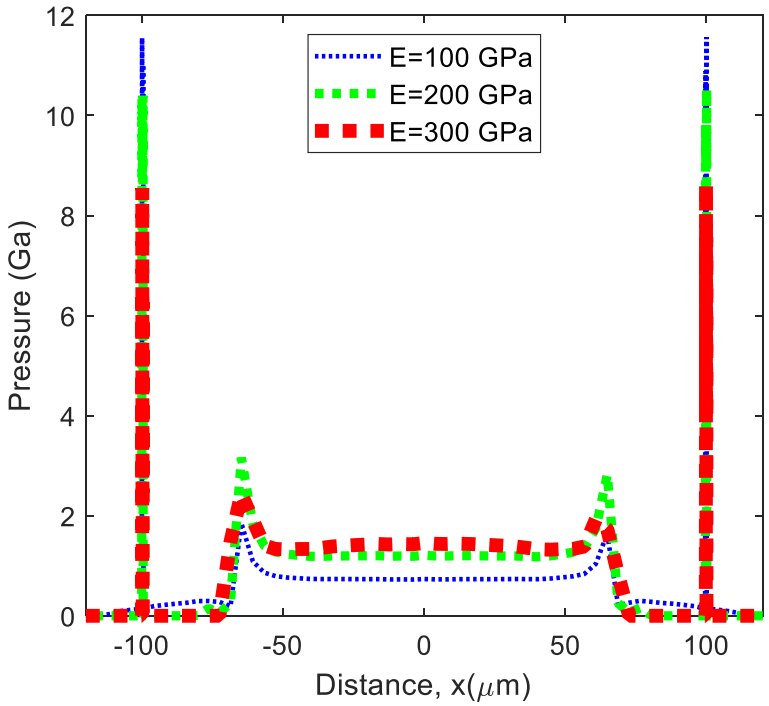

Figure 4.22. Comparison of centerline contact pressure for the cases with same M and Sy and different E for an elastic-plastic model with two particles

Figure 4.23 illustrates the effects of M on the contact pressure. Three different models with the properties of Sy=2.03 GPa, E=200 GPa, and M=10, 20, and 30 GPa were considered. It is demonstrated that the contact pressure of the first bodies was almost the same for these three cases as it was mostly in the elastic region while the contact pressure in the location of the wear particles changed considerably. The material with the higher hardening modulus had a higher contact pressure and this would affect the fretting process as well.

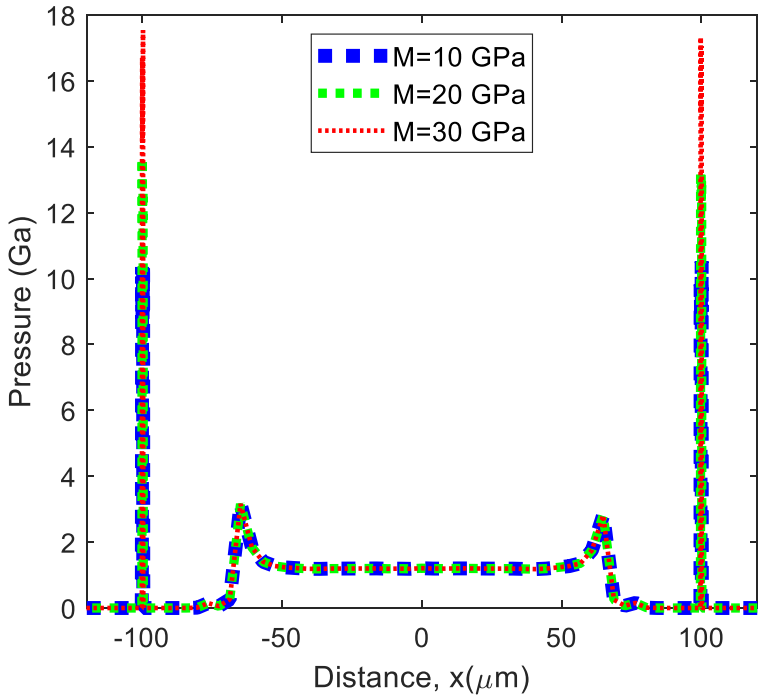

Figure 4.23. Comparison of centerline contact pressure for the cases with same E and Sy and different M for an elastic-plastic model with two particles

Figure 4.24 depicts the effect of Sy on the contact pressure. Three different models with the properties of E=200 GPa, M=10 GPa, and Sy=2.03, 3.03, and 4.03 GPa were simulated. It is shown that the trend of increase in Sy is similar to M. The model with a higher value of yield strength had a higher contact pressure in the location of third body particles while for the first bodies contact region, minimal change was observed as it was mostly in elastic. Actually, in the model with higher yield strength, the plasticity was delayed which resulted in higher contact pressure.

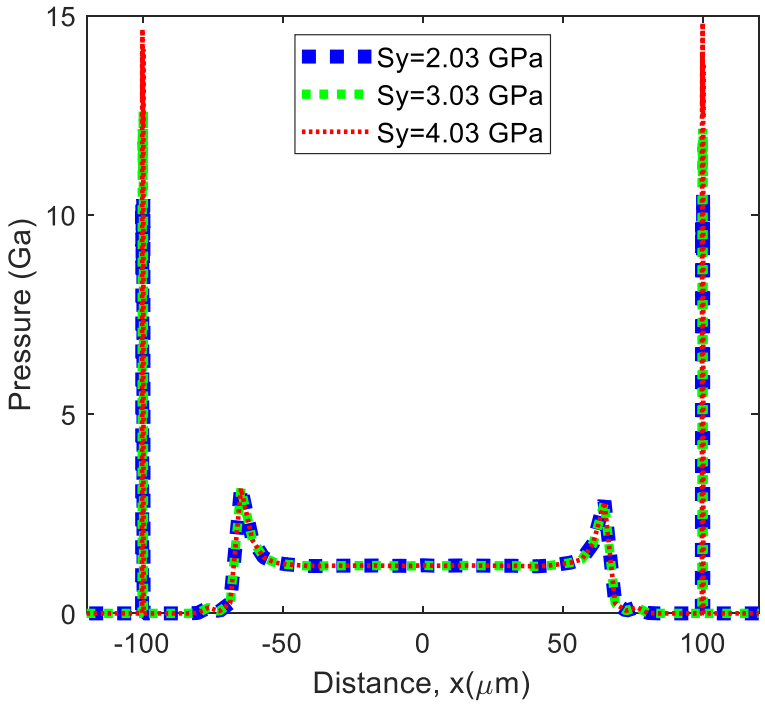

Figure 4.24. Comparison of centerline contact pressure for the cases with same E and M and different Sy for an elastic-plastic model with two particles

As described earlier, due to the oxidization of the third body, the material properties of the wear particles usually differ from the first bodies. To evaluate this behavior, another model with different material properties for the third body particles than the first bodies were considered. As shown in Table 4.2, it was assumed that wear particles had E= 300 GPa, Sy=2.53 GPa, and M=15 GPa while the first bodies had the previously used material properties (E= 200 GPa, Sy=2.03 GPa, and M=10 GPa). As depicted in Figure 4.25a, harder wear particles resulted in higher contact pressure on first bodies in the location of particles which would consequently affect the wear rate in fretting. In addition, the average of the accumulated slip of the first body elements in the location of the third body is demonstrated in Figure 4.25b. It is shown that less slip occurred when the wear particles were harder which means a higher portion of the contact was in the stick zone during the fretting process. The negative magnitude of slip (CSLIP1 in Abaqus) indicates that the node has moved in the negative first slip direction.

Table 4.2. Material properties of first bodies and the third body

Properties	First bodies	Third body
Modulus of elasticity, E (GPa)	200	300
Poisson ratio, ν	0.3	0.3
Hardening modulus, M (GPa)	10	15
Yield strength, S_y (GPa)	2.03	2.53

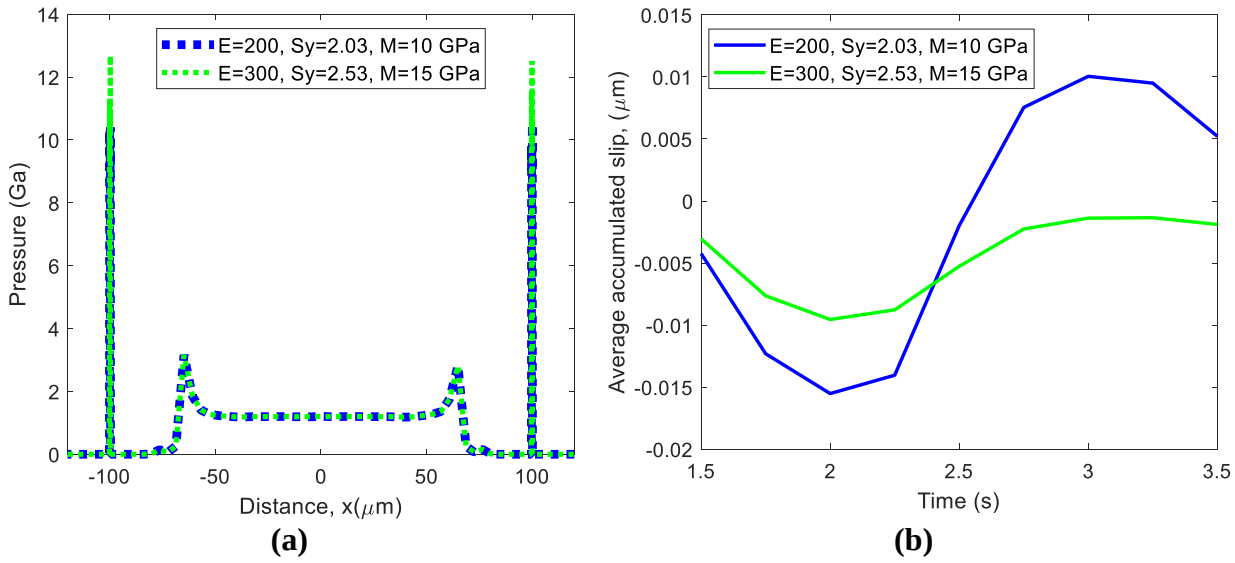

Figure 4.25. Comparison of a) contact pressures and b) average slip when the third body particles have different material properties than first bodies

4.4 Conclusions

The objective of this investigation was to develop a 3D FE model to study the effect of third body particles on a partial slip fretting wear in Hertzian point contacts. The effect of third body particles in an initial stage of a fretting process on different contact parameters such as contact pressure, shear stress, hardening properties, and slip behavior was studied. Plastic material properties were included in the model as there was a very high contact pressure at the location of the wear debris. A fundamental investigation was carried out to understand the effect of plasticity on contact pressure, force-deformation, and contact slip. Because of high plastic deformation on the particles, a platelet structure was observed for the wear particles which was similar to the experimental observations. Also, it was depicted that by increasing the number of particles in contact, more load was carried by the wear particles which affect the wear rate of the material.

Fretting loops of the model in different cycles were compared and the relation between the number of cycles and the hardening process was evaluated. While the wear particles were placed in the slip zone of the contact, local stick-slip behavior was observed at the location of particles that could be an indication of crack nucleation on the first bodies. In addition, several cases were considered to model wear debris with different material properties than first bodies due to oxidation and plastic deformation. The results indicate that harder wear particles had a higher contact pressure and lower slip at the location of particles which affect the wear rate of the bodies.

5. A 3D FINITE ELEMENT DAMAGE MECHANICS MODEL TO SIMULATE FRETTING WEAR OF HERTZIAN LINE AND CIRCULAR CONTACTS IN PARTIAL SLIP REGIME

5.1 Introduction

In this work, a 3D fretting wear model was developed based on the damage mechanics approach and accumulated dissipated energy to investigate fretting wear of Hertzian circular and line contacts. The damage mechanics stress-based law was implemented using the commercially available ABAQUS finite element software. Voronoi tessellation was used to simulate the microstructure of the material. Fretting wear process was simulated such that the elements with the maximum stress were removed in each fretting cycle. In order to reduce the computational expenses, the partial slip regimes were modeled using the normal and shear surface tractions for the circular and line contacts applied to the wear body. The stress distribution and wear volume rate calculated from FE model were compared with the wear coefficient available in the open literature. The influence of modulus of elasticity, hardness, and COF on fretting process were evaluated. Then, the FE model was verified using several fretting wear tests for two different materials (AISI 8620 and AISI 1566). The experiments were performed for the circular contact configuration. The modulus of elasticity and hardness of each material were obtained using nanoindentation tests near the contact surface and the grain size were measured using the scanning electron microscope (SEM). These properties were implemented in the FE model and the worn surface and wear rate were compared with the experimental results.

5.2 Modeling Approach

In the following sections, the formulation of damage law based on accumulated dissipated energy approach and simulation of fretting wear in circular and line contacts using FE modeling are described.

5.2.1 Formulation of Wear Equation

Fretting wear can be evaluated by different methods such as Archard and dissipated energy equations. The dissipated energy method was first studied by Matveskey [162] who related the

frictional dissipated energy in an oil-lubricated contact problem to wear. Fouvry et al. [123] proposed a relation between fretting wear and the dissipated energy in bodies in contact. They recommended that wear volume can be obtained based on the accumulated dissipated friction energy method. In this approach, wear volume (Vw) is proportionally related to the total dissipated friction energy (Ed):

$$V_w \, \alpha \, E_d \tag{5.1}$$

where E_d can be written as

$$E_d = \mu F_N S \tag{5.2}$$

where μ is the COF, F_N is normal load, and S is sliding distance in one fretting loop.

Gosh et al. [37] indicated that the fraction of energy which is essential to wear a material can be associated with the inverse of modulus of elasticity (E). Therefore, the wear volume can be expressed as:

$$V_w = \frac{c}{E} E_d = \frac{c}{E} \mu F_N S \tag{5.3}$$

where c is a constant dependent on the surface properties in contact including lubrication and material compatibility which can be obtained experimentally. In this study, c is considered to be 1 for the dry contact of compatible surfaces.

Also, Ghosh et al. [37] approximated the COF based on the properties of the softer material in contact as follows:

$$\mu \approx \frac{0.8 S_{ut}}{H} \tag{5.4}$$

where S_{ut} is the ultimate tensile strength of the material and H is the hardness of the softer material. Finally, the fraction of energy that results in wear of the material can be approximated as follow:

$$V_w \approx \frac{0.8 S_{ut} F_N S}{HE} \tag{5.5}$$

5.2.2 Damage Model Wear Law

Damage is the process of material deterioration which manifests itself as a gradual degradation of the material through the initiation and propagation of microcracks. A thermodynamic state variable D is defined in CDM to consider the microscopic failure mechanism. In an elastic material, the constitutive relationship coupled with isotropic damage has the following form:

$$\sigma_{ij} = C_{ijkl}(I - D)\, \varepsilon_{kl} \tag{5.6}$$

where σ_{ij}, C_{ijkl}, and ε_{kl} correspond to the stress, stiffness, and strain tensors, respectively. D is damage variable, which ranges from 0 (undamaged) to 1 (fully damaged).

The elastic damage evolution law at a material point can be expressed as follows [137,142]:

$$\frac{dD}{dN} = \alpha \left[\frac{\Delta\sigma}{\sigma_r(1-D)}\right]^m \tag{5.7}$$

where N is the number of cycles, m and σ_r are material parameters, α is a constant related to the material properties, and $\Delta\sigma$ is the critical stress range. Integrating Equation 5.7 from 0 to N and D from 0 to 1, N can be calculated as follows:

$$\int_0^N dN = \frac{1}{\alpha}\int_0^1 \left[\frac{\Delta\sigma}{\sigma_r(1-D)}\right]^{-m} dD \tag{5.8}$$

$$N = \frac{1}{\alpha}\frac{1}{m+1}\left[\frac{\sigma_r}{\Delta\sigma}\right]^m \tag{5.9}$$

$\Delta\sigma$ can be considered as shear or normal stress according to the type of loading which is applied to the bodies in contact. Raje et al. [33] showed that in RCF, shear stress is the critical component for crack initiation and propagation. Weinzapfel and Sadeghi [144] demonstrated that shear stress experiences a reversals in a Hertzian contact which makes it critical in RCF. Therefore, in this study, it is assumed that change in the shear stress initiates the failure in wear phenomenon [37] and thus in the damage model $\Delta\sigma = \Delta\tau$.

Rewriting the wear volume equation as V_w=Ah_w where A is the worn area and h_w is the worn depth and considering the sliding distance as S=4δN where δ is displacement amplitude; Equation 5.5 can be rearranged as:

$$Ah_w = \frac{0.8S_{ut}F_N(4\delta N)}{HE} \quad 5.10$$

$$N = \frac{h_w}{4\delta}\frac{E}{0.8S_{ut}}\frac{H}{\sigma} \quad 5.11$$

By comparing Equations 5.9 and 11, replacing σ by τ and considering $\frac{0.8S_{ut}4\delta}{h_w}$ to be a constant (β), the values of m and σ_r in Equation 5.7 are as follows:

$$m = 1 \quad , \quad \sigma_r = H \quad , \quad \alpha = \frac{\beta}{E} \quad 5.12$$

Therefore, the elastic damage evolution law can be simplified as:

$$\frac{dD}{dN} = \frac{\beta}{E}\frac{\Delta\tau}{H(1-D)} \quad 5.13$$

The constant value of β (GPa) can be adjusted based on the experimental wear result

5.2.3 Damage Model Wear Law

In the current investigation, a 3D elastic FE model based on CDM was developed to predict the fretting wear behavior of a Hertzian circular and line contacts in the partial slip condition. In order to have a tenable computational effort, only half of the contact was modeled for the circular contact domain and the periodic boundary condition (PBC) was applied to both models. The domain was divided into two regions as shown in Figure 5.1. The first region is the representative volume element (RVE) which is the critically stressed area. The majority of this region was meshed using Voronoi tessellation which simulate the morphology of the material microstructure. Voronoi tessellation has been widely used for representing material grain microstructures [139,141,163–166]. In this approach, a set of randomly seed points were generated to create the Voronoi cells. All the points on each cell are close to the seed point of that cell than any other points in the space. In this model, the average grain size of 4 μm was chosen. The remaining part of the semi-infinite domain was meshed using linear strain tetrahedron (LST) with a courser mesh than Voronoi to decrease the number of elements and thus the computational effort. The region beyond the RVE was meshed using constant strain tetrahedron (CST) with the courser mesh. The constraint between the CST and LST elements was considered to stablish continuity in solution.

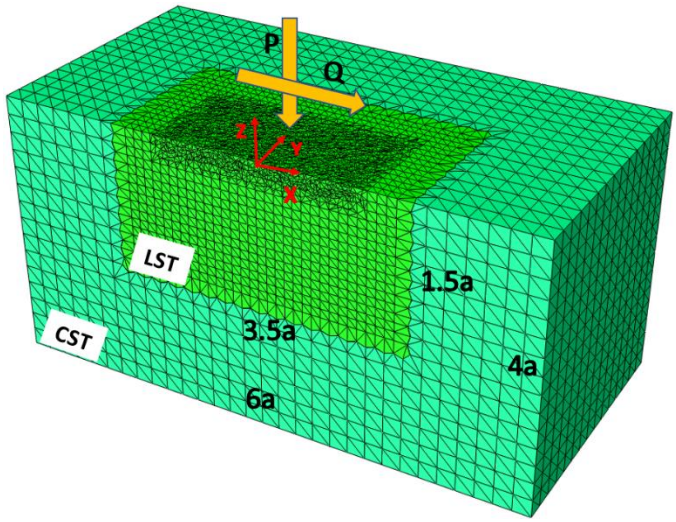

(a)

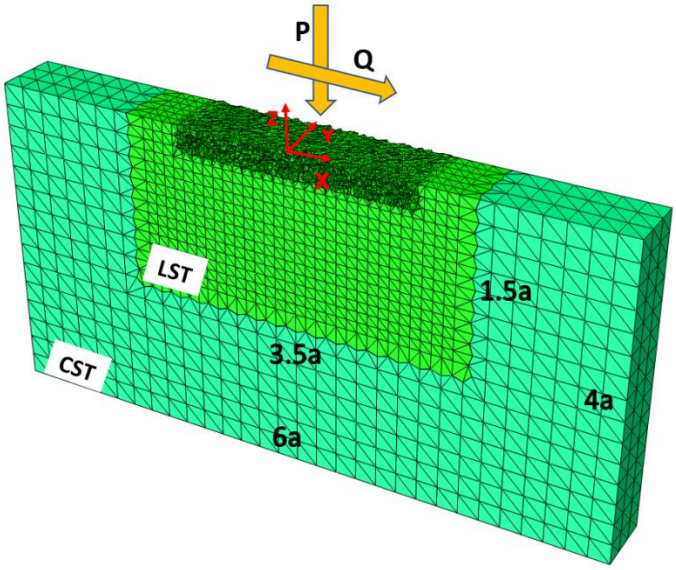

(b)

Figure 5.1. 3D FE model for fretting wear analysis: (a) circular contact domain, (b) line contact domain

In partial slip regime, normal and shear surface tractions for the circular and line contacts with the maximum Hertzian pressure of 1 GPa and Hertzian half contact of a = 100 μm were applied to the top surface of the domain with the fretting displacement amplitude of $\delta = 0.7$ μm. According to Hills and Nowell [167,168] for the cyclic variation of tangential force in partial slip fretting wear of similar material, the normal and shear tractions acting on x-direction during the reversal of the load for a circular contact is as follows:

$$P(r) = -P_{max}\sqrt{1-\left(\frac{r}{a}\right)^2} \tag{5.14}$$

$$Q(r) = \begin{cases} -\mu P_{max}\sqrt{1-({}^{r}/_{a})^2} & c' < |r| \le a \\ -\mu P_{max}\left(\sqrt{1-({}^{r}/_{a})^2} - 2\,{}^{c'}/_{a}\sqrt{1-\left({}^{r}/_{c'}\right)^2}\right) & c < |r| \le c' \\ -\mu P_{max}\left(\sqrt{1-({}^{r}/_{a})^2} - 2\,{}^{c'}/_{a}\sqrt{1-\left({}^{r}/_{c'}\right)^2} + {}^{c}/_{a}\sqrt{1-({}^{r}/_{c})^2}\right) & |r| \le c \end{cases} \tag{5.15}$$

where P_{max} is the peak contact pressure, c is the stick zone size and c' is the instantaneous size of stick zone in non-monotonic loading and can be calculated as follows:

$$c = a\sqrt[3]{1-\frac{T_{max}}{\mu F_{max}}} \tag{5.16}$$

$$c' = a\sqrt[3]{1-\frac{T_{max}}{2\mu F_{max}}(1-\sin(2\pi t_{step}))} \tag{5.17}$$

where F_{max} is the maximum normal force, T_{max} is the maximum tangential force ($T_{max} < \mu F_{max}$ in the partial slip regime), t_{step} is between 0 to 1 and represents one cyclic loop in the fretting wear modeling.

For the line contact model, r is substituted by x in Equations 5.14 and 5.15 (the direction of the fretting motion) and c and c' can be obtained as follows:

$$c = a\sqrt{1-\frac{T_{max}}{\mu F_{max}}} \tag{5.18}$$

$$c' = a\sqrt{1-\frac{T_{max}}{2\mu F_{max}}(1-\sin(2\pi t_{step}))} \tag{5.19}$$

These normal and shear tractions in the partial regime were implemented in ABAQUS subroutine ULTRACLOAD. This allowed to model fretting in partial slop without using the upper body which significantly improved the computational effort. The initial values of c and c' were calculated using a model with two bodies in contact for both circular and line contact models and

then implemented in the current modeling approach. Table 5.1 contains the material parameters used in this investigation. Table 5.2 contains the remaining boundary conditions for the 3D model.

Table 5.1. Material damage parameters for the fretting wear modeling

Material properties	**Value**
Undamaged elastic modulus, E (GPa)	210
Poisson's ratio, υ	0.3
Coefficient of friction, μ	0.6
Hardness, H (GPa)	2
Material parameter in damage, m	1
Hertzian point contact half-width, a (μm)	100
Maximum Hertzian contact pressure, P_{max} (GPa)	1.0

Table 5.2. Boundary conditions of the model

	Extent					
Model	**-X**	**+X**	**-Y**	**+Y**	**-Z**	**+Z**
Circular contact	Periodic	Periodic	Symmetric	Fixed	Fixed	Normal and shear tractions
Line contact	Periodic	Periodic	Periodic	Periodic	Fixed	Normal and shear tractions

To simulate the damage, Equation 5.13 was used for all the elements in the RVE such that the stress range $\Delta\tau$ was calculated for each tetrahedron element. The jump-in-cycle procedure [138,140,143,169] was implemented in the model to expedite computational fretting process. This method assumes the stress-strain response and the material damage status are constant over a block of cycles [142,144,148]. This damage field was implemented in the ABAQUS subroutine USDFLD. Finally, to calculate the wear rate, the volume of the removed elements in the model was calculated at different cycles using a MATLAB post processing code.

5.3 Results and Discussion

5.3.1 Normal and shear tractions and internal stresses

In order to verify the normal and shear tractions in the circular and line contact models, the centerline (at y = z = 0) normal and shear stresses from ABAQUS were compared with the

analytical solutions as shown in Figure 5.2 and Figure 5.3 respectively. The resultant stress fields for the circular and line contacts in the partial slip regime were nearly identical with the analytical solutions. It is worth noting that the simulation time for the current model without upper body was about 10% of the running time for the same model considering two bodies in contact. In addition, the current model didn't face convergence problems that was a major issue in the model with two bodies in contact especially after the elements were removed due to wear.

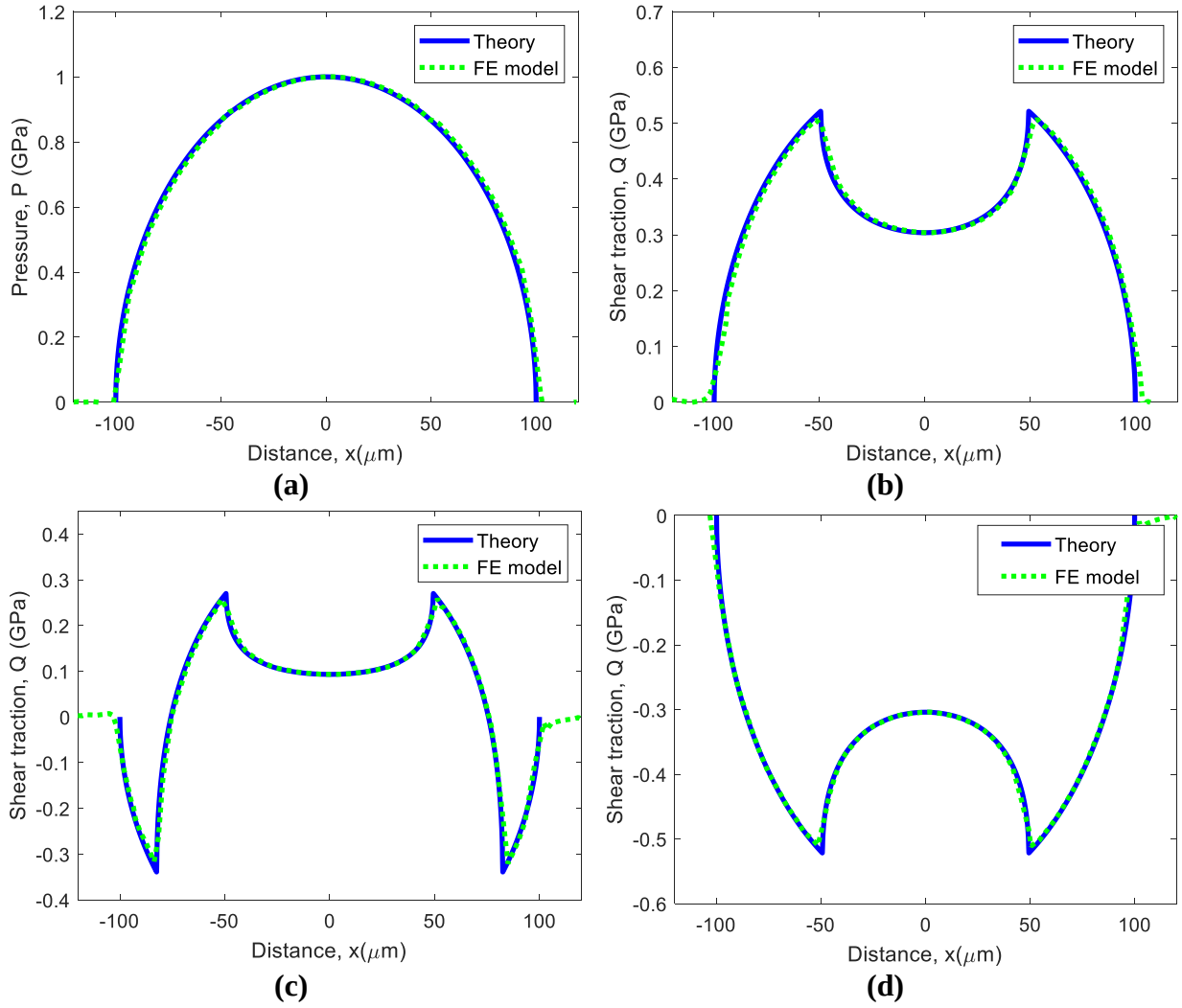

Figure 5.2. Comparison of centerline normal and shear tractions from the FE model with theory in partial slip regime of circular contact: a) normal traction at t_{step}=0.25, b) shear traction at t_{step}=0.25, c) shear traction at t_{step}=0.5, d) shear traction at t_{step}=0.75

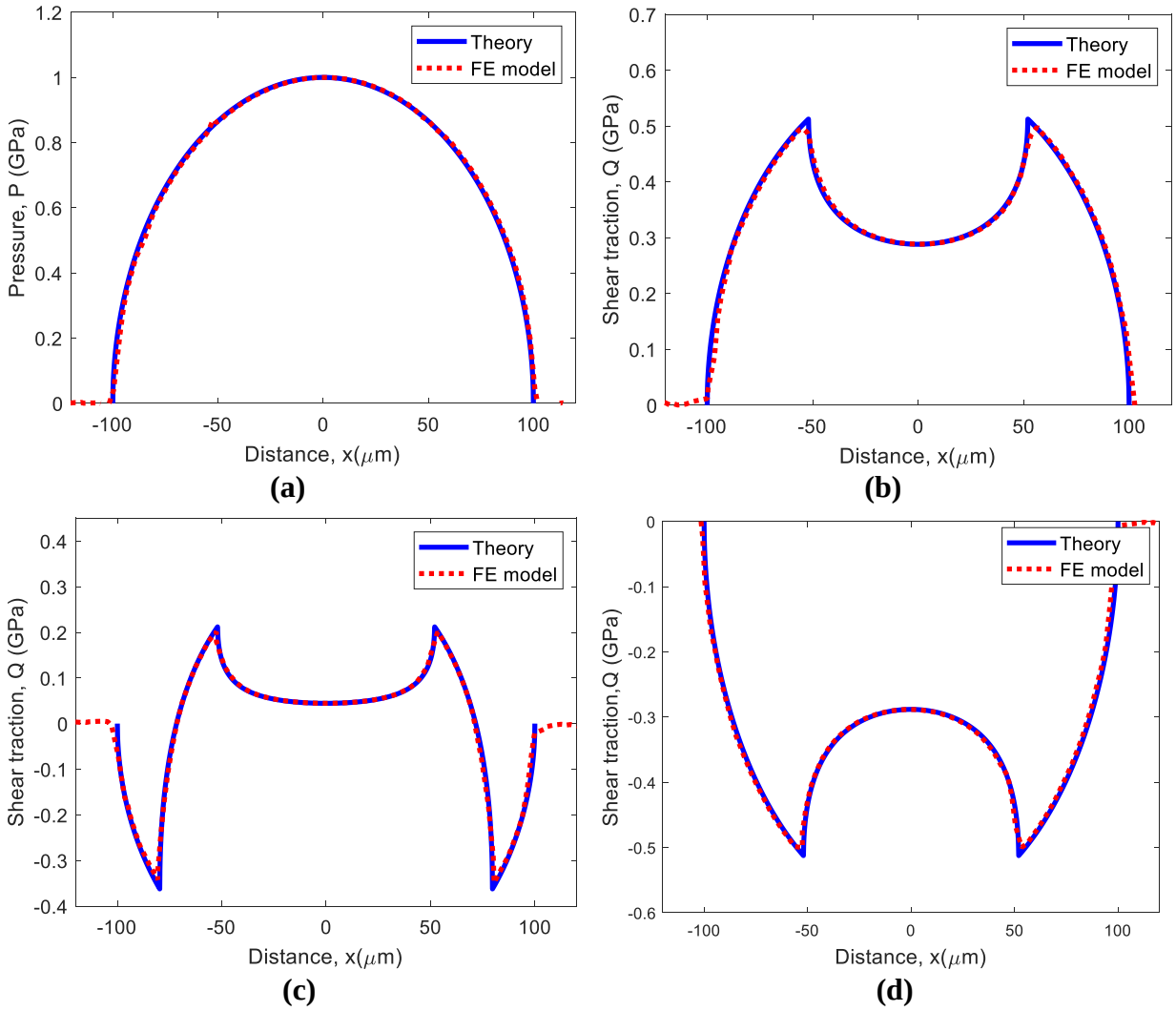

Figure 5.3. Comparison of centerline normal and shear tractions from the FE model with theory in partial slip regime of line contact: a) normal traction at t_{step}=0.25, b) shear traction at t_{step}=0.25, c) shear traction at t_{step}=0.5, d) shear traction at t_{step}=0.75

The internal stresses (at x=y=0) for both circular and line contact models were compared with theory as illustrated in Figure 5.4. This verified the accuracy of the boundary conditions, mesh quality, and domain size.

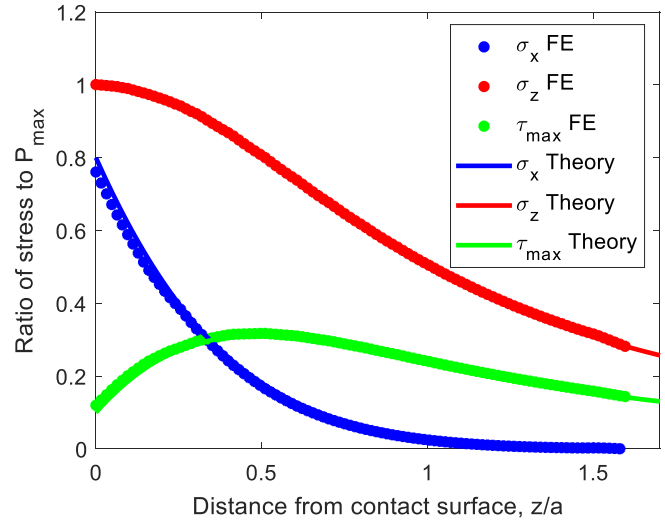

(a)

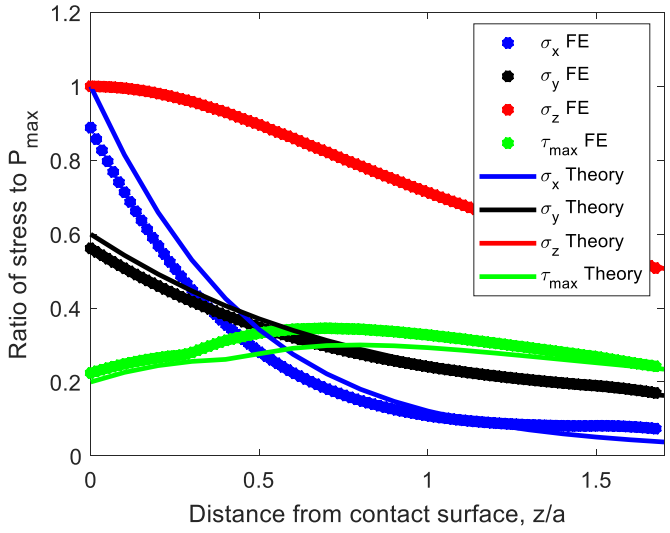

(b)

Figure 5.4. comparisons of the internal stresses along the centerline at x = 0: (a) circular contact, (b) line contact

Figure 5.5 also depicts the von-Mises stress for the partial regime of circular and line contact models at the end of the stoke. As expected, the results demonstrate that the von-Mises stress is higher in slip region than in stick region of the partial slip regime. Also, the stress was critical on the top surface of the models.

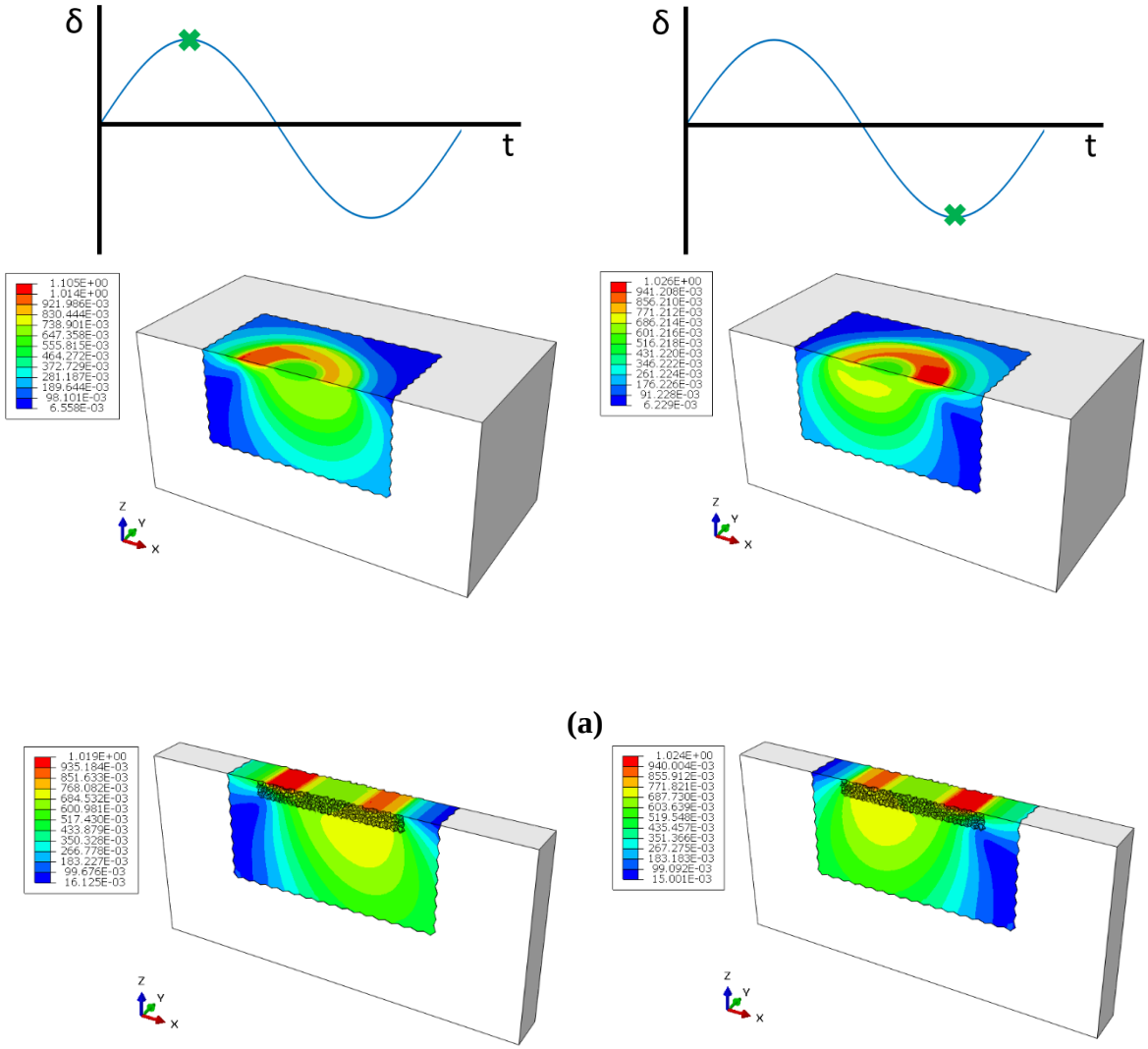

Figure 5.5. von-Mises profiles of the partial slip fretting wear loops obtained by the FE model: a) circular contact, b) line contact

5.3.2 Material Removal, Wear Scars, and Contact Pressure

There are two main regimes in the fretting wear phenomenon: partial slip and gross slip. In the partial slip regime phenomenon, the center of the contact is in stick and the outer edges of the contact are in slip, therefore in the slip zones due to high shear stress, the contact wears and the center of the contact remains unworn. As indicated previously, the wear law used in this

modeling approach is based on the shear stress and the contact shear stress is significantly lower in the stick zone as compared to the slip zone. In this FEM, as wear progressed, high contact pressure was observed at the outer edge of the stick zone which resulted in higher contact shear stress and the material was removed from this area. As the number of cycles increased, the worn area propagated toward the center of the contact and the size of the stick zone reduced and eventually, the entire stick region was worn off. Figure 5.6 and Figure 5.8 depict the wear scars at different cycles for the circular and line contact models, respectively. The corresponding normal and shear tractions on the surface of these worn models are also demonstrated in Figure 5.7 and Figure 5.9 for the circular and line contacts, respectively.

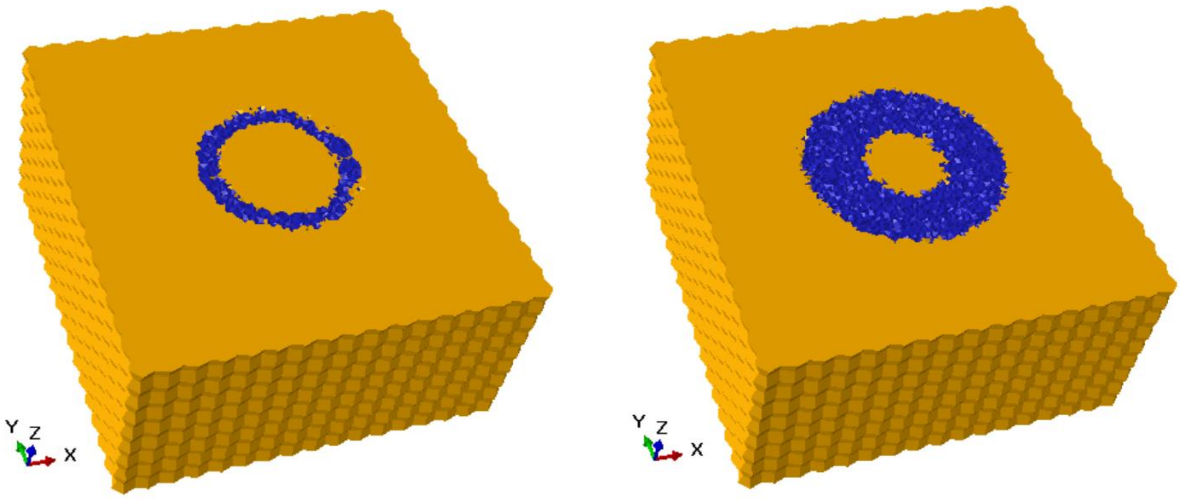

(a) **(b)**

Figure 5.6. Propagation of the wear scar for the partial slip regime of the circular contact: (a) N=250 cycles, (b) N=1000 cycles

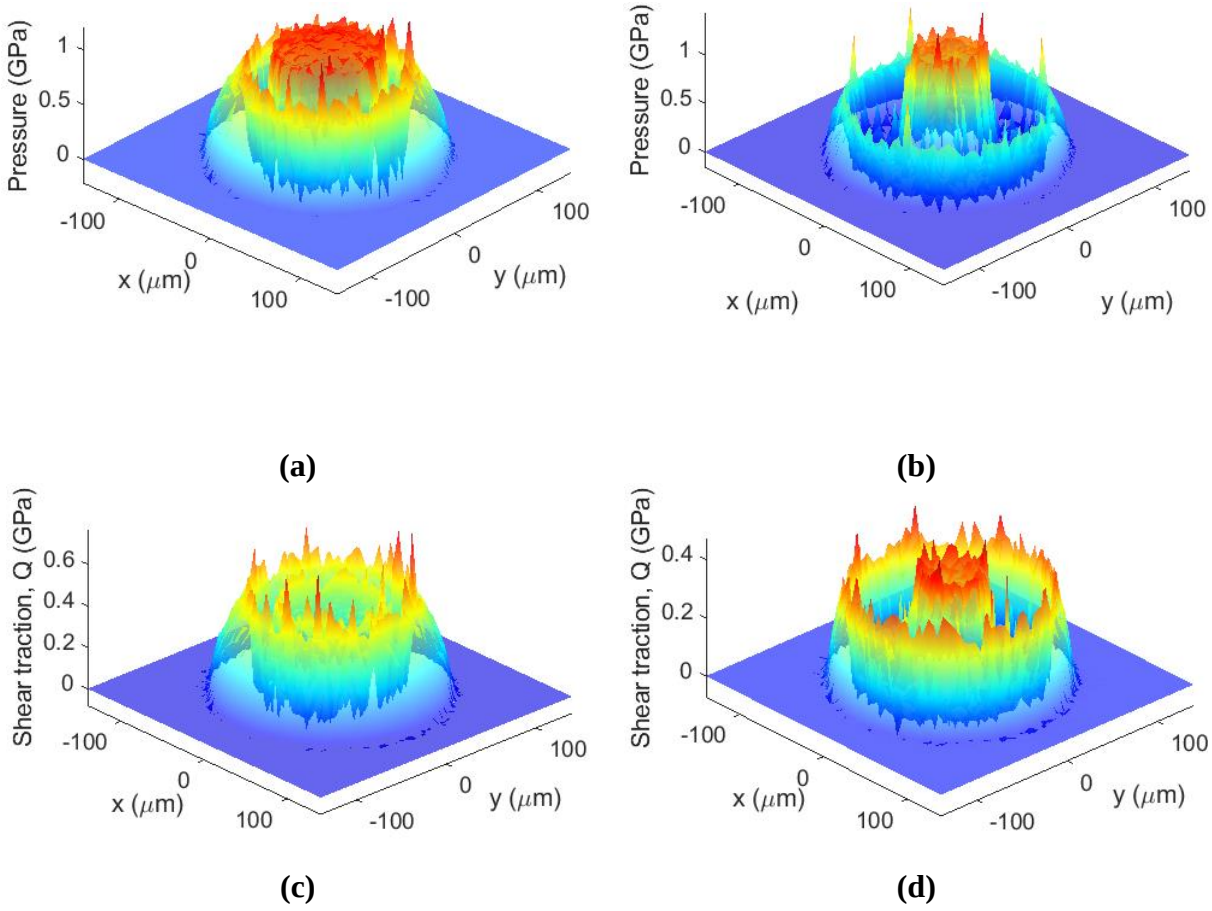

Figure 5.7. 3D normal and shear tractions of the worn surface for the circular contact at t_{step}=0.25: (a) normal stress at N=250 cycles, (b) normal stress at N=1000 cycles, (c) shear stress at N=250 cycles, (d) shear stress at N=1000 cycles

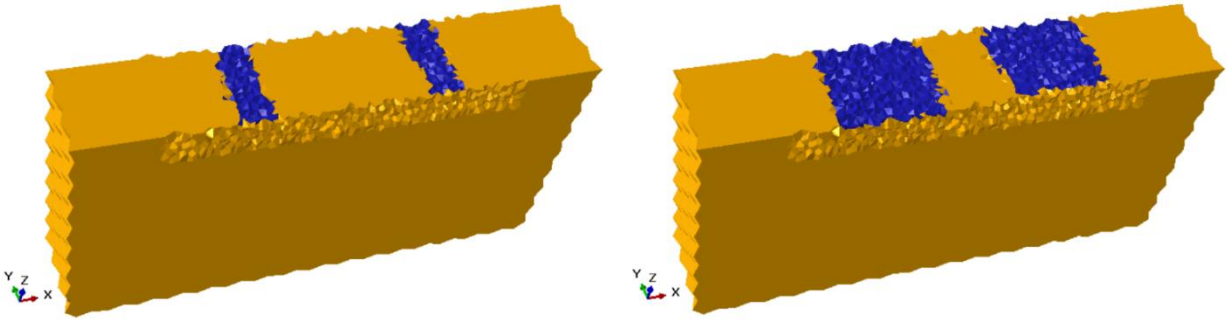

(a) **(b)**

Figure 5.8. Propagation of the wear scar for the partial slip regime of the line contact: (a) N=250 cycles, (b) N=1000 cycles

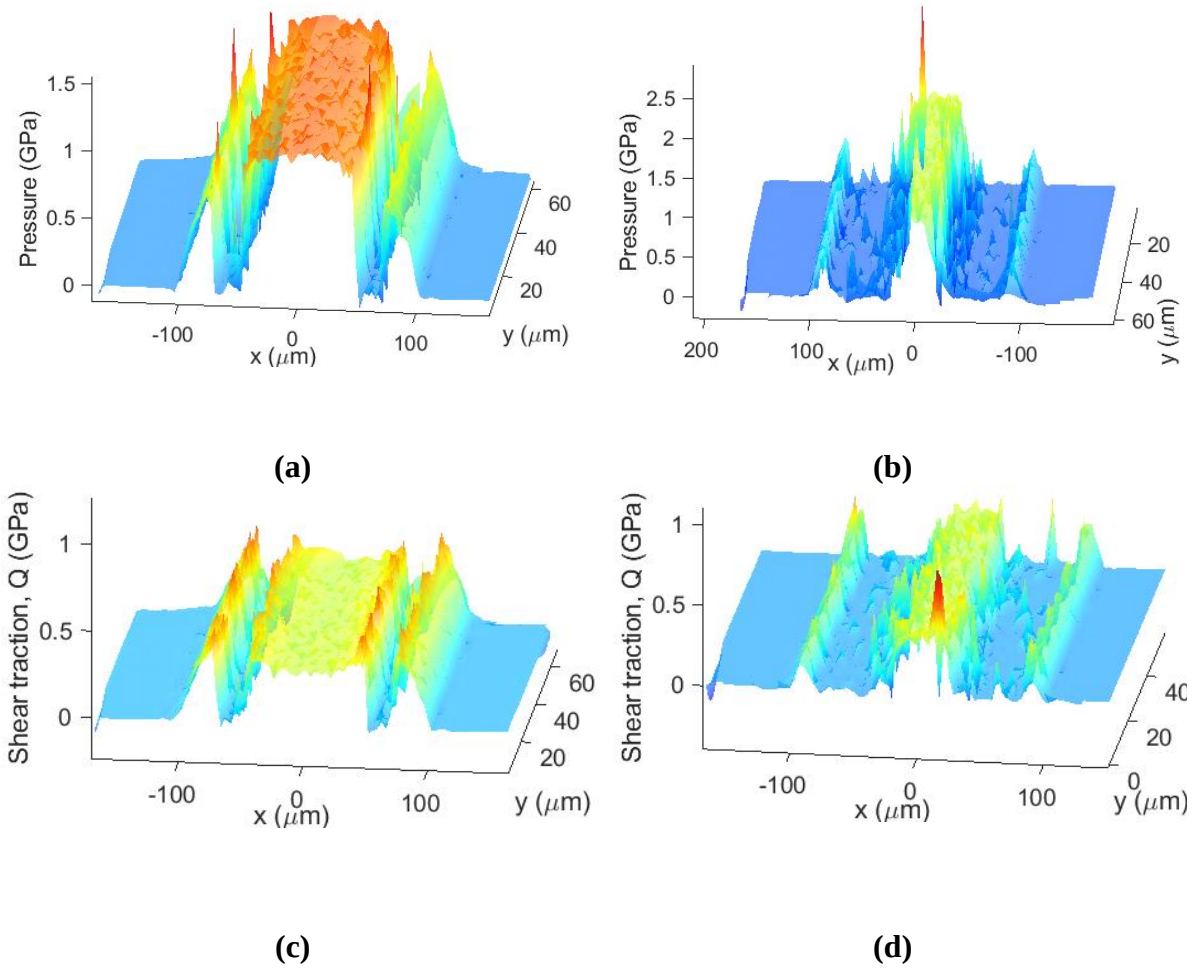

Figure 5.9. 3D normal and shear tractions of the worn model for the circular contact at t_{step}=0.25: (a) normal stress at N=250 cycles, (b) normal stress at N=1000 cycles, (c) shear stress at N=250 cycles, (d) shear stress at N=1000 cycles

5.3.3 Wear volume calculation

In order to calculate the wear volume in the FE model, a MATLAB code was developed to obtain the volume of the elements to be removed in each pass. The corresponding number of cycles was obtained using the damage law developed for this investigation. Figure 5.10 demonstrates the wear volume as a function of cycles in partial slip regime of line contact model. The slope of the linear curve fit in this model provides the wear rate in the fretting process. It is worth mentioning that before wear initiates on the surface, there is an incubation period which is the number of cycles until the first element damages [36,170]. This incubation period was ignored in this analysis [171].

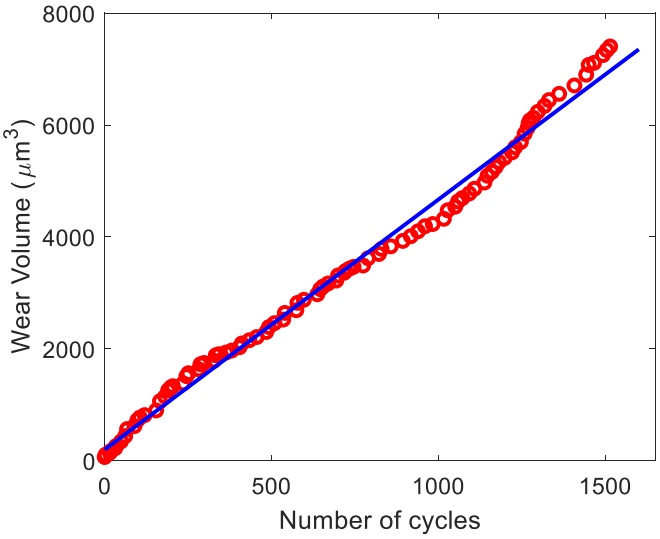

Figure 5.10. General wear volume rate obtained from the FE model in the partial slip regime of line contact model

In the current model, the wear equation was derived based on the dissipated energy method but to compare the results with the known Archard equation, Archard coefficient K is calculated for the current model using the slope as shown in Figure 5.10:

$$K = \frac{Slope * H}{4\delta F_N} \qquad 5.20$$

In this line contact model, the normal load was F_N = 9.4 N, the displacement amplitude was δ = 0.7 μm, and the hardness was H = 2 GPa, therefore the values of K was calculated as K= 1.69e-4 which is within the order of 10^{-6} to 10^{-3}. This is the typical range observed in dry contact experiments of different materials [172,173].

5.3.4 Effect of hardness, modulus of elasticity, and coefficient of friction on wear of line contact model

A parametric study was carried out to evaluate the effect of different material properties on the fretting wear rate phenomenon. For this study, the line contact model was chosen, and a series of models (37 models) were run with different values of hardness, modulus of elasticity, and COF as shown in Table 5.3. The results from this parametric study were used to develop three different wear maps to demonstrate the relationship between these parameters on wear for the line contact model as illustrated in Figure 5.11.

Table 5.3. The parametric study for the partial slip fretting wear in line contact configuration

Material properties	**Value**
Undamaged elastic modulus, E (GPa)	210, 260, 310, 360
Hardness, H (GPa)	1, 2, 3, 4
Coefficient of friction, μ	0.6, 0.7, 0.8, 0.9

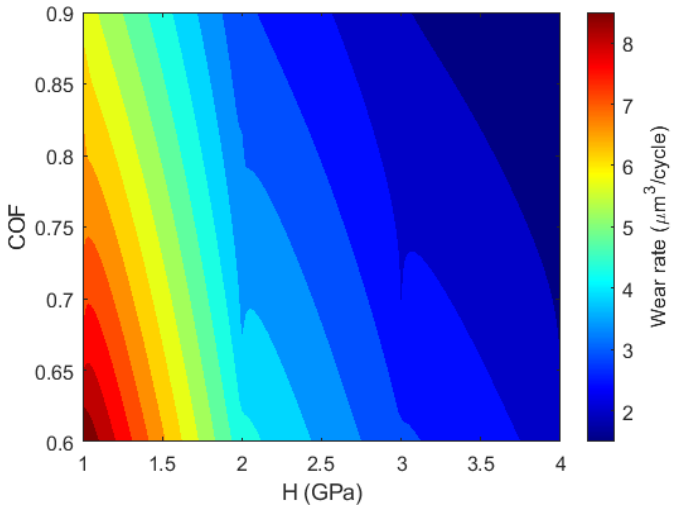

(a)

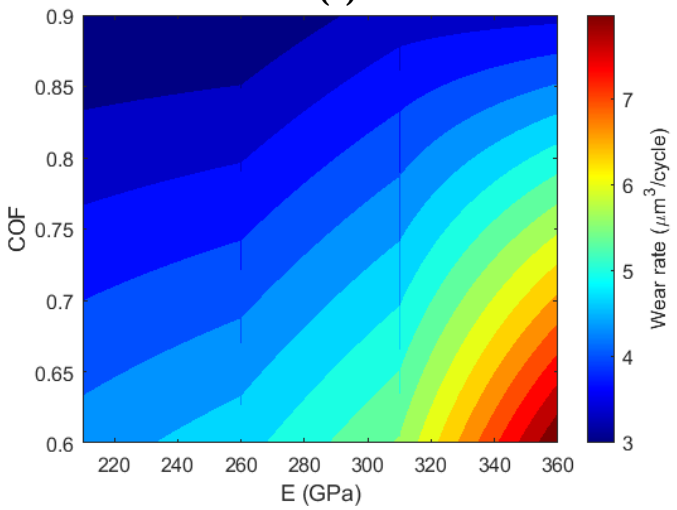

(b)

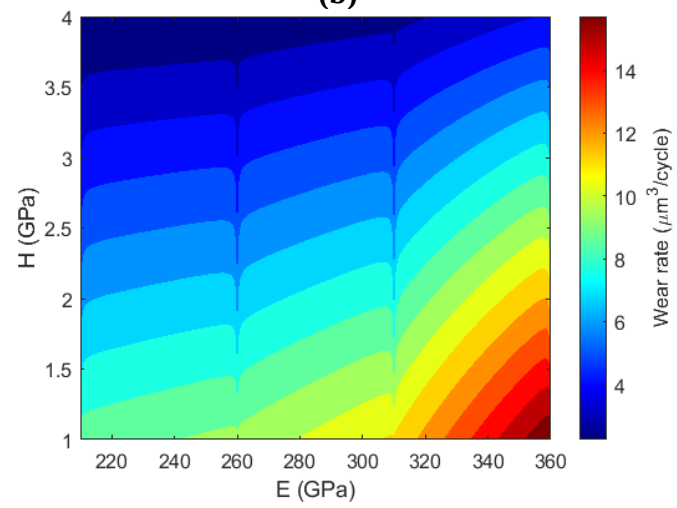

(c)

Figure 5.11. The wear maps of the partial slip regime for the line contact model: (a) H-COF, (b) E-COF, (c) E-H

It is shown in the literature that increase in hardness has an inverse effect on the wear of materials because of delaying the initiation of the crack. To verify the hardness effect in the current partial slip line contact model, four different values of hardness were evaluated, and it is repeated with different values of modulus of elasticity and the COF. It is demonstrated in Figure 5.11a and c that the wear rate decreased as the hardness increased. This is due to the higher wear resistance in the harder material which is consistent with the damage equation that is used in this simulation. According to Equation 5.13, the wear rate decreases as hardness increases.

To evaluate the effect of modulus of elasticity on partial slip fretting wear, four different values of E= 210 GPa, E=260 GPa, E=310 GPa, and E=360 GP were considered in this study. It is shown in Figure 5.11 b, and c that the material with a lower modulus of elasticity had a lower wear rate. In fact, modulus of elasticity affects the wear rate in partial slip regime by modifying the slip zone size. As the modulus of elasticity increased, the percentage of the contact in slip increased which resulted in a higher wear rate of the material. Nikas and Sayles [174] observed the same trend in their fretting fatigue studies.

Table 5.4. Effect of modulus of elasticity on wear rate in the partial slip regime of line contact model

Modulus of elasticity (GPa)	**Hardness (GPa)**	**Coefficient of friction**	**Normal load (N)**	**Percentage of contact in stick**	**Wear rate (μm^3/cycle)**
210	1	0.6	9.42	51.9	8.965
260	1	0.6	9.42	41.2	9.699
310	1	0.6	9.42	30.0	11.370
360	1	0.6	9.42	10.0	16.610

To evaluate the effect of COF on partial slip fretting wear, four different values of μ= 0.6, μ=0.7, μ=0.8, and μ=0.9 were considered in this study. As shown in Figure 5.11 a and b, the wear rate decreased as COF increased. It is demonstrated in Table 5.4 that higher COF resulted in a larger stick zone size and therefore, less material was removed from the slip region.

Table 5.5. Effect of coefficient of friction on wear rate in the partial slip regime of line contact model

Coefficient of friction	Hardness (GPa)	Modulus of elasticity (GPa)	Normal load (N)	Percentage of contact in stick	Wear rate (μm^3/cycle)
0.6	2	310	9.42	30.0	5.686
0.7	2	310	9.42	43.6	4.337
0.8	2	310	9.42	51.9	3.671
0.9	2	310	9.42	58.3	3.490

The wear maps in Figure 5.11 also demonstrates the combined effect of two parameters (E-H, E-COF, and H-COF) on wear rate of materials in partial slip line contact model. It can be concluded that the combination of lower hardness, lower COF and higher modulus of elasticity in partial slip regime can increase the wear rate of the material.

5.3.5 Experimental validation of the fretting wear model for circular contact

Figure 5.12 illustrates the fretting wear test rig (FWTR) [175] with the cross-cylinder configuration used in this investigation. Several experimental tests were conducted for the circular contact configuration in partial slip fretting wear. In this apparatus, a magnetostrictive actuator is used to reciprocate a 9.53 mm (0.375 in) cylinder between two stationary parallel cylinders to have a circular contact. The actuator is controlled using an amplifier and data acquisition card. An inline load cell was used to measure the frictional force and a high precision optical position probe was utilized to measure the displacement of the fretting contact. Before testing, all specimens were cleaned using an ultrasonic cleaner and acetone. Each test was repeated at least three times with the error of measured friction and wear below 5%. Table 5.6 contains the test parameters for the experimental tests.

Table 5.6. Experimental parameters for the partial slip fretting tests

Material properties	Value
Cylinder diameter, D (mm)	9.53
Normal load, F (N)	27
Frequency, f (Hz)	25
Displacement amplitude, δ (μm)	15
Number of cycles, N	4k, 6k, 8k, 10k, 12k

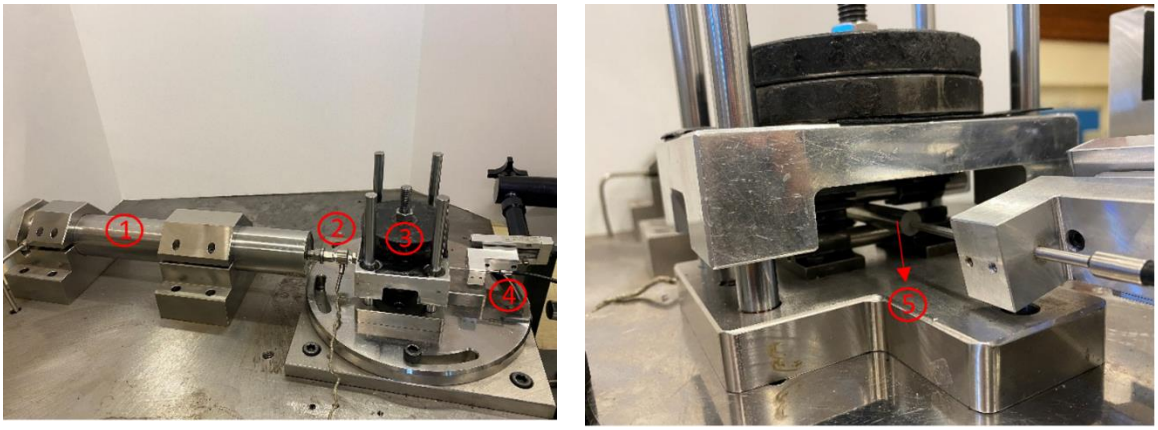

(a) **(b)**

Figure 5.12. The fretting wear test rig (FWTR): 1. Magnetostrictive actuator, 2. Inline load cell, 3. Weights, 4. Optical position sensor, 5. Reciprocating cylinder

Case carburized AISI 8620 steel and AISI 1566 case hardened steel were tested in this investigation. The 8620 steel is a common material for bearing applications which has an average grain size of 10 µm [138,148]. In order to determine the average grain size of 1566 steel, a specimen was etched in Nital 2%. Then, scanning electron microscope (SEM) was utilized to observe the material microstructure as depicted in Figure 5.13. Using the ASTM E112 [136] standard, the grain size of the 1566 steel was measured to be about 15 µm. It is worth mentioning that the FE model for each material was simulated with the corresponding grain size obtained from the experiments.

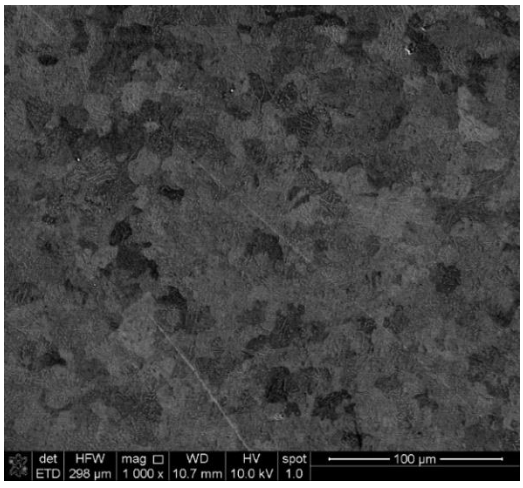

Figure 5.13. SEM of 1566 case hardened steel revealing grain structure.

Nanoindentation tests were performed in order to determine the modulus of elasticity and hardness of the AISI 8620 and 1566 materials. Figure 5.14 and Figure 5.15 depict the values of E and H obtained near the contact surface for the 8620 steel and 1566 steel, respectively. According to the nanoindentation tests, the average values of E= 245 GPa and H=10.6 GPa for the AISI 8620 steel and E=250 GPa and H=10.8 GPa for the AISI 1566 steel were obtained.

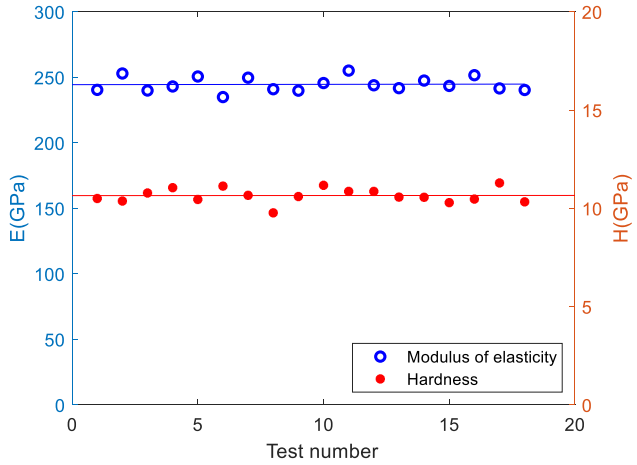

Figure 5.14. Hardness and modulus of elasticity for 8620 steel using nanoindentation near the contact surface

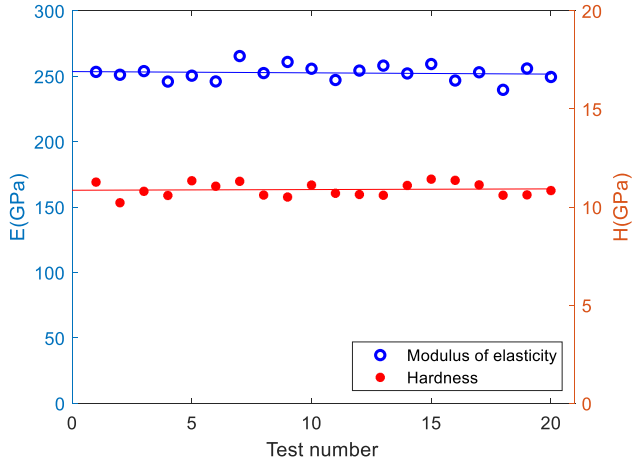

Figure 5.15. Hardness and modulus of elasticity for 1566 steel using nanoindentation near the contact surface

To validate the FE model, the worn surface and the wear rate of the experimental fretting wear tests in partial slip regime were compared with the simulation for both materials. The mean COF of 0.8 was considered in both models according to the experimental tests.

For the AISI 8620 steel, the Hertzian pressure of Pmax=1.61 GPa, half contact of a=89.5 μm, and fretting displacement of δ=15μm were applied to the model according to the experimental conditions. Figure 5.16 demonstrates that the worn surface predicted with the numerical model corroborates well with the experimental results. The stick zone size in both the FE model and experiments reduced as the number of cycles increased. At N=12k cycles, no stick zone remained in the contact. Figure 5.17 compares the wear volume as a function of cycles in the FE model and the experiments for the 8620 steel. It is illustrated that the wear rate obtained from the FE model was in close approximation with the experimental results.

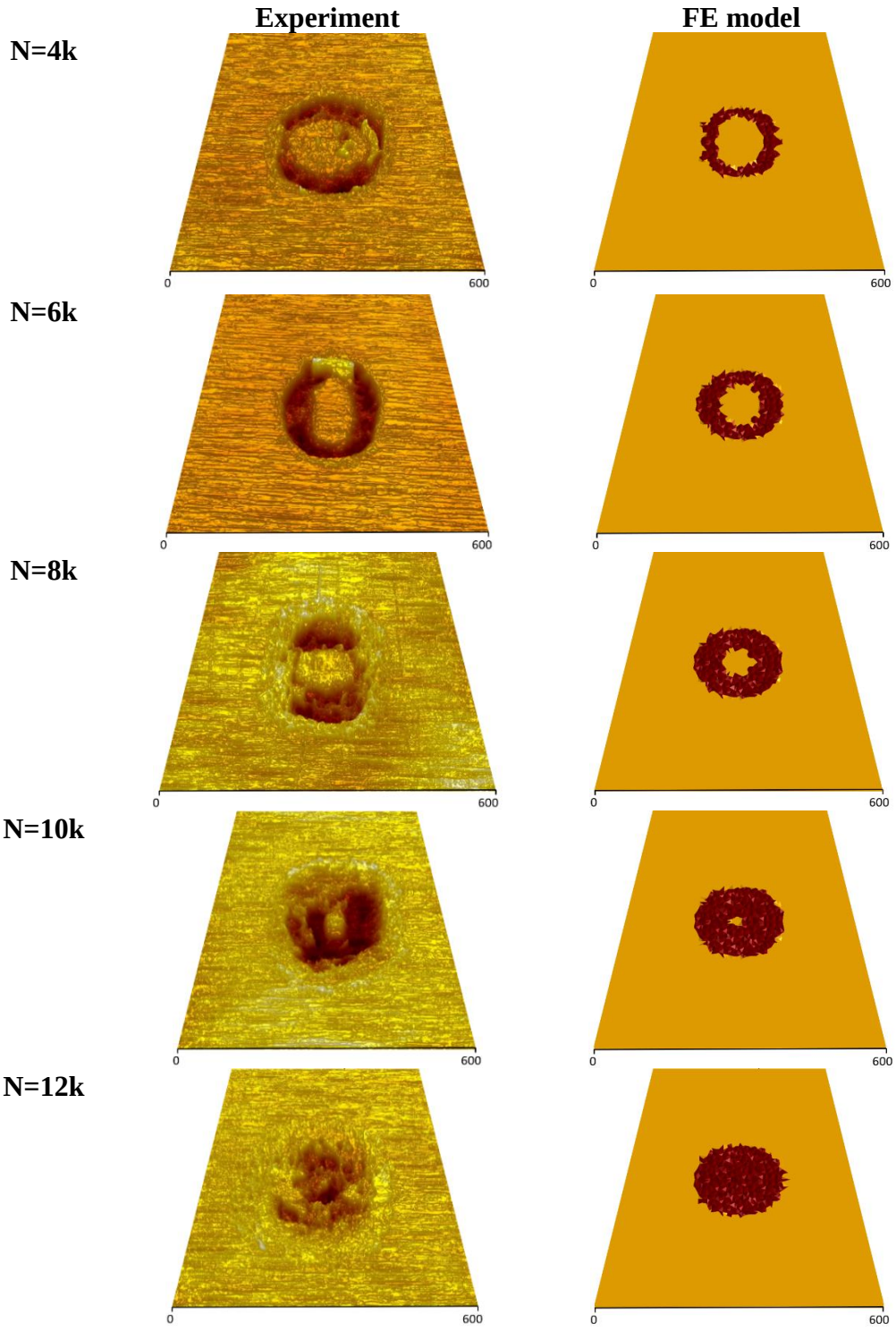

Figure 5.16. Comparison of the experiments and FE models for the partial slip fretting wear of 8620 case hardened steel (unit: microns**)**

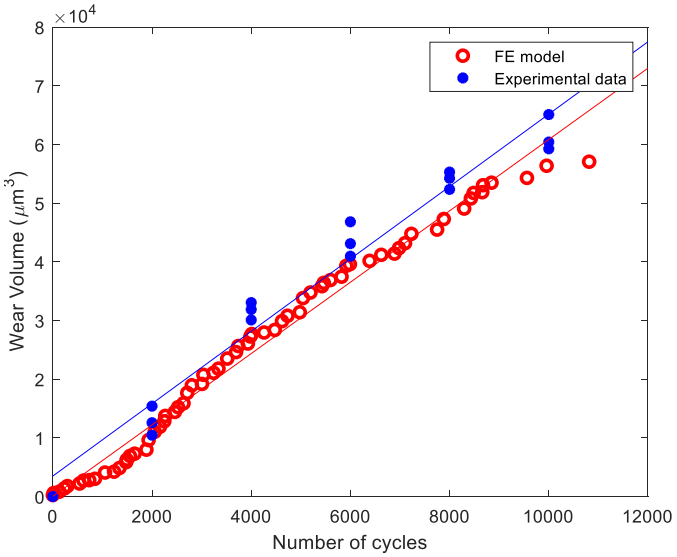

Figure 5.17. Wear volume vs number of cycles for 8620 case hardened steel

For the AISI 1566 steel, the Hertzian pressure of Pmax=1.63 GPa, half contact of a=89 μm, and fretting displacement of δ=15μm were applied to the model according to the experimental conditions. Due to the close values of E and H for AISI 1566 steel compared to the AISI 8620 steel, a very close behavior was observed for this material as well. Figure 5.18 and Figure 5.19 depict the worn surface and wear rate comparison of the FE model with the experimental fretting tests, respectively. A good correlation between the model and experiments was observed. Please note that the effect of wear debris and surface roughness was ignored in these partial slip models. Especially, the third body effects could be important in the partial slip fretting wear as these particles can affect the wear rate of the material but for this study, it is assumed that the particles are not trapped in the contact.

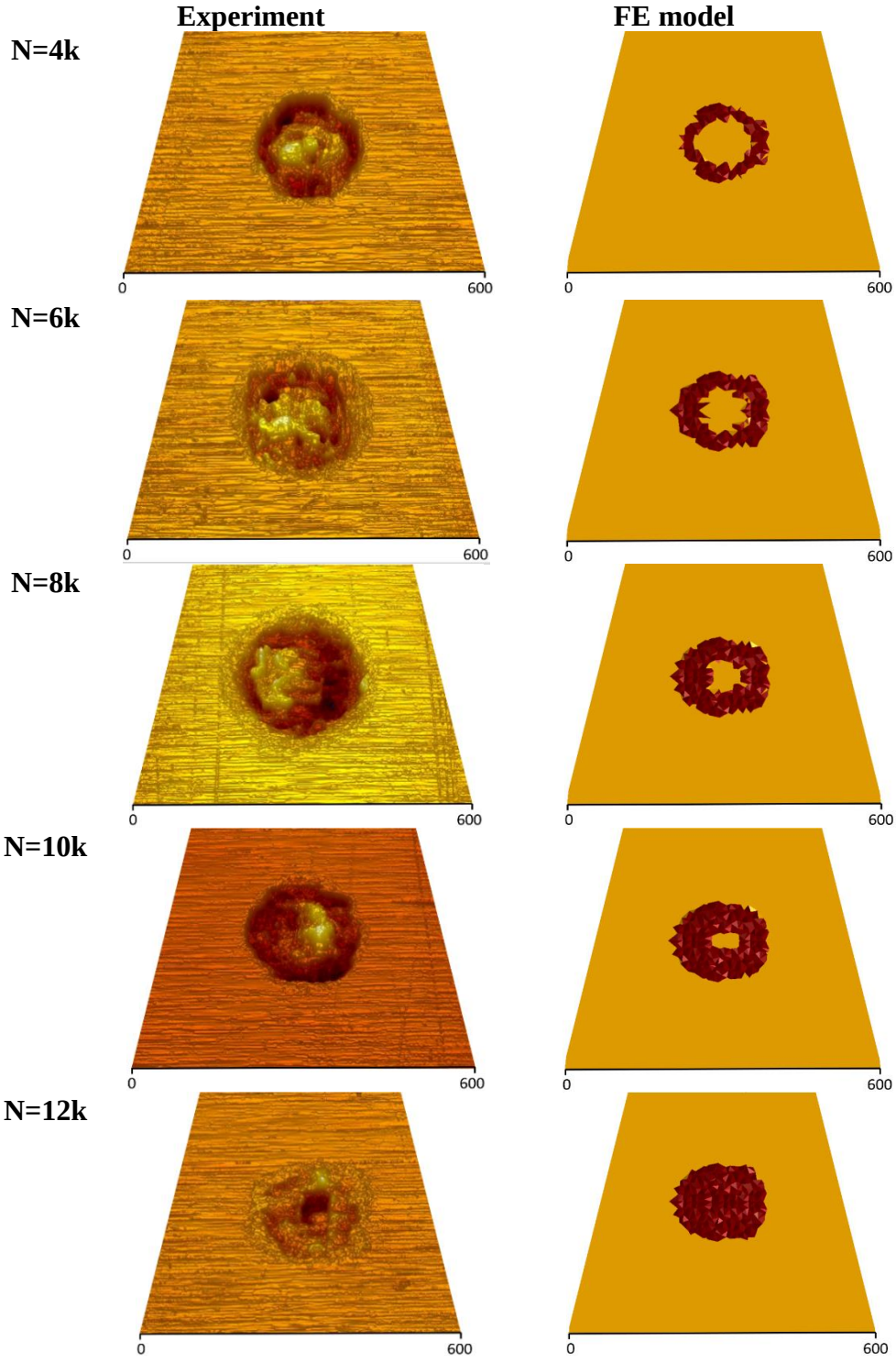

Figure 5.18. Comparison of the experiments and FE models for the partial slip fretting wear of 1566 case hardened steel (unit: microns)

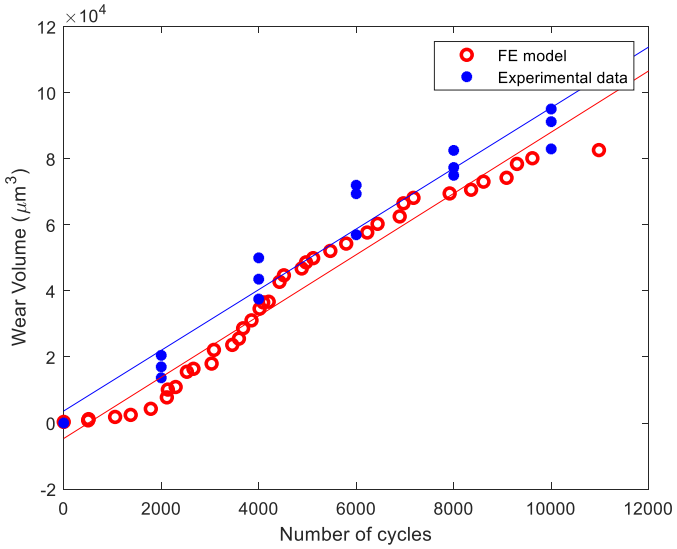

Figure 5.19. Wear volume vs number of cycles for 1566 case hardened steel

5.4 Conclusion

In this investigation a 3D finite element model was developed to investigate fretting wear study of Hertzian circular and line contacts. A wear law was derived based on the dissipated energy method. This wear law was implemented in a stress-based damage mechanics approach to determine the worn surface shape and the wear rate. To simulate the microstructure of the material, Voronoi tessellation was used to represent the grains of the material. This model was developed for the partial slip fretting wear of similar materials in contact. Instead of putting two FE bodies in contact, the normal and shear tractions were applied to the FE body using a subroutine which decreased the computational time significantly. The tractions subroutine was developed for both line and circular contacts. The resultant stress fields on the surface and the internal stresses for the circular and line contacts in the partial slip regime were nearly identical with the analytical solutions which verified the accuracy of the boundary conditions, mesh quality, and domain size.

A parametric study was conducted for the line contact model to evaluate the effect of different material properties on the wear rate of model. To this end, different values of modulus of elasticity, hardness, and COF were applied to the model and the resultant wear rates were compared. It was illustrated that increase in the hardness and COF had an inverse effect on the wear rate while an increase in modulus of elasticity resulted in a higher wear rate in the partial slip

regime. Also, three wear maps were created to show the combine interactions of hardness, modulus of elasticity, and COF on the wear rate of the material.

To verify the FE model developed, an existing fretting wear machine was used to determine fretting wear of circular contacts in partial slip and compared with the corresponding FE model. Two different hardened steels, AISI 8620 and AISI 1566, were considered for these experiments. The modulus of elasticity and hardness of each material were obtained using nanoindentation tests near the contact surface and then the corresponding grain size, load, displacement amplitude and the COF were applied to the FE model according to the experimental tests. It was shown that the partial slip worn surface at different cycles and wear rate predicted by the FE model correlated well with the experimental tests for both materials.

6. CURED, DRY SOLID LUBRICANT ON BEARING STEEL FOR SIGNIFICANT FRICTION AND WEAR REDUCTION UNDER HIGH CONTACT PRESSURE

6.1 Introduction

The majority of engineering systems can encounter a damage because of wear and friction. One of the reasons could be related to the mechanical components and manufacturing instruments with parts in contact and relative motion [84]. Lubrication is one of the most widely recognized methods of improving the efficiency, performance, and lifetime of mechanical components by reducing friction between two sliding surfaces. The use of liquid lubricants such as organic oils [85] is one of the most common means of reducing energy losses at moving interfaces. Furthermore, the importance of additives in the tribological performance of lubricating oils has been investigated by many researchers [86–91]. However, liquid lubricants are not good candidates in high-temperature or low-pressure applications due to their low resistance to vaporization [92,93]. On the other hand, dry solid lubricants have proven to be a vital option for high-load, high-speed, and extreme environmental conditions. Various types of solid lubricants such as molybdenum disulfide (MoS2) [94], boron nitride (BN) [95], polytetrafluoroethylene (PTFE) [96], and graphene [97] have been studied.

In this chapter, a cured Aremco-Bond™ 570 polymer-graphene-zinc oxide composite was developed to increase the adhesion and durability of the coating on contact surfaces and to reduce friction and wear in bearing steels under high contact pressure. The proposed composite was made from graphene, zinc oxide particles, and a specific binder including butanone and isopropanol and was laminated on a bearing steel disks. A sliding wear test with a ball-on-disk configuration was used to measure the tribological performance of the composite coating under a contact pressure of 1 GPa. Scanning electron microscope (SEM), energy dispersive X-ray spectrometry (EDX) analyses and X-ray powder diffraction (XRD) were conducted to determine the topography and morphology of the composite coating and the wear scars. Raman spectroscopic analysis and Fourier transformed infrared spectroscopy (FTIR) were conducted to study the mechanical and chemical durability of the composite coating .The surface adhesion properties of the coating were measured using the Nanovea® scratch tester and compared to an earlier graphene-zinc oxide-PVDF coating [111].

6.2 Introduction

Zinc oxide powder was prepared by calcining a zinc acetate dihydrate (Sigma-Aldrich Corp.) precursor inside a horizontal quartz tube furnace (MTI Corp.) under a continuous compressed air flow at a rate of approximately 100 mL min-1. The furnace was heated at the constant temperature rate of 10°C min-1 to a dwell temperature of 500°C for three hours. Subsequently, the product was cooled down to room temperature, and then ground and homogenized using a mortar and pestle.

A special product (Aremco-Bond 570) composed of butanone, isopropanol, phenol, carbon black, formaldehyde, and o-cresol was used as a binder in the coating composite. It was first mixed with acetone in a 1:1 volume ratio for three hours to create a uniform mixture, each 1 mg of the mixture containing ~0.22 mg of dry solid contents. Then, to prepare the lubricant slurry, 40 wt% of the as-prepared binder mixture (based on dry content), 10 wt% of the as-prepared ZnO, and 50 wt% of graphene (United Nanotech Innovations Pvt. Ltd.) were continuously stirred inside a scintillation vial (Thermo Fisher Scientific Co.) for 12 hours.

Lamination of the slurry onto the steel disks was performed using a spin coater (Laurell Technologies WS-650Mz-23NPPB). The spin speed was set at 500 rpm and the spin time was set to one minute. The coated disks were thermally cured at 80°C for 20 minutes and then at 180°C for 30 minutes in air using a heating plate. Due to heat dissipation into the surrounding air, the approximate temperature on the disk top (where the composite coating was mounted) was about 160°C. After completing the process, the coating covered the 52100 steel disk surface uniformly and was measured to be approximately 15 μm thick.

6.3 Characterization Techniques

The XRD patterns of the zinc oxide-graphene composite lubricant coating (ZnO-G-lubricant), Aremco binder coating, graphene powder, and as-prepared ZnO powder were recorded using a Rigaku SmartLab XRD fitted with a CuKα radiation source. The Rigaku scanning range is 20°-100° and the scan rate is 3° min-1. For XRD measurement, both the ZnO-G-lubricant coating and Aremco binder coating were applied onto glass slides (to mitigate XRD interference from the steel substrate) and cured using the same procedure mentioned previously.

SEM imaging was carried out using a JEOL JCM-6000 Plus NeoScope Benchtop SEM. To examine the composite coating, the prepared mixture was dried on a disk, loaded inside the microscope chamber, and then evacuated to a high vacuum. After optimization of the electron beam, micrographs of the coating and the wear scars were captured in different magnifications. EDX analyses (JEOL Ltd.) were conducted to determine the relative proportions of coating ingredients, especially carbon and zinc oxide.

Raman spectroscopy was conducted using a Raman microscope (DXR, Thermo Fisher Scientific). Before performing the tests, the laser was calibrated using polystyrene calibration. The mapping from the samples was captured by using an aperture green laser with a 25 μm beam diameter, wavelength of 532 nm and power of 5mW. A total of five exposures with a collection time of 10 s were averaged for each single mapping pattern, and all the patterns were smoothed and background-reduced for better interpretation. To generate each mapping, at least 150 sampled points were selected at 5 μm increments.

Fourier transform infrared (FTIR) spectral analysis was carried out using an Agilent Technologies Cary 630 FTIR in the frequency range of 500 cm−1 to 4000 cm−1 for the composite coating solution.

6.4 Tribological Tests

Sliding wear tests were conducted in the ball-on-disk configuration on a Bruker UMT TriboLab™. A stationary 6.35 mm diameter 52100 steel ball with surface roughness of 50 nm and a rotary 70 mm diameter 52100 steel uncoated disk with surface roughness of 500 nm and the coated disk with surface roughness of 2000 nm were used. The normal load applied in all the tests varied from 4 N to 12 N (average Hertzian pressure of 1.01 GPa to 1.45 GPa). The sliding distance was varied from 280 m to 680 m based on the wear track radius and number of cycles. The linear velocity was varied from 0.15 m/s to 1.2 m/s in different radii on the disk (with the frequency ranging from 0.9 to 9.1 Hz). A position probe with the resolution of 0.1 μm was used for in-situ measurement of wear depth during the test and an optical surface profilometer was utilized for wear measurements after the test. Prior to testing, all uncoated specimens were cleaned using acetone to remove residual debris on the surfaces. Each test was repeated at least three times with an error of measurement of wear and friction below 5%. Table 6.1 shows the experimental parameters of the sliding wear tests.

Table 6.1. Experimental parameters for sliding wear tests

Experimental Parameters	**Value**
Normal load	4 N, 8N, 12N
Total displacement	280-680 m
Frequency	0.9-9.1 Hz
Cycles	0.5K, 1K, 2K, 3K, 5K
Gas atmosphere	Air
Temperature	25°C

To elucidate the adhesive properties of the newly developed coating comprising of butanone and isopropanol binder, we performed scratch tests. The scratch testing method is a very reproducible quantitative technique to compare the cohesive or adhesive properties of coatings by observing the amount of wear and friction under the critical loads at which coating damage appears. In the case of coated samples with a high load regime, the damage usually occurs as a result of coating detachment from the substrate via spalling or chipping.

To observe the behavior of the coatings, a progressive load test was conducted in which the process of scratching was controlled and monitored in order to determine when a recognizable coating damage occurred. In this application, the Nanovea tester in scratch testing mode was used to measure and compare the load required to cause adhesion damage in the new thermally cured, advanced polymer-graphene-zinc oxide-based coating and the earlier graphene-zinc oxide-PVDF coating. [111] The coating was deposited at a thickness of 30-50 μm on a metal substrate. A 200 μm diamond-tipped stylus was used in a progressive load ranging from 0.015 N to 20.00 N to scratch the coating. The point where the coating damaged by cracking was documented. The modified ASTM D7027 was followed as a reference to determine the testing parameters. Table 6.2 shows the parameters used for the scratch tests.

Table 6.2. Parameters for scratch tests following ASTM D7027

Parameters	Description
Load type	Progressive
Initial load	0.015 N
Final load	20.00 N
Loading rate	20.00 N/min
Scratch length	1.6 mm
Scratching speed, dx/dt	1.601 mm/min
Pre-scan load	0.200 N
Post-scan load	0.200 N
Indenter geometry	90° conical
Indenter tip radius	200 μm
Indenter material (tip)	Diamond

6.5 Results and Discussion

In this section, formation of composite, coefficient of friction, wear and adhesion analysis are explained in detail.

6.5.1 Formation of Composite

The cured, dry solid lubricant was composed of graphene, zinc oxide, and Aremco binder. In this coating, multilayer graphene is the primary component of lubrication and synergistic adhesion is related to the zinc oxide and the binder. The zinc oxide provides adhesion between the lubricant and the substrate surface, an occurrence known as an intraphase adhesion — while the binder provides the adhesion within the composite itself, a condition called an interphase adhesion [111].

XRD analysis of the ZnO-G composite lubricant indicated the presence of both crystalline ZnO and graphene components in the cured coating (Figure 6.1). The XRD peaks for ZnO and graphene in the composite coating matched well with the corresponding powder samples, suggesting no crystal structure changes in the ZnO and graphene particles during the sample

preparation and curing steps. The Aremco binder, however, exhibited no distinguishable XRD peaks, so it could not be readily identified in the composite lubricant XRD. Additionally, EDX analysis showed that the composite coating had a uniform distribution of zinc oxide and graphene (Figure 6.2).

The color pixel maps of EDX show that the coating consisted of large amounts of micro-scale graphene particles (indicated by C) and smaller amounts of zinc oxide (indicated by Z) particles, which were scattered uniformly. Based on the characterization of the coating, it can be concluded that the composition of the coating included a random arrangement of micro-scale graphene particles with a mono-disperse mixture of nano-scale zinc oxide and the binder. In fact, the preparation process used for this coating kept its crystallographic order in the coating.

Raman spectroscopy of the coating on the tribo-tested disk is shown in Figure 6.3a. It is demonstrated that the binding of carbon within graphene didn't change in the coating preparation process. The vibration modes of D, G, and 2D corresponding to the Raman excitation frequency of 1332, 1580, 2668 cm-1 are exhibited which are related to the graphene in the composite coating [176]. It is worth mentioning that the spectral features of the binder and ZnO are not captured in the composite spectrum as graphene dominated Raman intensity.

Figure 6.3b shows the FTIR spectrum of the coating solution. The FTIR spectrum of composite solution displayed several characteristic absorptions bands of graphene/binder containing groups. A broad and strong peak around 1710 cm-1 is attributed to the C=O vibration [177,178] and sharp peaks at around 1360 cm-1 and 1220 cm-1 correspond to the C-O and O-H respectively [177,179]. These peaks could be attributed to the presence of graphene (or its oxide) and elements of binder. The small peaks of 1415 cm-1 and 1080 cm-1 could be related to the C-O as well [180–183]. These peaks could be attributed to the solvents which acted as dispersant in the slurry of the composite coating. Broad absorption at low frequency of about 500 cm-1 is attributed to the vibration of the bulk ZnO [184,185].

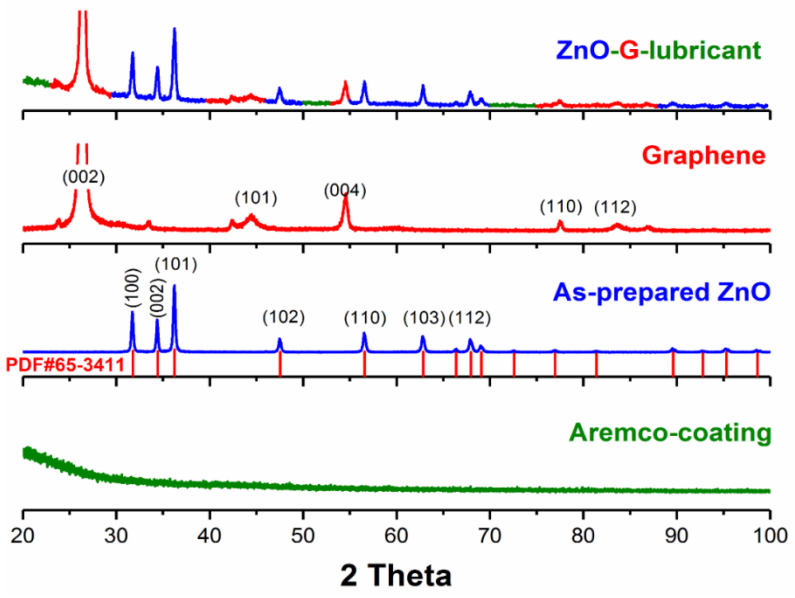

Figure 6.1. X-ray powder diffraction patterns of ZnO-G lubricant on a glass slide and individual components of graphene powder, as-prepared ZnO powder, and Aremco-only coating on a glass slide.

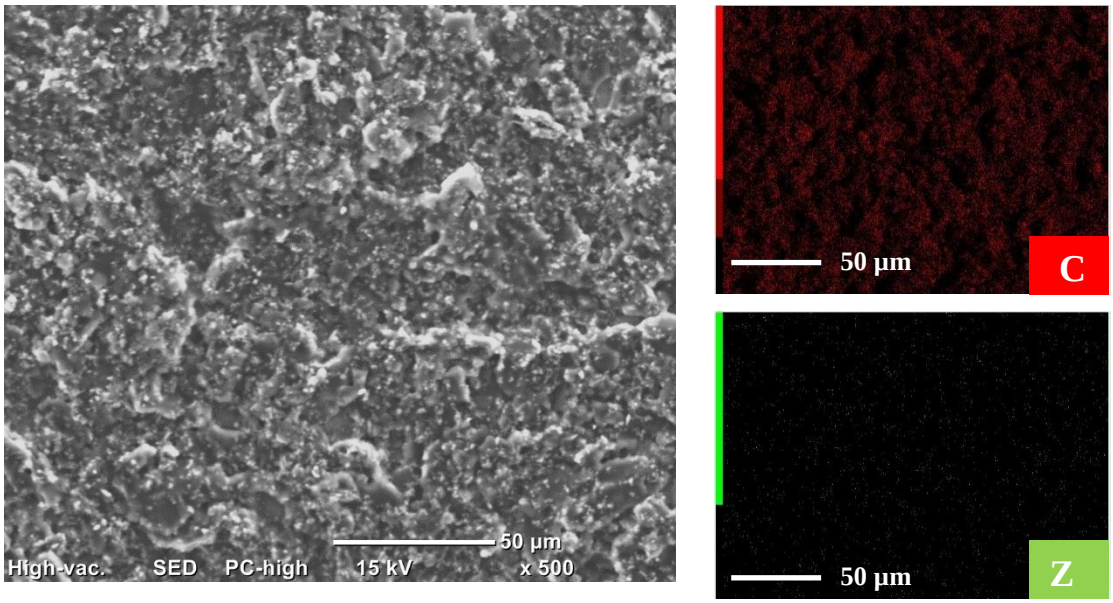

Figure 6.2. SEM and EDX micrographs of the composite coating

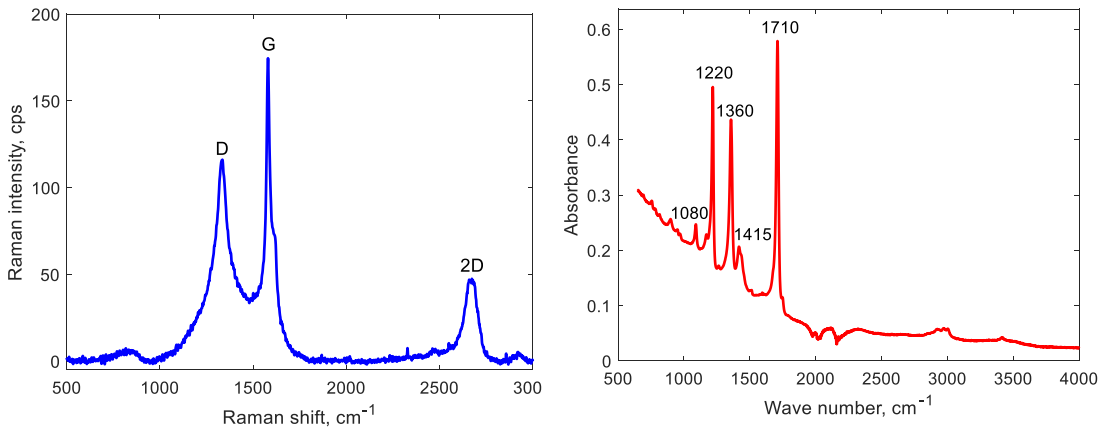

(a) **(b)**

Figure 6.3. (a) Raman spectroscopy of the composite coating. (b) FTIR spectra of the ZnO-G lubricant solution

6.5.2 Wear, Coefficient of Friction and Adhesion Analysis

The tribological performance of the solid lubricant-coated surface was superior to that of the uncoated surface. Under a normal load of 4 N and duration of 3000 cycles, the COF declined about 82% in the graphene-based coating compared to the uncoated contact (Figure 6.4). The COF in the uncoated surface started at 0.69, and after 500 cycles, rose to the steady state value of 0.84. In contrast, the COF in the coated surfaces started at 0.14 and reached the steady state of 0.15, exhibiting more stable behavior during the test.

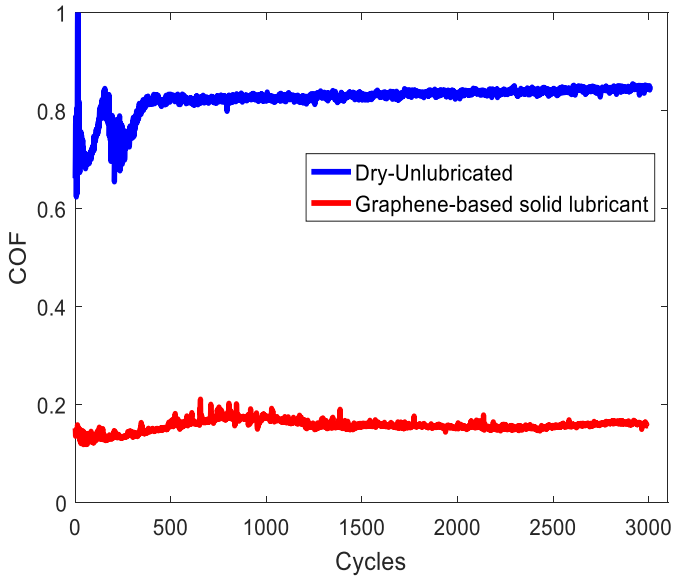

Figure 6.4. Comparison of the COF obtained by graphene-coated and uncoated surfaces

In-situ measurement of wear rate was conducted using a proximity probe during the sliding wear test to monitor the wear depth in both the coated and uncoated specimens. Figure 6.5 shows that after around 3000 cycles with a normal load of 4 N, the total wear depth for the uncoated surface tests was higher than that of the tests conducted on the graphene coated surface. In fact, it took around 3000 cycles for the 15 µm coating to be removed completely, and only very small wear on the subsurface of the disk occurred after that. The residual coating actually enhanced the friction and wear reduction by preventing direct contact of the surfaces during the sliding test.

The reduction of wear on the specimens was further illustrated by scanning the ball and disk using a profilometer and SEM. Figure 6.6 shows that after the uncoated surface sliding test, the wear scar that formed on the ball was 610 µm in diameter, while the graphene coated surface sliding test showed just a few discernible scratches on the surface with diameters of about 210 µm. Figure 6.7 also shows the wear scars on the flat surfaces of the uncoated and coated disks, as captured by SEM. The uncoated disk developed a large wear track of 17 µm in depth, but on the coated disk, the coating was utilized to the degree that only a few scratches were created and some of the grinding lines of the disk were visible.

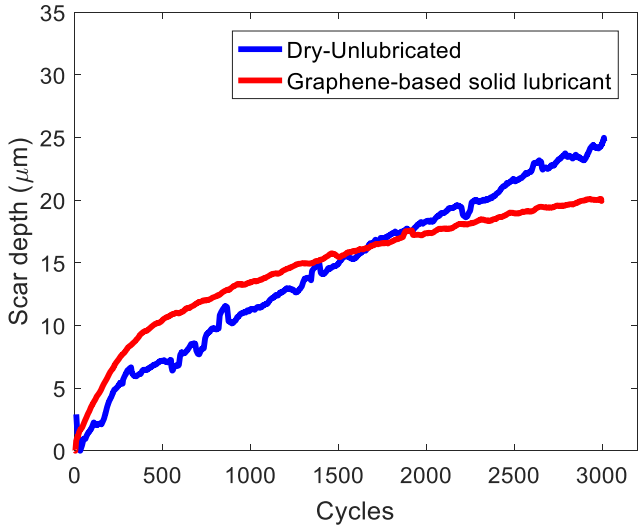

Figure 6.5. In-situ measurement of wear depth for the graphene-coated and uncoated specimens

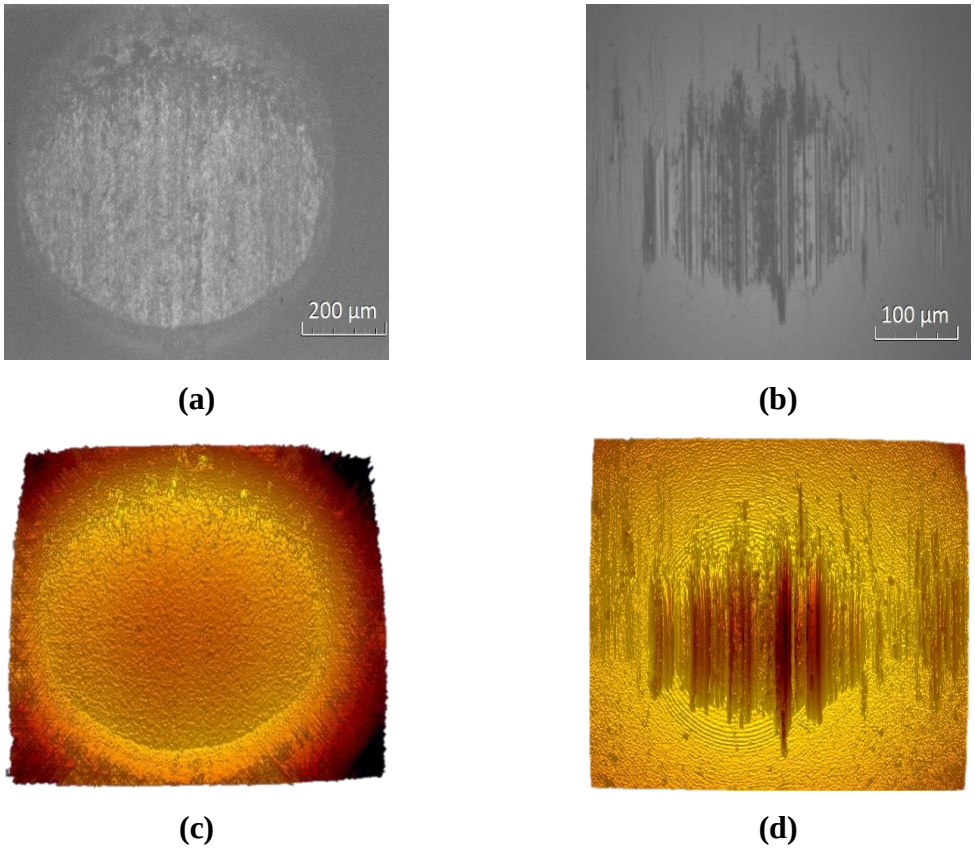

Figure 6.6. Optical micrograph of the wear scar on the tested balls after 3000 cycles in sliding wear tests: (a) ball on uncoated disk, (b) ball on coated disk, and 3D surface reconstruction of the wear scar on the tested balls after 3000 cycles in sliding wear tests: (c) ball on uncoated disk, (d) ball on coated disk

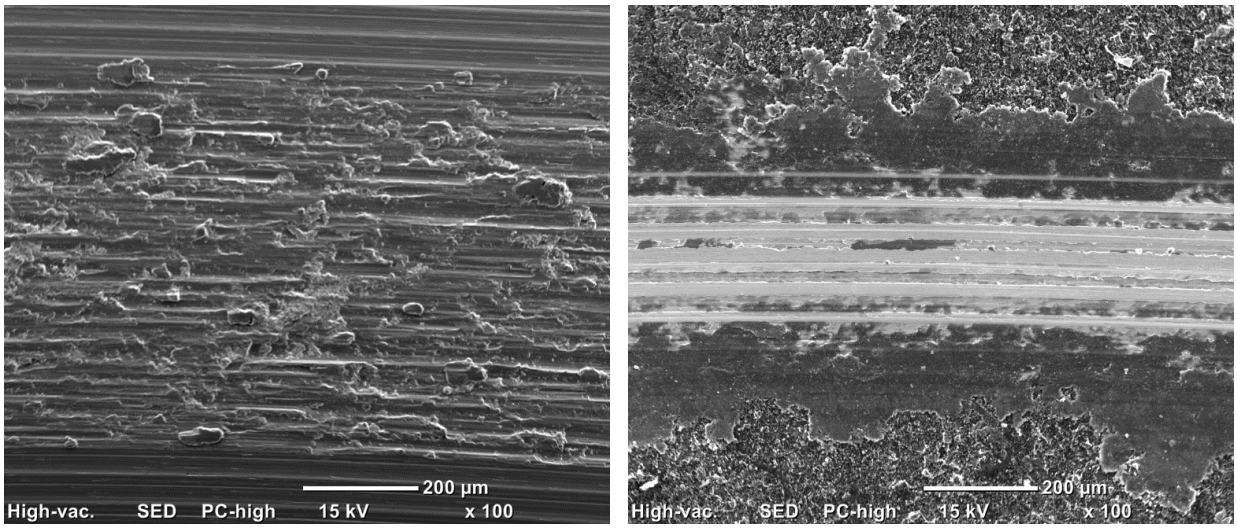

(a) **(b)**

Figure 6.7. SEM micrographs of disks after 3000-cycle wear tests: (a) uncoated disk, (b) coated disk

To better illustrate the amount of wear for the coated and uncoated tests, the profiles of the scar depth measured by the profilometer are shown in Figure 6.8 for the ball and disk. It is demonstrated that after 3000 cycles, a very small amount of the materials was removed from both ball and disk in the coated test, while the depth of the scars on both ball and disk for the uncoated test is quite noticeable.

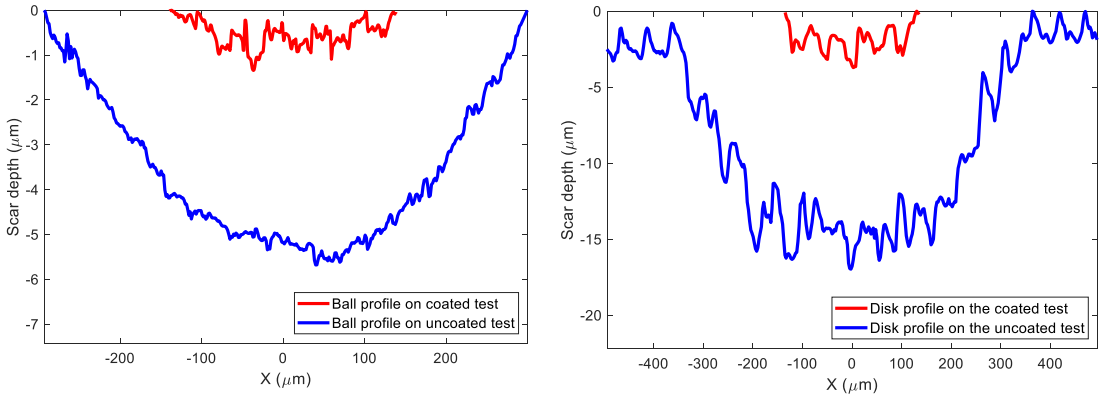

(a) **(b)**

Figure 6.8. Two-dimensional surface profiles of the ball and disk specimens in the coated and uncoated tests: (a) ball, (b) disk

By measuring the wear volume removed from the ball using an optical profilometer on both coated and uncoated tests, the total wear volume related to the balls are shown in Table 6.3.

Table 6.3. Wear volume on the ball for the coated and uncoated tests

Test	**Total wear volume of the ball (μm^3)**
Coated	5.27e5
Uncoated	4.41e3

To evaluate the influence of sliding distance on the tribological behavior of the composite coating, the COFs of three different tests were measured and compared with a normal load of 4 N and sliding distances of 295 m, 500 m and 675 m, which correspond to 2000, 3000, and 5000 cycles, respectively. It was observed that after 3000 cycles, the COF started to increase due to the generation of wear particles at the contact surfaces and degradation of the graphene lubricant (Figure 6.9).

Figure 6.10 shows the wear scar formation for different sliding distances on the balls in the coated surface sliding tests. The 5000-cycle test had a visible scar with a diameter of 500 µm, while the 3000-cycle and 2000-cycle tests resulted in only a few scratches on the ball surface.

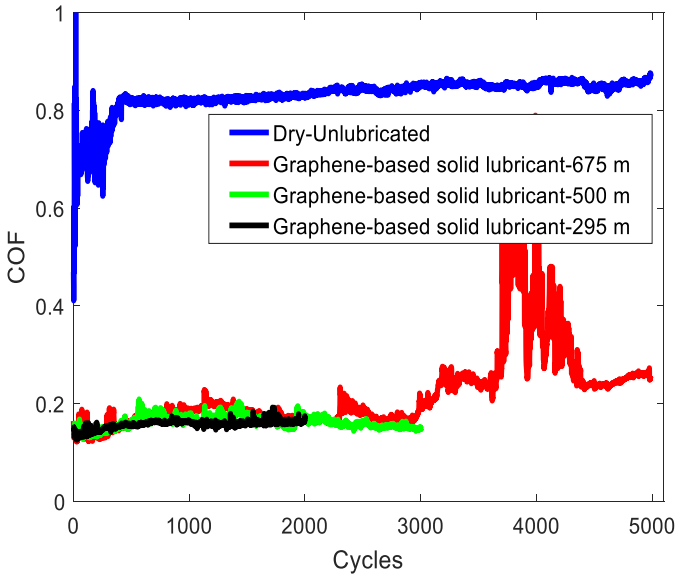

Figure 6.9. Effect of sliding distance on COF of coated surface for unlubricated and lubricated surfaces

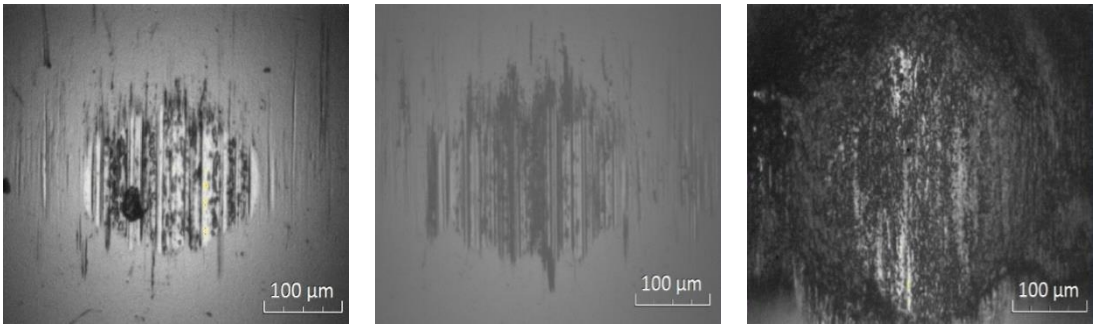

(a) **(b)** **(c)**

Figure 6.10. Optical micrographs of wear scars on balls at different sliding distances for the graphene coated surface sliding test: (a) 2000 cycles, (b) 3000 cycles, (c) 5000 cycles

To evaluate the influence of normal load on the tribological behavior of the composite coating, the COFs of three different tests were measured with normal loads of 4, 8, and 12 N corresponding to Hertzian pressures of 1.01, 1.27, and 1.45 GPa, respectively (Figure 6.11). The COF remained almost constant for the different loads up to 500 cycles. The 12 N normal force test resulted in faster utilization of the coating such that after 500 cycles, the COF started to increase. However, the test with normal force of 8 N lasted longer (more than 1000 cycles). Therefore, it can be concluded that as the amount of load increases, the durability of the coating diminishes due to the higher wear rate at the higher normal load. The consistency of the solid lubricant is related to the native mechanical strength of graphene [100] and the strong adhesive properties of zinc oxide and the binder. The solid lubricant's high-bearing load capacity demonstrates its potential for high-pressure applications.

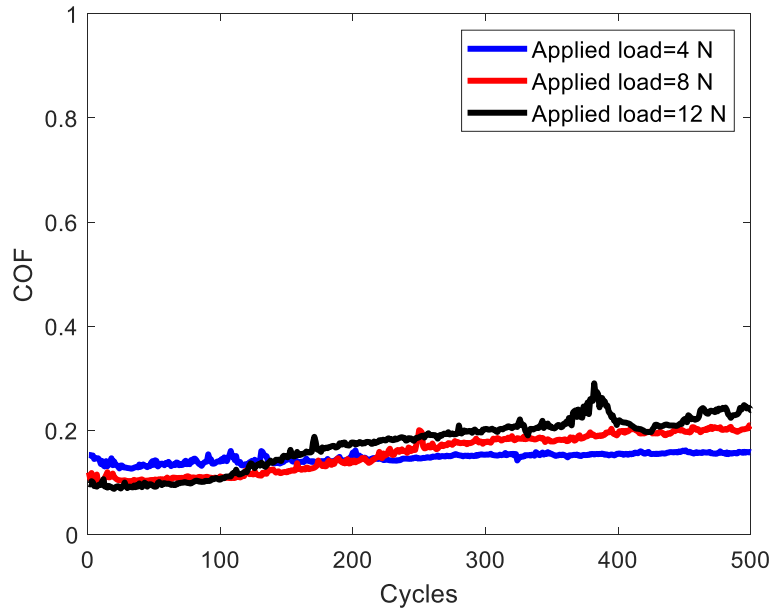

Figure 6.11. Effect of normal load on COF of coated surface

To study the effect of sliding speed on the tribological behavior of the composite coating, the COFs of three different tests were measured with linear velocities of 0.15, 0.6, and 1.2 m/s (Figure 6.12). It is demonstrated that by increasing the sliding speed, the COF decreases marginally. Mohanty et al. [186] observed the same behavior in their wear study of a specific coating. They noted that by increasing the sliding speed, the frictional heat flux and local temperature increase accordingly. Therefore, this frictional heating softens the local surface layer and lowers the shear strength without a significant change in the coating's bulk properties.

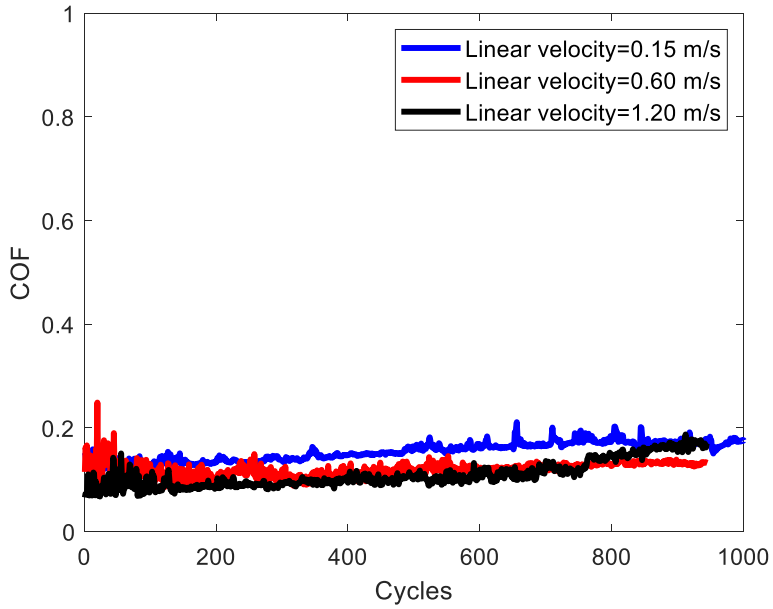

Figure 6.12. Effect of linear velocity on COF of coated surface

To study the coating's interfacial adhesion properties, the scratch test method was used. This comparison of the newly developed cured composite coating and the earlier composite coating [111] demonstrated that the new coating was much more robust. Moreover, the test results indicated that the new coating had a four times lower friction coefficient and less wear than the previous version of the graphene-based composite coating, mainly because of the fact that previous coating damaged quickly and exposed the steel substrate. The micrographs in Figure 6.13 show the adhesion damage of these two coatings. Detailed scratch test results are shown in Table 6.4

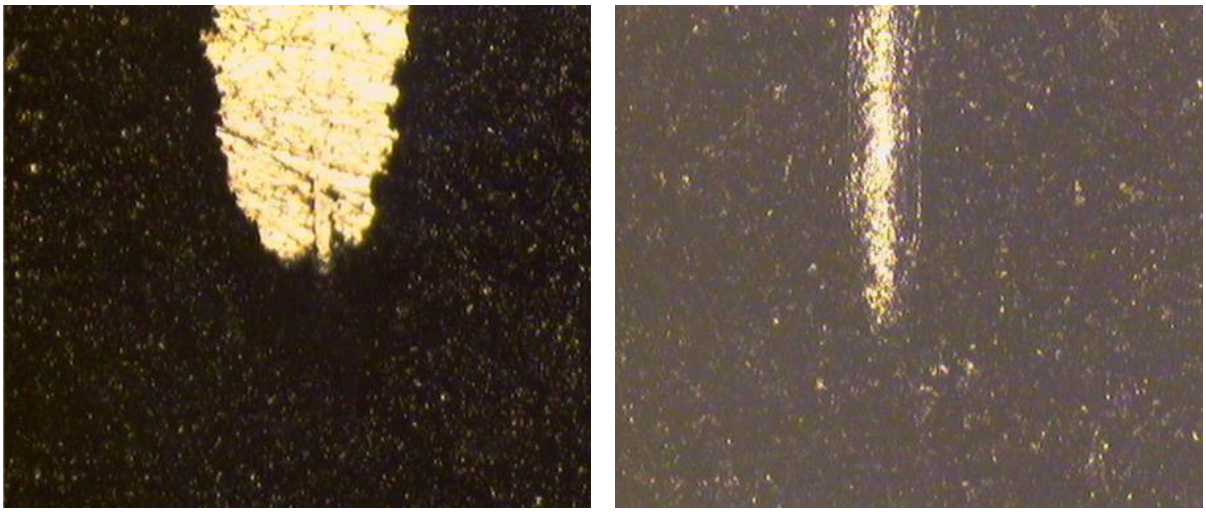

(a) **(b)**

Figure 6.13. Micrograph of coating adhesion damage: (a) PVDF-graphene-ZnO based composite coating, (b) new, cured Aremco-Bond™ 570 polymer-graphene-zinc oxide based composite coating

Table 6.4. Results of damage and coefficients of friction for the scratch tests

	Scratch width (mm)	Coefficient of friction
PVDF based coating	0.27 ± 0.013	0.03
New, cured Aremco-Bond™ 570 polymer-graphene-zinc oxide composite coating	0.07 ± 0.003	0.0075

Numerous studies explained the importance of graphene as a promising protective coating for various components [187–189]. It was demonstrated that the tribological properties of graphene is highly related to the adhesion between the graphene and substrate. Actually, the wear properties of graphene improved when it is tightly bonded to the substrate. Furthermore, the role of zinc oxide can be explained as the reduction of the native friction of graphene alone, mitigation of the friction which occurred by the binder, and improvement on adhesion of graphene to the substrate [109,190–193]. In fact, the durability and high tribological performance of the current coating are associated with three main factors: first, high modulus of elasticity of graphene (1000 GPa) and intrinsic stress strength (130 GPa), which result in having effective mechanical strength [100]. Second, strong adhesion and anti-wear properties of zinc oxide. Third, improvement of the adhesion between graphene and zinc oxide by adding a binder.

6.5.3 Post-diagnostic Surface Analysis

To identify the mechanical and chemical durability of the graphene lubricant, the wear tracks of the disks for the tests with normal load of 4N at 2000 and 3000 cycles were analyzed using Raman spectroscopy. Accordingly, the composite coating on the disk was tracked by the intense vibration mode of graphene at frequency 1580 cm-1 (Figure 6.14). The digital photograph of the wear scar after the test demonstrates a dark opaque film covering the sides of the scar. Correlation of spectral color map to the photograph illustrates the protective film has high graphene content especially at 2000-cycle test. Figure 6.14a shows the high graphene content of the wear track formed from the 2000-cycle test. The 3000-cycle test resulted in a wear track with lower graphene content than the 2000-cycle test, but still a noticeable amount of graphene adhered to the track area, and that prevented excessive wear on the ball and disk. The adherence of graphene around the wear track is attributed to the zinc oxide additive, which performed as a binding agent between the graphene and the steel surfaces.

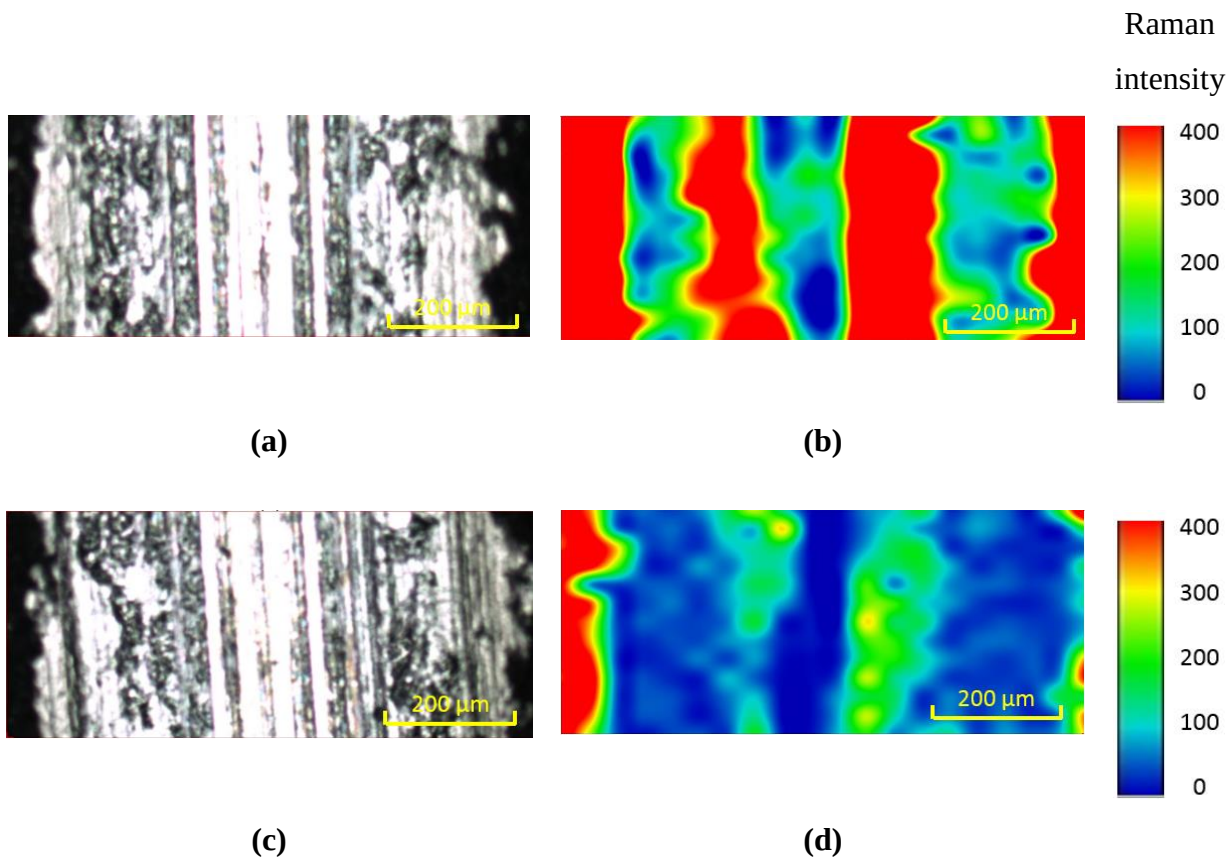

Figure 6.14. Raman spectroscopy map of disk substrate surface: (a, b) 2000 cycles, (c, d) 3000 cycles

6.6 Conclusions

Significantly improved tribological performance and durability of graphene-rich composite coatings as solid lubricants in high-contact pressure applications is demonstrated via utilization of Aremco-Bond™ 570 polymer enhancing superior adhesion properties. Prior to performing the wear tests, characterization of the cured lubricant confirmed that the prepared composite coating was a physical mixture of its ingredients, without any chemical or crystallographic alteration. Sliding wear tests with a ball-on-disk configuration, at Hertzian pressure of 1 GPa on the 15 µm coated disk, demonstrated that the dry solid lubricant sustained noticeable friction and wear reduction up to a 3000 cycles duration compared to the uncoated surfaces.

Further tests under different loads, sliding distances, and sliding velocity revealed that the durability of the coating decreased as the load or displacement increased or velocity decreased, and the decrease was due to an increase in the wear rate of the composite. The adhesion, friction

and wear properties of the newly developed coating showed considerable improvement over the properties of the previously developed graphene-zinc oxide coating. Optical and spectroscopic analysis after the tribological tests demonstrated the superior tribofilm of composite lubricant on the contact surfaces

7. SUMMARY, CONCLUSIONS AND FUTURE WORK

7.1 Summary and Conclusions

In chapter one, the topic of fretting wear is introduced with brief discussions of historical background, fretting wear mechanisms and current wear models. In addition, the fretting wear at elevated temperatures is discussed. Then, the effect of deformable third body particles which is one of the main concerns in a fretting contact is also analyzed. One of the remedies for the wear failures is using lubricants in contact. A brief description of solid lubricants for reducing the coefficient of friction and wear rate is mentioned in this chapter. Finally, a review of torsion fatigue study of different materials is discussed as shear mode of failure is of significant importance in triaxial state of stress present for ball and rolling element bearings and machine component which are subject to fretting fatigue.

Chapter two described the effect of temperature and inert environment on the fretting wear of Inconel 617. Gross sliding fretting tests for the 6.35 mm-diameter ball-on-flat configuration with a normal load of 4 N and displacement of 250 μm were conducted. In-situ fretting wear measurement was used to continuously monitor the change in wear depth of the scar during the process. It was observed that as the number of cycles in both room temperature and in air were increased, the wear rate decreased such that there was a bilinear wear behavior, including a severe running-in wear at the beginning followed by a mild steady state wear. The COF and friction loops were plotted for different conditions of the tests. It was observed that in both helium and air environments, the COF decreased as the temperature increased which was attributed to the change in oxidation and material properties of the specimens at elevated temperatures. Furthermore, the wear rate decreased compared to the room temperature test in both environments. At 750°C, the wear rate in the helium environment was higher than in the air environment. At 750°C in air, a significant amount of stable oxide film covered the surface of the scar, leading to the decrease in wear rate, while in the helium environment, fewer protective oxides particles were present in the contact zone, leading to the increased wear rate of the specimens. Topography and morphology of the scars were performed using SEM and EDX. A high percentage of oxide particles were observed to be adhered to the contact surfaces at 750°C in air, which led to lower friction and wear.

Chapter three focused on experimentally and analytically investigating the effect of temperature on torsional fatigue of Inconel 617. In the experimental aspect, a modified MTS machine was used by to obtain torsional fatigue (SN) results under fully revered conditions at 850°C. The MTS machine was modified by high temperature gripers with cooling fins. The final failure surface of the test specimen depicted that they had similar failure modes which was observed by helical fracture planes at 45° angle with the specimen torsional axis. The helical shape of the failure surface depicted that normal stress was dominant in propagation as normal stresses were maximum on these planes in pure torsion. In the analytical aspect of this study, a 3D elastic-plastic FEM was developed to investigate the torsional fatigue damage of the material at high temperatures. Voronoi tessellation was used to model the microstructure of the material and boundaries of the grains were considered to be weak planes in the material. Continuum damage mechanics approach was applied to simulate the material degradation during the fatigue process. Mises based plasticity model combined with a linear kinematic hardening approach was used to include the influence of plasticity into the model. The model predicted fatigue lives and crack growth path which corroborated well with the high-temperature torsional fatigue experiments.

Chapter four investigated the development of a 3D FE model to study the effect of third body particles on a partial slip fretting wear in Hertzian point contacts. The effect of third body particles in an initial stage of a fretting process on different contact parameters such as contact pressure, shear stress, hardening properties, and slip behavior was studied. Plastic material properties were included in the model as there was a very high contact pressure at the location of the wear debris. A fundamental investigation was carried out to understand the effect of plasticity on contact pressure, force-deformation, and contact slip. Because of high plastic deformation on the particles, a platelet structure was observed for the wear particles which was similar to the experimental observations. Also, it was depicted that by increasing the number of particles in contact, more load was carried by the wear particles which affect the wear rate of the material. Fretting loops of the model in different cycles were compared and the relation between the number of cycles and the hardening process was evaluated. While the wear particles were placed in the slip zone of the contact, local stick-slip behavior was observed at the location of particles that could be an indication of crack nucleation on the first bodies. In addition, several cases were considered to model wear debris with different material properties than first bodies due to

oxidation and plastic deformation. The results indicate that harder wear particles had a higher contact pressure and lower slip at the location of particles which affect the wear rate of the bodies.

Chapter five discussed about a 3D finite element model that was developed to investigate fretting wear study of Hertzian circular and line contacts. A wear law was derived based on the dissipated energy method. This wear law was implemented in a stress-based damage mechanics approach to determine the worn surface shape and the wear rate. To simulate the microstructure of the material, Voronoi tessellation was used to represent the grains of the material. This model was developed for the partial slip fretting wear of similar materials in contact. Instead of putting two FE bodies in contact, the normal and shear tractions were applied to the FE body using a subroutine which decreased the computational time significantly. The tractions subroutine was developed for both line and circular contacts. The resultant stress fields on the surface and the internal stresses for the circular and line contacts in the partial slip regime were nearly identical with the analytical solutions which verified the accuracy of the boundary conditions, mesh quality, and domain size. A parametric study was conducted for the line contact model to evaluate the effect of different material properties on the wear rate of model. To this end, different values of modulus of elasticity, hardness, and COF were applied to the model and the resultant wear rates were compared. It was illustrated that increase in the hardness and COF had an inverse effect on the wear rate while an increase in modulus of elasticity resulted in a higher wear rate in the partial slip regime. Also, three wear maps were created to show the combine interactions of hardness, modulus of elasticity, and COF on the wear rate of the material. To verify the FE model developed, an existing fretting wear machine was used to determine fretting wear of circular contacts in partial slip and compared with the corresponding FE model. Two different hardened steels, AISI 8620 and AISI 1566, were considered for these experiments. The modulus of elasticity and hardness of each material were obtained using nanoindentation tests near the contact surface and then the corresponding grain size, load, displacement amplitude and the COF were applied to the FE model according to the experimental tests. It was shown that the partial slip worn surface at different cycles and wear rate predicted by the FE model correlated well with the experimental tests for both materials.

Chapter six talked about a significantly improved tribological performance and durability of graphene-rich composite coatings as solid lubricants in high-contact pressure applications via utilization of Aremco-Bond™ 570 polymer enhancing superior adhesion properties. Prior to

performing the wear tests, characterization of the cured lubricant confirmed that the prepared composite coating was a physical mixture of its ingredients, without any chemical or crystallographic alteration. Sliding wear tests with a ball-on-disk configuration, at Hertzian pressure of 1 GPa on the 15 μm coated disk, demonstrated that the dry solid lubricant sustained noticeable friction and wear reduction up to a 3000 cycles duration compared to the uncoated surfaces. Further tests under different loads, sliding distances, and sliding velocity revealed that the durability of the coating decreased as the load or displacement increased or velocity decreased, and the decrease was due to an increase in the wear rate of the composite. The adhesion, friction and wear properties of the newly developed coating showed considerable improvement over the properties of the previously developed graphene-zinc oxide coating. Optical and spectroscopic analysis after the tribological tests demonstrated the superior tribofilm of composite lubricant on the contact surfaces.

7.2 Future Work

This section suggests further research efforts for continued investigations of fretting wear phenomenon. Considering the current state of understanding of fretting wear, there are several promising directions in which more research can be conducted. The wear models described in the previous chapters can be extended to include effects that are more comparable to experiments or in actual operation. The future work avenues are a result of initial project goals as well as investigations conducted during this study.

7.2.1 Effect of Surface Roughness on Wear

In the FE models developed in this study, it is assumed that the surfaces of the contacts are smooth while in reality, each surface has different roughness properties that could affect the wear rate of materials. Therefore, is necessary to implement the effect of roughness using an elastic-plastic material model to accurately evaluate the contact stresses. Since the rough surface contact model is based on force displacement equilibrium, relationship between force and displacement in the three regions: Linear Elastic, Elastic-Plastic and Perfectly Plastic can be obtained with the aid of Finite Element Analysis of Hertzian circular contact. A non-Gaussian surface generator can be implemented at various scales to investigate the effect of various roughness scales. Some research

studies demonstrated a significant reduction in wear rates when an elastic plastic material model is incorporated. Evolution of surface roughness parameters such as RMS roughness, skewness and kurtosis can be investigated. The effect of skewness and kurtosis on wear rates can also be evaluated. Therefore, by incorporating an elastic-plastic material response as experienced during laboratory or field conditions, the surface roughness model is expected to yield results which are more in agreement with published experimental work

7.2.2 Experimental Evaluation of Third Bodies on Fretting Contact

In a fretting contact, the two rubbing surfaces in sliding or fretting contact are called “first bodies”, while the wear debris or particles generated between them are called “third body”. This concept was introduced by Godet in the 1970s to connect the lubrication theory with dry contacts. In addition to the computational model proposed in this thesis, the effect of third body particles in wear can be experimentally studied. Pin on disk and reciprocating sliding experiments can be conducted to study the entrapment of third body particles and their possible role in reducing coefficient of friction. To achieve this, grooves of different depths and widths can be laser machined on one of the contacting bodies at various angles with respect to the angle of motion. It is expected that varying degree of third body particles will be retained in each situation which could influence the shear force

7.2.3 Wear Studies of Coating at Elevated Temperatures

Solid lubricant is a vital choice for reduction of wear in different applications. A lot of industrial components are running at elevated temperatures that could affect the performance of the solid lubricants significantly. The relationship between temperature and friction force is not well understood for most materials despite that in many engineering applications the operating temperature exceeds 100 ºC. Therefore, a study demonstrating the effect of temperature and normal force or displacement amplitude on the friction behavior would advance our knowledge of the friction phenomena. Also, a thermal finite element model can be developed to implement the effect of temperature in the model and predict the amount of wear for different coatings at different conditions.

REFERENCES

[1] M. Odfalk, O. Vingsbo, Influence of Normal Force and Frequency in Fretting©, Tribol. Trans. 33 (1990) 604–610. doi:10.1080/10402009008981995.

[2] S.R. Pearson, P.H. Shipway, J.O. Abere, R.A.A. Hewitt, The effect of temperature on wear and friction of a high strength steel in fretting, Wear. 303 (2013) 622–631.

[3] Y. Qiu, B.J. Roylance, The effect of lubricant additives on fretting wear, Lubr. Eng. 48 (1992) 801–808.

[4] A. Ahmadi, J. Tang, V.G. Pol, F. Sadeghi, K.K. Mistry, Binder Mediated Enhanced Surface Adhesion of Cured, Dry Solid Lubricant on Bearing Steel for Significant Friction and Wear Reduction under High Contact Pressure, Carbon N. Y. 146 (2019) 588–596.

[5] A. Sharma, F. Sadeghi, A. Sharma, Experimental investigation of fretting wear of coated spring clip and inlet ring in land-based gas turbines at elevated temperature, Wear. 446–447 (2020) 203200. doi:10.1016/j.wear.2020.203200.

[6] O. Vingsbo, S. Söderberg, On fretting maps, Wear. 126 (1988) 131–147. doi:10.1016/0043-1648(88)90134-2.

[7] Z.R. Zhou, K. Nakazawa, M.H. Zhu, N. Maruyama, P. Kapsa, L. Vincent, Progress in fretting maps, Tribol. Int. 39 (2006) 1068–1073. doi:10.1016/j.triboint.2006.02.001.

[8] P. Blanchard, C. Colombie, V. Pellerin, S. Fayeulle, L. Vincent, Material Effects in Fretting Wear: Application to Iron, Titanium, and Aluminum Alloys, n.d.

[9] J. Beard, The avoidance of fretting, Mater. Des. 9 (1988) 220–227. doi:10.1016/0261-3069(88)90034-9.

[10] J.F. Archard, Contact and rubbing of flat surfaces, J. Appl. Phys. 24 (1953) 981–988. doi:10.1063/1.1721448.

[11] S. Fouvry, P. Kapsa, L. Vincent, Quantification of fretting damage, Wear. 200 (1996) 186–205.

[12] EDEN, E. M., The endurance of metals, Proc. Inst. Mech. Eng. 4 (1911) 875–881. https://ci.nii.ac.jp/naid/10026822762 (accessed June 22, 2020).

[13] G.F.S., The rusting of steel surfaces in contact, Proc. R. Soc. London. Ser. A, Contain. Pap. a Math. Phys. Character. 115 (1927) 472–483. doi:10.1098/rspa.1927.0104.

[14] CATTANEO, C., Sul Contatto di due Corpi Elasticie : Distribution Locale Degli Sforzi, Reconditi Dell Acad. Naz. Die Lincei. 27 (1938) 474–478. https://ci.nii.ac.jp/naid/10008660819 (accessed June 22, 2020).

[15] MINDLIN, R. D., Compliance of Elastic Bodies in Contact, J. Appl. Mech., ASME. 16 (1949) 259–268. https://ci.nii.ac.jp/naid/10013415139 (accessed June 22, 2020).

[16] I.G. Goryacheva, P.T. Rajeev, T.N. Farris, Wear in partial slip contact, J. Tribol. 123 (2001) 848–856.

[17] D.A. Hills, A. Sackfield, R.J.H. Paynter, Simulation of fretting wear in halfplane geometries: part 1—the solution for long term wear, J. Tribol. 131 (2009) 31401.

[18] D. Nowell, Simulation of fretting wear in half-plane geometries—Part II: analysis of the transient wear problem using quadratic programming, J. Tribol. 132 (2010) 21402.

[19] H. Ben Dhia, M. Torkhani, Modeling and computation of fretting wear of structures under sharp contact, Int. J. Numer. Methods Eng. 85 (2011) 61–83. doi:10.1002/nme.2958.

[20] L. Johansson, Numerical simulation of contact pressure evolution in fretting, J. Tribol. 116 (1994) 247–254.

[21] I.R. McColl, J. Ding, S.B. Leen, Finite element simulation and experimental validation of fretting wear, Wear. 256 (2004) 1114–1127.

[22] C. Paulin, S. Fouvry, C. Meunier, Finite element modelling of fretting wear surface evolution: Application to a Ti--6A1--4V contact, Wear. 264 (2008) 26–36.

[23] B.D. Leonard, F. Sadeghi, S. Shinde, M. Mittelbach, A numerical and experimental investigation of fretting wear and a new procedure for fretting wear maps, Tribol. Trans. 55 (2012) 313–324.

[24] A. Cruzado, M.A. Urchegui, X. Gómez, Finite element modeling and experimental validation of fretting wear scars in thin steel wires, Wear. 289 (2012) 26–38.

[25] L. Rodr\'\iguez-Tembleque, M.H. Aliabadi, Numerical simulation of fretting wear in fiber-reinforced composite materials, Eng. Fract. Mech. 168 (2016) 13–27.

[26] Q. Dong, K. Zhou, W.W. Chen, Q. Fan, Partial slip contact modeling of heterogeneous elasto-plastic materials, Int. J. Mech. Sci. 114 (2016) 98–110.

[27] T. Yue, M.A. Wahab, Finite element analysis of fretting wear under variable coefficient of friction and different contact regimes, Tribol. Int. 107 (2017) 274–282.

[28] A.L.M. Tobi, W. Sun, P.H. Shipway, Investigation on the plasticity accumulation of Ti-6Al-4V fretting wear by decoupling the effects of wear and surface profile in finite element modelling, Tribol. Int. 113 (2017) 448–459.

[29] P.J. Ashton, A.M. Harte, S.B. Leen, A strain-gradient, crystal plasticity model for microstructure-sensitive fretting crack initiation in ferritic-pearlitic steel for flexible marine risers, Int. J. Fatigue. 111 (2018) 81–92.

[30] B. Bhattacharya, B. Ellingwood, Continuum damage mechanics analysis of fatigue crack initiation, Int. J. Fatigue. 20 (1998) 631–639.

[31] P. Ireman, A. Klarbring, N. Strömberg, A model of damage coupled to wear, Int. J. Solids Struct. 40 (2003) 2957–2974.

[32] N. Raje, F. Sadeghi, R.G. Rateick, A statistical damage mechanics model for subsurface initiated spalling in rolling contacts, J. Tribol. 130 (2008) 42201.

[33] N. Raje, T. Slack, F. Sadeghi, A discrete damage mechanics model for high cycle fatigue in polycrystalline materials subject to rolling contact, Int. J. Fatigue. 31 (2009) 346–360.

[34] A. Warhadpande, B. Jalalahmadi, T. Slack, F. Sadeghi, A new finite element fatigue modeling approach for life scatter in tensile steel specimens, Int. J. Fatigue. 32 (2010) 685–697.

[35] T. Zhang, P.E. McHugh, S.B. Leen, Finite element implementation of multiaxial continuum damage mechanics for plain and fretting fatigue, Int. J. Fatigue. 44 (2012) 260–272.

[36] B.D. Leonard, F. Sadeghi, S. Shinde, M. Mittelbach, Rough surface and damage mechanics wear modeling using the combined finite-discrete element method, Wear. 305 (2013) 312–321.

[37] A. Ghosh, B. Leonard, F. Sadeghi, A stress based damage mechanics model to simulate fretting wear of Hertzian line contact in partial slip, Wear. 307 (2013) 87–99.

[38] by Rebecca David Ibrahim, Modeling, Analysis, and Validation of Temperature Dependent Vibration Induced Fretting Corrosion, 2010. https://etd.auburn.edu/handle/10415/2122 (accessed June 22, 2020).

[39] A. Ahmadian, A. Shafiee, N. Aliahmad, M. Agarwal, Overview of Nano-Fiber Mats Fabrication via Electrospinning and Morphology Analysis, Text. 2021, Vol. 1, Pages 206-226. 1 (2021) 206–226. doi:10.3390/TEXTILES1020010.

[40] A. Shafiee, M.T. Ahmadian, M. Hoviattalab, Traumatic Brain Injury Caused by +Gz Acceleration, Proc. ASME Des. Eng. Tech. Conf. 3 (2016). doi:10.1115/DETC2016-59021.

[41] A. Shafiee, A. Ahmadian, A. Akbari, A Parametric Study of Mechanical Cross-Coupling in Parallel-Kinematics Piezo-Flexural Nano-Positioning Systems, Open J. Appl. Sci. 11 (2021) 596–613. doi:10.4236/ojapps.2021.115043.

[42] A. Iwabuchi, Fretting wear of inconel 625 at high temperature and in high vacuum, Wear. 106 (1985) 163–175.

[43] C.H. Hager, J.H. Sanders, S. Sharma, Effect of high temperature on the characterization of fretting wear regimes at Ti6Al4V interfaces, Wear. 260 (2006) 493–508.

[44] X.-Y. Zhang, J.-H. Liu, Z.-B. Cai, J.-F. Peng, M.-H. Zhu, P.-D. Ren, Experimental Study of the Fretting Wear Behavior of Incoloy 800 Alloy at High Temperature, Tribol. Trans. 60 (2017) 1110–1119.

[45] R.C. Bill, Fretting wear and fretting fatigue-how are they related, J. Lubr. Technol. 105 (1983) 230–238.

[46] R.B. Waterhouse, Fretting corrosion, Pergamon press, 1972.

[47] T. Kayaba, A. Iwabuchi, The fretting wear of 0.45% C steel and austenitic stainless steel from 20 to 650 C in air, Wear. 74 (1981) 229–245.

[48] I. Velkavrh, F. Autserer, S. Klien, J. Voyer, A. Ristow, J. Brenner, P. Forêt, A. Diem, The influence of temperature on friction and wear of unlubricated steel/steel contacts in different gaseous atmospheres, Tribol. Int. 98 (2016) 155–171. doi:10.1016/j.triboint.2016.02.022.

[49] X. Liu, Z. Cai, J. He, J. Peng, M. Zhu, Effect of elevated temperature on fretting wear under electric contact, Wear. 376 (2017) 643–655.

[50] R.B. Waterhouse, A. Iwabuchi, High temperature fretting wear of four titanium alloys, Wear. 106 (1985) 303–313.

[51] L. Xin, B.B. Yang, Z.H. Wang, J. Li, Y.H. Lu, T. Shoji, Microstructural evolution of subsurface on Inconel 690TT alloy subjected to fretting wear at elevated temperature, Mater. Des. 104 (2016) 152–161. doi:10.1016/J.MATDES.2016.05.030.

[52] D. Kesavan, V. Done, M.R. Sridhar, R. Billig, D. Nelias, High temperature fretting wear prediction of exhaust valve material, Tribol. Int. 100 (2016) 280–286.

[53] R. Rybiak, S. Fouvry, B. Bonnet, Fretting wear of stainless steels under variable temperature conditions: Introduction of a ‘composite’ wear law, Wear. 268 (2010) 413–423. doi:10.1016/J.WEAR.2009.08.029.

[54] A. Shafiee, M.T. Ahmadian, M. Hoviattalab, Mechanical Characterization of Brain Tissue in Compression, Proc. ASME Des. Eng. Tech. Conf. 3 (2016). doi:10.1115/DETC2016-59019.

[55] A. Shafiee, A. Ahmadian, M. Alidoost, A. Shafiee, A. Ahmadian, M. Alidoost, Investigation of Loss of Consciousness Induced by Gravity Acceleration on the Human Brain, Open Access Libr. J. 8 (2021) 1–24. doi:10.4236/OALIB.1107507.

[56] P.L. Hurricks, The fretting wear of mild steel from 200 to 500 C, Wear. 30 (1974) 189–212.

[57] P.L. Hurricks, The fretting wear of mild steel from room temperature to 200 C, Wear. 19 (1972) 207–229.

[58] Y. Birol, High temperature sliding wear behaviour of Inconel 617 and Stellite 6 alloys, Wear. 269 (2010) 664–671.

[59] A. Shafiee, A. Ahmadian, A. Akbari, A. Shafiee, A. Ahmadian, A. Akbari, A Parametric Study of Mechanical Cross-Coupling in Parallel-Kinematics Piezo-Flexural Nano-Positioning Systems, Open J. Appl. Sci. 11 (2021) 596–613. doi:10.4236/OJAPPS.2021.115043.

[60] A. Niknejad, A. Zareei, Ballistic limit velocity of empty rectangular metal columns under a blunt projectile penetration:, Http://Dx.Doi.Org/10.1177/1548512915590611. 13 (2015) 119–131. doi:10.1177/1548512915590611.

[61] H. Kato, K. Komai, Tribofilm formation and mild wear by tribo-sintering of nanometer-sized oxide particles on rubbing steel surfaces, Wear. 262 (2007) 36–41.

[62] F.H. Stott, G.C. Wood, The influence of oxides on the friction and wear of alloys, Tribol. Int. 11 (1978) 211–218.

[63] A. Zareei, S.M. Nabavi, Calculation of stress intensity factors for circumferential semi-elliptical cracks with high aspect ratio in pipes, Int. J. Press. Vessel. Pip. 146 (2016) 32–38. doi:10.1016/J.IJPVP.2016.05.008.

[64] M. Godet, The third-body approach: a mechanical view of wear, Wear. 100 (1984) 437–452.

[65] A. Zmitrowicz, Wear debris: a review of properties and constitutive models, J. Theor. Appl. Mech. 43 (2005) 3–35.

[66] R.B. Waterhouse, D.E. Taylor, Fretting debris and the delamination theory of wear, Wear. 29 (1974) 337–344. doi:10.1016/0043-1648(74)90019-2.

[67] A. Iwabuchi, The role of oxide particles in the fretting wear of mild steel, Wear. 151 (1991) 301–311. doi:10.1016/0043-1648(91)90257-U.

[68] L. Vincent, Y. Berthier, A. Floquet, M. Godet, Fretting: Load carrying capacity of wear debris, J. Tribol. 106 (1984) 192–200. doi:10.1115/1.3260881.

[69] J.K. Lancaster, GEOMETRICAL EFFECTS ON THE WEAR OF POLYMERS AND CARBONS., in: Am. Soc. Mech. Eng., American Society of Mechanical Engineers Digital Collection, 1974: pp. 187–194. doi:10.1115/1.3452553.

[70] Y. Berthier, L. Vincent, M. Godet, Velocity accommodation in fretting, Wear. 125 (1988) 25–38. doi:10.1016/0043-1648(88)90191-3.

[71] Y. Berthier, Experimental evidence for friction and wear modelling, Wear. 139 (1990) 77–92. doi:10.1016/0043-1648(90)90210-2.

[72] I. Iordanoff, Y. Berthier, S. Descartes, H. Heshmat, A review of recent approaches for modeling solid third bodies, J. Tribol. 124 (2002) 725–735. doi:10.1115/1.1467632.

[73] H. Heshmat, The quasi-hydrodynamic mechanism of powder lubrication—part III: On theory and rheology of triboparticulates, Tribol. Trans. 38 (1995) 269–276. doi:10.1080/10402009508983404.

[74] P.A. Cundall, O.D.L. Strack, A discrete numerical model for granular assemblies, Géotechnique. 29 (1979) 47–65. doi:10.1680/geot.1979.29.1.47.

[75] N. Fillot, I. Iordanoff, Y. Berthier, A granular dynamic model for the degradation of material, J. Tribol. 126 (2004) 606–614. doi:10.1115/1.1705666.

[76] I. Iordanoff, K. Elkholy, M.M. Khonsari, Effect of particle size dispersion on granular lubrication regimes, Proc. Inst. Mech. Eng. Part J J. Eng. Tribol. 222 (2008) 725–739. doi:10.1243/13506501JET414.

[77] V. Linck, L. Baillet, Y. Berthier, Modeling the consequences of local kinematics of the first body on friction and on third body sources in wear, Wear. 255 (2003) 299–308. doi:10.1016/S0043-1648(03)00207-2.

[78] J. Ding, I.R. McColl, S.B. Leen, P.H. Shipway, A finite element based approach to simulating the effects of debris on fretting wear, Wear. 263 (2007) 481–491.

[79] M.A. Kabir, M.R. Lovell, C.F. Higgs, Utilizing the explicit finite element method for studying granular flows, Tribol. Lett. 29 (2008) 85–94. doi:10.1007/s11249-007-9285-y.

[80] H.P. Cao, M. Renouf, F. Dubois, Y. Berthier, Coupling continuous and discontinuous descriptions to model first body deformation in third body flows, J. Tribol. 133 (2011). doi:10.1115/1.4004881.

[81] S. Basseville, E. Héripré, G. Cailletaud, Numerical simulation of the third body in fretting problems, Wear. 270 (2011) 876–887. doi:10.1016/j.wear.2011.02.016.

[82] B.D. Leonard, A. Ghosh, F. Sadeghi, S. Shinde, M. Mittelbach, Third body modeling in fretting using the combined finite-discrete element method, Int. J. Solids Struct. 51 (2014) 1375–1389. doi:10.1016/j.ijsolstr.2013.12.036.

[83] A. Ghosh, W. Wang, F. Sadeghi, An elastic--plastic investigation of third body effects on fretting contact in partial slip, Int. J. Solids Struct. 81 (2016) 95–109.

[84] A. Ahmadi, F. Sadeghi, S. Shaffer, In-Situ Friction and Fretting Wear Measurements of Inconel 617 at Elevated Temperatures, Wear. 410 (2018) 110–118.

[85] B.J. Hamrock, S.R. Schmid, B.O. Jacobson, Fundamentals of fluid film lubrication, CRC press, 2004.

[86] Q. Xue, W. Liu, Z. Zhang, Friction and wear properties of a surface-modified TiO2 nanoparticle as an additive in liquid paraffin, Wear. 213 (1997) 29–32.

[87] H. Kamimura, T. Kubo, I. Minami, S. Mori, Effect and mechanism of additives for ionic liquids as new lubricants, Tribol. Int. 40 (2007) 620–625.

[88] H.D. Huang, J.P. Tu, L.P. Gan, C.Z. Li, An investigation on tribological properties of graphite nanosheets as oil additive, Wear. 261 (2006) 140–144.

[89] M. Kalin, J. Kogovšek, M. Remškar, Mechanisms and improvements in the friction and wear behavior using MoS2 nanotubes as potential oil additives, Wear. 280 (2012) 36–45.

[90] A.A. Alazemi, A.D. Dysart, X.L. Phuah, V.G. Pol, F. Sadeghi, MoS2 nanolayer coated carbon spheres as an oil additive for enhanced tribological performance, Carbon N. Y. 110 (2016) 367–377.

[91] A.A. Alazemi, V. Etacheri, A.D. Dysart, L.-E. Stacke, V.G. Pol, F. Sadeghi, Ultrasmooth submicrometer carbon spheres as lubricant additives for friction and wear reduction, ACS Appl. Mater. Interfaces. 7 (2015) 5514–5521.

[92] S.S. Kandanur, M.A. Rafiee, F. Yavari, M. Schrameyer, Z.-Z. Yu, T.A. Blanchet, N. Koratkar, Suppression of wear in graphene polymer composites, Carbon N. Y. 50 (2012) 3178–3183.

[93] N. Nemati, M. Emamy, S. Yau, J.-K. Kim, D.-E. Kim, High temperature friction and wear properties of graphene oxide/polytetrafluoroethylene composite coatings deposited on stainless steel, RSC Adv. 6 (2016) 5977–5987.

[94] J. Xu, M.H. Zhu, Z.R. Zhou, P. Kapsa, L. Vincent, An investigation on fretting wear life of bonded MoS2 solid lubricant coatings in complex conditions, Wear. 255 (2003) 253–258.

[95] Y. Kimura, T. Wakabayashi, K. Okada, T. Wada, H. Nishikawa, Boron nitride as a lubricant additive, Wear. 232 (1999) 199–206.

[96] N.L. McCook, D.L. Burris, P.L. Dickrell, W.G. Sawyer, Cryogenic friction behavior of PTFE based solid lubricant composites, Tribol. Lett. 20 (2005) 109–113.

[97] D. Berman, A. Erdemir, A. V Sumant, Graphene: a new emerging lubricant, Mater. Today. 17 (2014) 31–42.

[98] A.A. Balandin, S. Ghosh, W. Bao, I. Calizo, D. Teweldebrhan, F. Miao, C.N. Lau, Superior thermal conductivity of single-layer graphene, Nano Lett. 8 (2008) 902–907.

[99] I.N. Kholmanov, C.W. Magnuson, A.E. Aliev, H. Li, B. Zhang, J.W. Suk, L.L. Zhang, E. Peng, S.H. Mousavi, A.B. Khanikaev, others, Improved electrical conductivity of graphene films integrated with metal nanowires, Nano Lett. 12 (2012) 5679–5683.

[100] C. Lee, X. Wei, J.W. Kysar, J. Hone, Measurement of the elastic properties and intrinsic strength of monolayer graphene, Science (80-.). 321 (2008) 385–388.

[101] A. Klemenz, L. Pastewka, S.G. Balakrishna, A. Caron, R. Bennewitz, M. Moseler, Atomic scale mechanisms of friction reduction and wear protection by graphene, Nano Lett. 14 (2014) 7145–7152.

[102] D. Marchetto, C. Held, F. Hausen, F. Wählisch, M. Dienwiebel, R. Bennewitz, Friction and wear on single-layer epitaxial graphene in multi-asperity contacts, Tribol. Lett. 48 (2012) 77–82.

[103] L.-Y. Lin, D.-E. Kim, W.-K. Kim, S.-C. Jun, Friction and wear characteristics of multi-layer graphene films investigated by atomic force microscopy, Surf. Coatings Technol. 205 (2011) 4864–4869.

[104] F. Wählisch, J. Hoth, C. Held, T. Seyller, R. Bennewitz, Friction and atomic-layer-scale wear of graphitic lubricants on SiC (0001) in dry sliding, Wear. 300 (2013) 78–81.

[105] M.-S. Won, O. V Penkov, D.-E. Kim, Durability and degradation mechanism of graphene coatings deposited on Cu substrates under dry contact sliding, Carbon N. Y. 54 (2013) 472–481.

[106] D. Berman, A. Erdemir, A. V Sumant, Reduced wear and friction enabled by graphene layers on sliding steel surfaces in dry nitrogen, Carbon N. Y. 59 (2013) 167–175.

[107] A. Moezzi, A.M. McDonagh, M.B. Cortie, Zinc oxide particles: Synthesis, properties and applications, Chem. Eng. J. 185 (2012) 1–22.

[108] C. Wu, F. Li, Y. Zhang, L. Wang, T. Guo, Formation and field emission of patterned zinc oxide-adhering graphene cathodes, Vacuum. 89 (2013) 57–61.

[109] H.-J. Song, Z.-Z. Zhang, X.-H. Men, Z.-Z. Luo, A study of the tribological behavior of nano-ZnO-filled polyurethane composite coatings, Wear. 269 (2010) 79–85.

[110] B. Selvam, P. Marimuthu, R. Narayanasamy, V. Anandakrishnan, K.S. Tun, M. Gupta, M. Kamaraj, Dry sliding wear behaviour of zinc oxide reinforced magnesium matrix nano-composites, Mater. Des. 58 (2014) 475–481.

[111] A.A. Alazemi, A.D. Dysart, S.J. Shaffer, V.G. Pol, L.-E. Stacke, F. Sadeghi, Novel tertiary dry solid lubricant on steel surfaces reduces significant friction and wear under high load conditions, Carbon N. Y. 123 (2017) 7–17.

[112] Y. Akiniwa, S. Stanzl-Tschegg, H. Mayer, M. Wakita, K. Tanaka, Fatigue strength of spring steel under axial and torsional loading in the very high cycle regime, Int. J. Fatigue. 30 (2008) 2057–2063.

[113] H. Matsunaga, N. Shomura, S. Muramoto, M. Endo, Shear mode threshold for a small fatigue crack in a bearing steel, Fatigue Fract. Eng. Mater. Struct. 34 (2011) 72–82.

[114] S.M. Moghaddam, J.A.R. Bomidi, F. Sadeghi, N. Weinzapfel, A. Liebel, Effects of compressive stresses on torsional fatigue, Tribol. Int. 77 (2014) 196–210.

[115] J.A.R. Bomidi, N. Weinzapfel, T. Slack, S.M. Moghaddam, F. Sadeghi, A. Liebel, J. Weber, T. Kreis, Experimental and numerical investigation of torsion fatigue of bearing steel, J. Tribol. 135 (2013) 31103.

[116] B. Jalalahmadi, F. Sadeghi, V. Bakolas, Material inclusion factors for Lundberg-Palmgren--based RCF life equations, Tribol. Trans. 54 (2011) 457–469.

[117] V. V Bolotin, I.L. Belousov, Early fatigue crack growth as the damage accumulation process, Probabilistic Eng. Mech. 16 (2001) 279–287.

[118] N. Shamsaei, A. Fatemi, Deformation and fatigue behaviors of case-hardened steels in torsion: Experiments and predictions, Int. J. Fatigue. 31 (2009) 1386–1396.

[119] J. Aktaa, R. Schmitt, High temperature deformation and damage behavior of RAFM steels under low cycle fatigue loading: Experiments and modeling, Fusion Eng. Des. 81 (2006) 2221–2231.

[120] A. Rinaldi, P. Peralta, D. Krajcinovic, Y.-C. Lai, Prediction of scatter in fatigue properties using discrete damage mechanics, Int. J. Fatigue. 28 (2006) 1069–1080.

[121] T. Slack, F. Sadeghi, Cohesive zone modeling of intergranular fatigue damage in rolling contacts, Tribol. Int. 44 (2011) 797–804.

[122] I. V Papadopoulos, A new criterion of fatigue strength for out-of-phase bending and torsion of hard metals, Int. J. Fatigue. 16 (1994) 377–384.

[123] S. Fouvry, P. Duo, P. Perruchaut, A quantitative approach of Ti--6Al--4V fretting damage: friction, wear and crack nucleation, Wear. 257 (2004) 916–929.

[124] T. Dick, C. Paulin, G. Cailletaud, S. Fouvry, Experimental and numerical analysis of local and global plastic behaviour in fretting wear, Tribol. Int. 39 (2006) 1036–1044.

[125] F.H. Stott, High-temperature sliding wear of metals, Tribol. Int. 35 (2002) 489–495.

[126] A. Cruzado, M. Hartelt, R. Wäsche, M.A. Urchegui, X. Gómez, Fretting wear of thin steel wires. Part 2: Influence of crossing angle, Wear. 273 (2011) 60–69.

[127] N.A. Henein, Z. Ma, S. Huang, W. Bryzik, J. Glidewell, In Situ Wear Measuring Technique in Engine Cylinders{\copyright}, Tribol. Lubr. Technol. 71 (2015) 46.

[128] A. Ghosh, F. Sadeghi, A novel approach to model effects of surface roughness parameters on wear, Wear. 338 (2015) 73–94.

[129] M.S. Rahman, G. Priyadarshan, K.S. Raja, C. Nesbitt, M. Misra, Characterization of high temperature deformation behavior of INCONEL 617, Mech. Mater. 41 (2009) 261–270.

[130] D. Kaoumi, K. Hrutkay, Tensile deformation behavior and microstructure evolution of Ni-based superalloy 617, J. Nucl. Mater. 454 (2014) 265–273.

[131] H.-P. Meurer, G.K.H. Gnirss, W. Mergler, G. Raule, H. Schuster, G. Ullrich, Investigations on the fatigue behavior of high-temperature alloys for high-temperature gas-cooled reactor components, Nucl. Technol. 66 (1984) 315–323.

[132] K.B.S. Rao, H. Schiffers, H. Schuster, H. Nickel, Influence of time and temperature dependent processes on strain controlled low cycle fatigue behavior of alloy 617, Metall. Trans. A. 19 (1988) 359–371.

[133] T.C. Totemeier, H. Tian, Creep-fatigue--environment interactions in INCONEL 617, Mater. Sci. Eng. A. 468 (2007) 81–87.

[134] M.A. Burke, C.G. Beck, The high temperature low cycle fatigue behavior of the nickel base alloy IN-617, Metall. Trans. A. 15 (1984) 661–670.

[135] A. E407-07, Standard practice for microetching metals and alloys, (2015).

[136] A.S. for Testing, P.. Materials (Filadelfia, ASTM E112-96 (2004) e2: Standard Test Methods for Determining Average Grain Size, in: 2004.

[137] Z. Golmohammadi, A. Walvekar, F. Sadeghi, A 3D efficient finite element model to simulate rolling contact fatigue under high loading conditions, Tribol. Int. 126 (2018) 258–269.

[138] Z. Golmohammadi, F. Sadeghi, A. Walvekar, M. Saei, K.K. Mistry, Y.S. Kang, Experimental and analytical investigation of effects of refurbishing on rolling contact fatigue, Wear. 392 (2017) 190–201.

[139] A. Ahmadi, R. Mirzaeifar, N.S. Moghaddam, A.S. Turabi, H.E. Karaca, M. Elahinia, Effect of manufacturing parameters on mechanical properties of 316L stainless steel parts fabricated by selective laser melting: A computational framework, Mater. Des. 112 (2016) 328–338.

[140] A. Vijay, N. Paulson, F. Sadeghi, A 3D finite element modelling of crystalline anisotropy in rolling contact fatigue, Int. J. Fatigue. 106 (2018) 92–102.

[141] A. Vijay, F. Sadeghi, An anisotropic damage model for tensile fatigue, Fatigue Fract. Eng. Mater. Struct. 42 (2019) 129–142.

[142] J.A.R. Bomidi, F. Sadeghi, Three-dimensional finite element elastic--plastic model for subsurface initiated spalling in rolling contacts, J. Tribol. 136 (2014) 11402.

[143] J. Lemaitre, A course on damage mechanics, Springer Science & Business Media, 2012.

[144] N. Weinzapfel, F. Sadeghi, Numerical modeling of sub-surface initiated spalling in rolling contacts, Tribol. Int. 59 (2013) 210–221.

[145] Y.-C. Xiao, S. Li, Z. Gao, A continuum damage mechanics model for high cycle fatigue, Int. J. Fatigue. 20 (1998) 503–508.

[146] A.A. Walvekar, F. Sadeghi, Rolling contact fatigue of case carburized steels, Int. J. Fatigue. 95 (2017) 264–281.

[147] J. Lubliner, Plasticity theory, Courier Corporation, 2008.

[148] N.R. Paulson, Z. Golmohammadi, A.A. Walvekar, F. Sadeghi, K. Mistry, Rolling contact fatigue in refurbished case carburized bearings, Tribol. Int. 115 (2017) 348–364.

[149] K.B.S. Rao, H.-P. Meurer, H. Schuster, Creep-fatigue interaction of inconel 617 at 950 C in simulated nuclear reactor helium, Mater. Sci. Eng. A. 104 (1988) 37–51.

[150] S. Mall, J.M. Engesser, Effects of frequency on fatigue behavior of CVI C/SiC at elevated temperature, Compos. Sci. Technol. 66 (2006) 863–874.

[151] K. Slámečka, P. Pon\'\ižil, J. Pokluda, Quantitative fractography in bending-torsion fatigue, Mater. Sci. Eng. A. 462 (2007) 359–362.

[152] K. Slámečka, J. Pokluda, P. Pon\'\ižil, Š. Major, P. Šandera, On the topography of fracture surfaces in bending--torsion fatigue, Eng. Fract. Mech. 75 (2008) 760–767.

[153] E.S. Zanoria, S. Danyluk, M.J. McNallan, Formation of cylindrical sliding-wear debris on silicon in humid conditions and elevated temperatures, Tribol. Trans. 38 (1995) 721–727. doi:10.1080/10402009508983464.

[154] A. Warhadpande, F. Sadeghi, M.N. Kotzalas, G. Doll, Effects of plasticity on subsurface initiated spalling in rolling contact fatigue, Int. J. Fatigue. 36 (2012) 80–95. doi:10.1016/j.ijfatigue.2011.08.012.

[155] A.A. Reda, R. Bowen, V.C. Westcott, Characteristics of particles generated at the interface between sliding steel surfaces, Wear. 34 (1975) 261–273. doi:10.1016/0043-1648(75)90095-2.

[156] H.R. Shetty, T.H. Kosel, N.F. Fiore, A study of abrasive wear mechanisms using diamond and alumina scratch tests, Wear. 80 (1982) 347–376. doi:10.1016/0043-1648(82)90262-9.

[157] S. Söderberg, U. Bryggman, T. McCullough, Frequency effects in fretting wear, Wear. 110 (1986) 19–34. doi:10.1016/0043-1648(86)90149-3.

[158] A. Kapoor, K.L. Johnson, Plastic ratchetting as a mechanism of metallic wear, Proc. R. Soc. A Math. Phys. Eng. Sci. 445 (1994) 367–381. doi:10.1098/rspa.1994.0066.

[159] S. Fouvry, K. Elleuch, G. Simeon, Prediction of crack nucleation under partial slip fretting conditions, J. Strain Anal. Eng. Des. 37 (2002) 549–564. doi:10.1243/030932402320950152.

[160] J. Jiang, F.H. Stott, M.M. Stack, The role of triboparticulates in dry sliding wear, Tribol. Int. 31 (1998) 245–256. doi:10.1016/S0301-679X(98)00027-9.

[161] N.M. Everitt, J. Ding, G. Bandak, P.H. Shipway, S.B. Leen, E.J. Williams, Characterisation of fretting-induced wear debris for Ti-6Al-4 V, Wear. 267 (2009) 283–291. doi:10.1016/j.wear.2008.12.032.

[162] R.M. Matveevsky, The critical temperature of oil with point and line contact machines, J. Fluids Eng. Trans. ASME. 87 (1965) 754–759. doi:10.1115/1.3650672.

[163] A. Ahmadi, N.S. Moghaddam, M. Elahinia, H.E. Karaca, R. Mirzaeifar, Finite element modeling of selective laser melting 316l stainless steel parts for evaluating the mechanical properties, in: ASME 2016 11th Int. Manuf. Sci. Eng. Conf., 2016: p. V002T01A003--V002T01A003.

[164] Z. Golmohammadi, F. Sadeghi, A Coupled Multibody Finite Element Model for Investigating Effects of Surface Defects on Rolling Contact Fatigue, J. Tribol. 141 (2019) 41402.

[165] A.A. Walvekar, D. Morris, Z. Golmohammadi, F. Sadeghi, M. Correns, A novel modeling approach to simulate rolling contact fatigue and three-dimensional spalls, J. Tribol. 140 (2018) 31101.

[166] K. Singh, F. Sadeghi, M. Correns, T. Blass, A microstructure based approach to model effects of surface roughness on tensile fatigue, Int. J. Fatigue. 129 (2019). doi:10.1016/j.ijfatigue.2019.105229.

[167] D.A. Hills, D. Nowell, Mechanics of fretting fatigue. Solid mechanics and its applications vol. 30, (1994).

[168] D.A. Hills, D. Nowell, J.J. O'Connor, On the mechanics of fretting fatigue, Wear. 125 (1988) 129–146.

[169] A. Ahmadi, F. Sadeghi, Experimental and Numerical Investigation of Torsion Fatigue of a Nickel-Based Alloy at Elevated Temperature, Mater. Sci. Eng. A. 751 (2019) 263–270.

[170] I.V. Kragelsky, M.N. Dobychin, V.S. Kombalov, Friction and wear: calculation methods, Elsevier, 2013.

[171] A. Sharma, A. Vijay, F. Sadeghi, Finite element modeling of fretting wear in anisotropic composite coatings: Application to HVOF Cr3C2–NiCr coating, Tribol. Int. 155 (2021) 106765. doi:10.1016/j.triboint.2020.106765.

[172] J.F. Archard, Wear theory and mechanisms, Wear Control Handb. 58 (1980).

[173] J.F. Archard, W. Hirst, The wear of metals under unlubricated conditions, Proc. R. Soc. London. Ser. A. Math. Phys. Sci. 236 (1956) 397–410.

[174] G.K. Nikas, R.S. Sayles, Surface coatings and finite-element analysis of layered fretting contacts, Proc. Inst. Mech. Eng. Part J J. Eng. Tribol. 223 (2009) 159–181. doi:10.1243/13506501JET441.

[175] B.D. Leonard, F. Sadeghi, S. Shinde, M. Mittelbach, A novel modular fretting wear test rig, Wear. 274 (2012) 313–325.

[176] I. Childres, L.A. Jauregui, W. Park, H. Cao, Y.P. Chen, Raman spectroscopy of graphene and related materials, New Dev. Phot. Mater. Res. 1 (2013).

[177] W. Gao, Graphite oxide: Structure, reduction and applications, Rice University, 2012.

[178] V. \cTucureanu, A. Matei, A.M. Avram, FTIR spectroscopy for carbon family study, Crit. Rev. Anal. Chem. 46 (2016) 502–520.

[179] Y. Dou, L.U.O. Min, S. Liang, X. Zhang, X. Ding, B. Liang, Flexible free-standing graphene-like film electrode for supercapacitors by electrophoretic deposition and electrochemical reduction, Trans. Nonferrous Met. Soc. China. 24 (2014) 1425–1433.

[180] D.W. Lee, L. De Los Santos V, J.W. Seo, L.L. Felix, A. Bustamante D, J.M. Cole, C.H.W. Barnes, The structure of graphite oxide: investigation of its surface chemical groups, J. Phys. Chem. B. 114 (2010) 5723–5728.

[181] L. Shahriary, A.A. Athawale, Graphene oxide synthesized by using modified hummers approach, Int J Renew Energy Env. Eng. 2 (2014) 58–63.

[182] F.Y. Ban, S.R. Majid, N.M. Huang, H.N. Lim, Graphene oxide and its electrochemical performance, Int. J. Electrochem. Sci. 7 (2012) 4345–4351.

[183] K.T. Dissanayake, W.R. De Silva, A. Kumarasinghe, K.M.N. De Silva, Synthesis of Graphene and Graphene Oxide Based Nanocomposites and Their Characterization, in: SAITM Res. Symp. Eng. Adv., 2014: pp. 75–78.

[184] S. Nagarajan, K.A. Kuppusamy, Extracellular synthesis of zinc oxide nanoparticle using seaweeds of gulf of Mannar, India, J. Nanobiotechnology. 11 (2013) 39.

[185] R. Wahab, S.G. Ansari, Y.S. Kim, M.A. Dar, H.-S. Shin, Synthesis and characterization of hydrozincite and its conversion into zinc oxide nanoparticles, J. Alloys Compd. 461 (2008) 66–71.

[186] M. Mohanty, R.W. Smith, M. De Bonte, J.-P. Celis, E. Lugscheider, Sliding wear behavior of thermally sprayed 75/25 Cr3C2/NiCr wear resistant coatings, Wear. 198 (1996) 251–266.

[187] O. Penkov, H.-J. Kim, H.-J. Kim, D.-E. Kim, Tribology of graphene: a review, Int. J. Precis. Eng. Manuf. 15 (2014) 577–585.

[188] D. Berman, A. Erdemir, A. V Sumant, Few layer graphene to reduce wear and friction on sliding steel surfaces, Carbon N. Y. 54 (2013) 454–459.

[189] D. Berman, S.A. Deshmukh, S.K.R.S. Sankaranarayanan, A. Erdemir, A. V Sumant, Extraordinary macroscale wear resistance of one atom thick graphene layer, Adv. Funct. Mater. 24 (2014) 6640–6646.

[190] F. Li, K. Hu, J. Li, B. Zhao, The friction and wear characteristics of nanometer ZnO filled polytetrafluoroethylene, Wear. 249 (2001) 877–882.

[191] S. V Prasad, N.T. McDevitt, J.S. Zabinski, Tribology of tungsten disulfide--nanocrystalline zinc oxide adaptive lubricant films from ambient to 500 C, Wear. 237 (2000) 186–196.

[192] F.J. Carrion, J. Sanes, M.-D. Bermúdez, Influence of ZnO nanoparticle filler on the properties and wear resistance of polycarbonate, Wear. 262 (2007) 1504–1510.

[193] L.-Q. Wang, X.-M. Jia, L. Cui, G.-C. Chen, Effect of aramid fiber and ZnO nanoparticles on friction and wear of PTFE composites in dry and LN2 conditions, Tribol. Trans. 52 (2008) 59–65.